COMBUSTION AND FLOW CHARACTERISTICS OF STAGED COMBUSTORS INVOLVING CONFINED JETS IN CROSSFLOW

A Dissertation
Presented to
The Academic Faculty

by

Nishant Jain

In Partial Fulfillment
of the Requirements for the Degree
Doctor of Philosophy in the
School of Aerospace Engineering

Georgia Institute of Technology
May 2019

COMBUSTION AND FLOW CHARACTERISTICS OF STAGED COMBUSTORS INVOLVING CONFINED JETS IN CROSSFLOW

Approved by:

Dr. Jerry M. Seitzman, Professor, Advisor
School of Aerospace Engineering
Georgia Institute of Technology

Dr. Oleksandr Bibik, Research Scientist
School of Aerospace Engineering
Georgia Institute of Technology

Dr. Timothy C. Lieuwen, Professor
School of Aerospace Engineering
Georgia Institute of Technology

Dr. Randolph J. Smith, Sr. Aerothermal
Engineer
Combustor Aerodynamics
Pratt & Whitney

Dr. Jachiel Jagoda, Professor
School of Aerospace Engineering
Georgia Institute of Technology

Date Approved: January 11, 2019

To my parents, my wife and our son,

Vayu

ACKNOWLEDGEMENTS

TABLE OF CONTENTS

LIST OF TABLES

LIST OF FIGURES

NOMENCLATURE

JICF	Jet(s) in crossflow
CJICF	Confined Jets in crossflow
RQL	Rich burn-Quick quench-Lean burn
LQL	Lean burn-Quick mix-Lean burn
NO_x	Oxides of Nitrogen
CO	Carbon Monoxide
UHC	Unburnt Hydrocarbons
PW	Pratt & Whitney
RR	Rolls Royce
GE	General Electric
TRL	Technologies Readiness Level
SAC	Single Annular Combustor
DAC	Dual Annular Combustor
TAPS	Twin Annular Premixing Swirler
LDI	Lean Direct Injection
LPP	Lean Premixed Prevaporized
ASC	Axially Staged Combustor
VGC	Variable Geometry Combustor
PIV	Particle Image Velocimetry
SPIV	Stereo Particle Image Velocimetry
ϕ	Equivalence ratio
J	Momentum flux ratio

Split	Air split ratio
d_j	Jet diameter
s	Hole spacing
H	Test section height
T	Temperature
U, V	Velocity
ρ	Density
τ_{auto}	Autoignition time
Re	Reynold's number
Da	Damköhler number
$(\ )_\infty$	Crossflow quantity
$(\ )_j$	Jet quantity
$(\ )_p$	Pilot quantity
$(\ )_b$	Bottom jet quantity
$(\ )_t$	Top jet quantity

SUMMARY

Staged combustion offers many advantages in high performance aero-propulsion and power generation applications of gas turbine engines. For example, staged combustors can operate at low overall equivalence-ratio and temperature, thereby, pollutant emissions, while maintaining robustness, e.g., ignitability and flame stability over a greater operational range. To be effective, axial staging approaches require rapid mixing and burning of the staged reactants with the vitiated products from the pilot zone. In practice, this is achieved by utilizing a multiple jets-in-cross-flow (JICF) configuration in a highly reactive and confined combustor environment. While most previous work has focused on studying the properties of single, unconfined JICF, there is a paucity of work employing detailed diagnostics to study multiple and confined JICF (CJICF).

This thesis examines the mixing, velocity and combustion characteristics of CJICF in air-staged (Rich-Quench-Lean, RQL), and fuel-air-staged (Lean-Quench-Lean, LQL) configurations using natural gas and air at atmospheric pressure and high temperature conditions. The well-characterized facility developed for this study allows for injection from five round jets, each produced by sudden contraction; two jets from the top wall and three interlaced jets from the bottom wall, with independent control of each set. Results are presented for parallel (one-sided injection), and staggered-opposed (two-sided injection) jets in a vitiated crossflow. High speed (10 kHz) stereo particle image velocimetry results are used to elucidate the mixing and flow characteristics, while OH* chemiluminescence imaging is used to study the combustion zone. Chemical reactor modeling is also used to help interpret the combustion results.

For multiple confined, high momentum jets, the jet-wall and, to a lesser extent, the jet-jet interactions are found to have a major influence on the flowfield and the mixing characteristics of the jets with the crossflow. For example, the stagnation region where a jet interact with the opposite wall creates an upstream recirculation zone that redirects the crossflow away from the wall. Downstream of the jets, the crossflow can rapidly mix with jet fluid, which is even more noticeable in the regions between the jets due to lateral movement of jet fluid as it is redirected near the wall stagnation zone. The jet-wall impact appears to be more influenced by the total mass injection (or air split ratio in this study) rather than the momentum flux ratio, which is the parameter considered most influential for single, unconfined JICF configurations.

In RQL conditions, with the high temperature crossflow containing H_2 and CO, chemical times (autoignition delays) are sufficiently fast ($\sim$1-100μs), such that flames are stabilized near the jet exits and combustion is found to be mixing limited rather than chemistry limited. For LQL conditions, most of the burning likely occurs due to flame propagation, though a sufficiently high temperature crossflow can lead to enhanced flame stabilization, and burning of the premixed jets before significant mixing with the crossflow. Thus when stabilized in a high temperature crossflow, the LQL jets can burn in the opposed wall stagnation region, while the RQL burning is delayed until mixing with the crossflow occurs.

CHAPTER 1. INTRODUCTION

Investigation of flame and flowfield characteristics of staged combustors for gas turbine applications in aviation industry is presented in this thesis. The experimental and analytical approaches employed to perform these investigations along with the results are explained in the following chapters. In this chapter, the motivation and background for the development of staged combustor technologies are presented along with previous research and literature review that examined jets in crossflow architectures pertaining to their use in staged combustion systems for aero-propulsion applications.

1.1 Motivation

The aviation and power generation industries rely heavily on the development of combustor technologies used in gas turbine engine applications to meet the globally increasing demand for clean energy and high performance propulsion systems. To understand the global impact of combustor technologies and the motivation behind the research and development of gas turbine combustors, it is important to understand their magnitude or scale of operation. In power generation sector about 24% of world's electricity is currently produced using natural gas plants that rely on land based gas turbine engines [1].The aviation industry almost entirely depends on gas turbine engines for propulsion requirements. The number of flights operated every year is astoundingly large, increasing from 32.8 million in 2014 to 39 million in 2018 [2].

With millions of flights in operation to satisfy the emerging need and affordability for air transportation; with increasing demand for electricity as world's population

continues to rise, the risk of adverse environmental effects due to pollutants such as oxides of nitrogen (NO_x, NO, NO_2), carbon monoxide (CO) and unburned hydrocarbons (UHCs) is of grave concern [3-5]. Hence, increasingly stringent regulations concerning emission levels have been established, especially in the aviation sector [6, 7]. Besides meeting the requirements for low emission levels from combusting hydrocarbon fuels, the aircraft engines are also required to be increasingly robust, powerful, efficient and reliable [8-12]. Combustor design plays a vital role in achieving these goals, and the staged combustion technology has been one approach successfully employed to date.
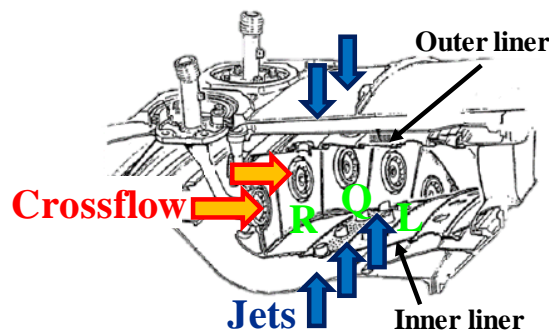
Figure 1.1: An example of staged combustor employing JICF configuration (Rolls Royce Phase 5 combustor) [13].

In a simplified manner, as illustrated in Figure 1.1, the flowfield in staged combustors can be represented as conditions involving multiple transverse jets carrying significant amount of mass and momentum flux into a highly reactive crossflow of hot vitiated products from a pilot burner. This jets in crossflow (JICF) configuration is considered remarkably effective for staging and rapid mixing of the fluid from jets and the vitiated products from pilot burner in the quench zones and for rapid re-ignition and flame stabilization in the secondary combustion zone [9, 11, 14-16]. With increased mass flow,

the jets have very high velocity in their potential core and can be highly *confined* between the combustor liner walls [17]. Although, single unconfined JICF configuration have been studied to a great extent by previous researchers, multiple confined jets in crossflow (CJICF) scenario has not been studied extensively. Thus, examining CJICF configuration to investigate the interplay of mixing, flow field and combustion processes involved under confined engine conditions using advanced optical diagnostics techniques in an experimental laboratory setup is instrumental to understanding and extending the limits of low emission staged combustion architectures.

1.2   Staged Combustion

Staged combustion offers several advantages in high performance aero-propulsion and power generation applications which require robust gas turbine engines producing low emissions. Contrary to using a single combustion zone supplied with fuel and air from one injection location, multiple combustion zones in a staged combustor obtained by distributing or "staging" air, fuel and premixed fuel-air supplies provide extra means to control the overall combustor performance. As identified in Figure 1.2, the initial zone (1) involves fuel-rich combustion, which is easy to ignite and promotes flame holding. The secondary and tertiary dilution air initially bypassed around the combustor dome is gradually injected in zones 2 and 3 through the holes in the liner walls ensuring stable and complete combustion and control over the exit temperature profile [18]. Multiple stages can help optimize the combustor to produce low emissions while maintaining ignition reliability, flame stability, good turn-down ratio, desired pattern factor, fuel flexibility and reduced thermo-acoustic oscillations – all while operating at low overall equivalence ratios [19].
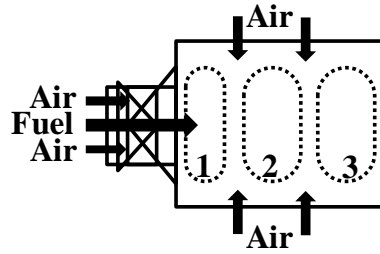
Figure 1.2: Schematic of a staged combustor with primary rich combustion (zone 1), secondary lean combustion (zone 2), tertiary lean combustion (zone 3).
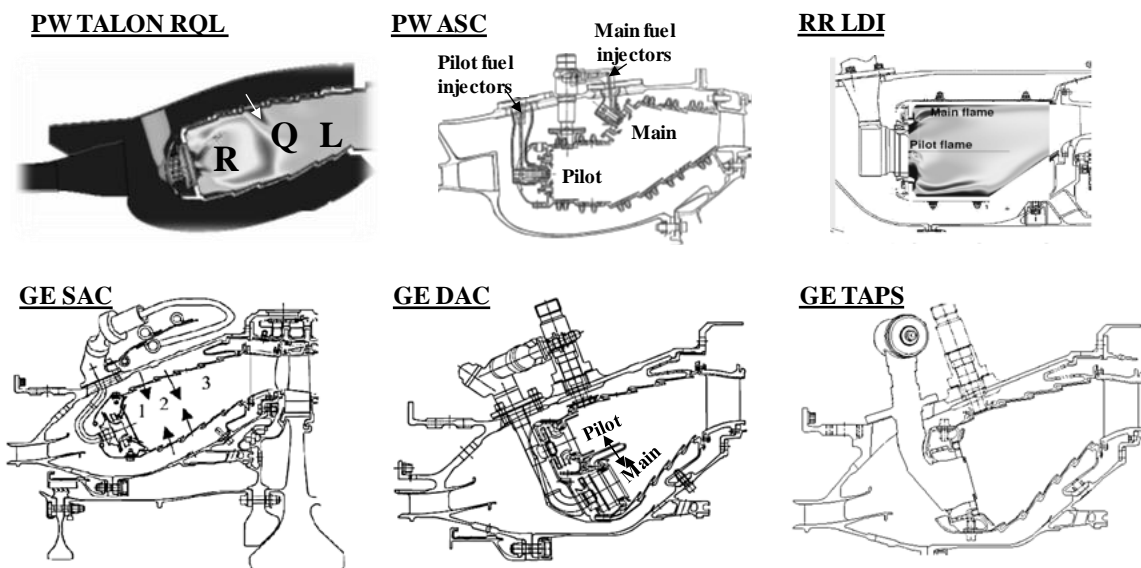
Figure 1.3: Existing low emission technologies and staged combustors from leading manufacturers Pratt & Whitney (PW), Rolls Royce (RR) and General Electric (GE) [14, 18-22].

The staging techniques can be categorized based on the types of injected fluid as air, fuel and premixed fuel/air staging. Based on the geometry, the combustors are categorized as radial (annular) or axial staged combustors. There are several high Technologies Readiness Level (TRL) low emissions staged combustors illustrated in Figure 1.3 such as, Rich-Burn, Quick-Quench, Lean-Burn (RQL), Single Annular Combustor (SAC), Dual Annular Combustor (DAC), Twin Annular Premixing Swirler

(TAPS), Lean Direct Injection (LDI) combustors. Some of the lower TRL devices include NASA multipoint LDI (MLDI), Lean Premixed Prevaporized (LPP), Axially Staged Combustors (ASC) and Variable Geometry Combustors (VGC). RQL combustors are primarily of the SAC type that involve air staging where bypassed dilution air jets enter the combustor through holes in the liners downstream of the pilot combustor. Fuel or fuel-air staging can be used in both SAC and DAC configurations as shown in Figure 1.3 for PW and GE combustors. One way to look at SAC and DAC is that the combustion occurs in "series" and in "parallel" respectively.

The performance of these combustors are reviewed in detail by Liu et. al. [18] while addressing issues such as combustion efficiency, combustion instability, altitude relight capability, pressure loss, autoignition/flashback risk, size/weight, liner durability and most importantly, low emissions capabilities. A qualitative assessment summary of combustion performance of these combustors is tabulated in Table 1.1.

The combustion efficiency of turbine engine combustors has improved significantly over the decades; at present, greater than 99.5% combustion efficiency is achieved at take-off conditions and between 98%-99.5% combustion efficiency can be seen at low power conditions. At high power conditions, RQL combustors demonstrate an efficiency of 99.9%. High idle efficiency (at low power) is achieved in lean-burn combustors through local rich burn due to fuel staging.

Table 1.1: Qualitative comparison of low emissions combustors performance [18].

	RQL	DAC	ASC	TAPS	LDI	MLDI	LPP	VGC
TRL	9	9	≤ 5	9	≤ 7	≤ 5	≤ 5	< 5 (for aeros)
Altitude relight capability	High	Moderate	Moderate	Moderate	Moderate	Low	Moderate	Higher
Autoignition/flashback risk	Low	Low	Low	Moderate	Low	Low	High	Low
Combustion stability	High	Moderate	Moderate	Moderate	Moderate	Moderate	Low	Moderate
Combustion efficiency (high power)	High	High	High	High	High	High	High	High
Combustion (low power)	High	High	Higher	High	High	High	High	Higher
Pressure loss	Moderate	Moderate	Moderate	Moderate	Moderate	High	Moderate	High
LTO Nox	Low	Lower	Lower	Even Lower	Even Lower	Evern Lower	Lowest	Lower
LTO CO (low power)	Moderate	Higher	Moderate	High	High	High	High	Low
LTO UHC (low power)	Moderate	High	Low	Low	Low	Low	Low	Low
Smoke number	High	Moderate	Low	Low	Low	Low	Low	Low
Weight	Moderate	Heavy	Heavy	Moderate	Moderate	Moderate	Moderate	Heavy
Fuel coking	Moderate	Moderate	Higher	Moderate	High	High	Moderate	Moderate
Liner life	Moderate	Moderate	Moderate	Long	Long	Long	Long	Moderate
OTDF/RTDF quality	High	Moderate	High	Higher	Higher	Higher	Higher	Moderate

Rich-burn combustors such as the PW RQL shown in Figure 1.3 also have improved altitude relight performance compared to lean-burn combustors due to the stability of richer fuel-air stoichiometry and less susceptibility to local quenching from staging. However with continued improvements, some of the lean burn combustors such as the Rolls Royce LDI has achieved relight capability of 9143 m (30,000 feet) in E3E engine testing [21]. Autoignition and flashback risks are theoretically highest in LPP premixed staged systems in comparison to the diffusion or non-premixed systems such as RQL, DAC, ASC, LDI, MLDI and VGC. Lean premixed combustion systems are also more prone to combustion instabilities that arise due to coupling of unstable combustion processes from fluctuation in fuel-air mixture composition and the combustor duct acoustics.

Axial staging has certain advantages over the radial staging as the local quenching can be minimized due to axial staging when compared to internally staged RR LDI and GE TAPS. The axially staged, PW V2500 combustor has an inward located pilot stage and outward located main stage as shown in Figure 1.3; this eliminates combustor susceptibility

to blow out in heavy rain since the compressor centrifuges the water to the outer flow path [20]. Both ASC and DAC face weight penalty due to complex fuel feed systems. In ASC, the increase in axial length and the introduction of separate fuel feed system introduces a weight penalty. In DAC, the high surface to volume ratio presents cooling challenges which in turn imposes a weight penalty.

Many of these staging approaches involve application of JICF, for example with dilution air jets issuing into the vitiated crossflow of combustion products from the primary zone. These applications are described below with an emphasis laid on air and premixed fuel-air staging techniques that involve CJICF which is in line with the work presented in this thesis.

1.2.1   *Air Staged Rich-Burn, Quick-Quench, Lean-Burn (RQL) Combustion*

Rich-Burn, Quick-Quench, Lean-Burn (RQL), also known as Rich-Quench-Lean combustors that use air-staging have been under development for several decades (since 1970s) proving effective in reducing NO_x emissions while meeting overall requirements, especially in aero-propulsion applications [8, 17, 23-26]. RQL type non-premixed air-staging is used in various combustors in the aviation industry, such as the PW RQL type TALON (Technology for Advanced Low NO_x) shown in Figure 1.3, the RR Phase 5 shown in Figure 1.1 and the GE LEC (Lean Emissions Combustor) [14, 21, 22, 27, 28].

As shown in Figure 1.4, the range of temperatures favorable to minimizing the competing CO and NO_x production processes is estimated as 1675-1900 K. It is also known that the formation of thermal (Zeldovich) NO_x is rapid at high temperatures (above ~1800 K) especially if long residence times are encountered in such high temperature

7

regions. Near-stoichiometric combustion has highest adiabatic flame temperatures since just the right amount of air is present to oxidize all the fuel resulting in maximum heat release with no excess air left for dilution. The temperature in rich and lean burn zones is lower than stoichiometric combustion temperature due to higher heat absorption from the diluent air in fuel-rich zone and lower heat release due to less fuel present in the fuel-lean zone.
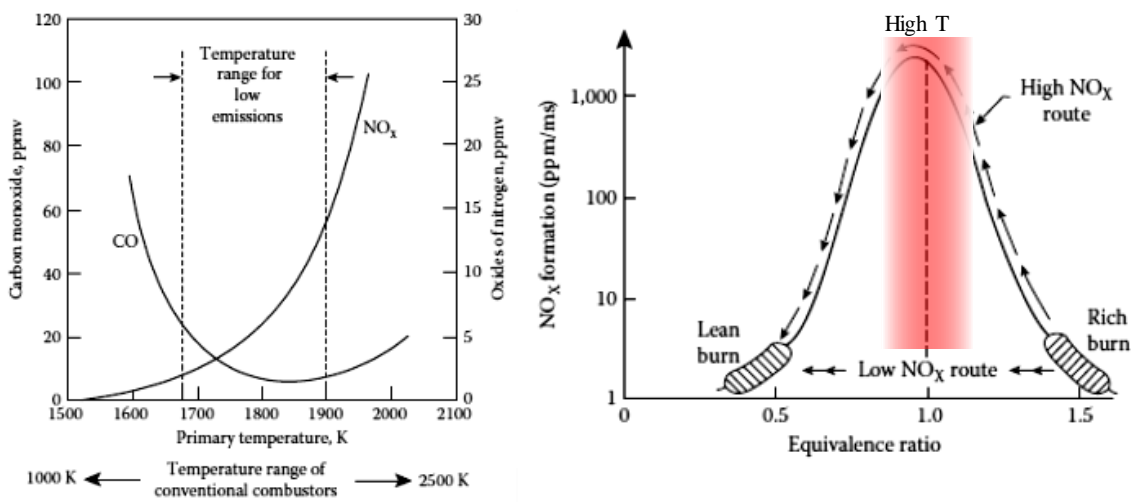
Figure 1.4: Trade-off between CO and NO$_x$ production at given temperatures (left). NO$_x$ production with equivalence ratio showing thermal NO$_x$ region (right) [19].

If the equivalence ratio is gradually decreased between rich-burn and lean-burn stages, the high NO$_x$ production route shown in Figure 1.4 is followed where the combustor operates near stoichiometric conditions during a portion of the process. To mitigate the NOx production, a quick-quench process is needed to avoid the stoichiometric operation while transitioning from rich-burn to lean-burn conditions as shown by the low NO$_x$ route in Figure 1.4. Hence, an effective quench section that allows fast mixing of fuel and air followed by rapid and stable combustion at lower temperatures is considered ideal for mitigating NO$_x$ production. In essence, an air-staged, RQL type combustor achieves lower

8

NO$_x$ by operating at lower overall temperatures in both fuel-rich zone and fuel-lean zone while avoiding near stoichiometric combustion in the quick-quench zone.
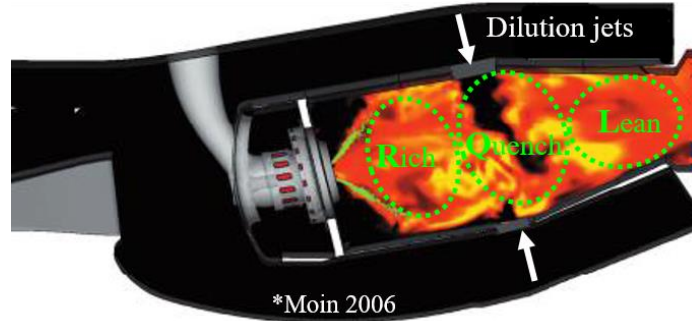
Figure 1.5: Instantaneous temperature prediction using LES in a Pratt & Whitney RQL combustor. Image adapted from Moin [16].

For illustration, an instantaneous temperature map predicted by Moin [16] using a Large Eddy Simulation (LES) of a Pratt & Whitney RQL combustor is shown in Figure 1.5. As expected, overall temperatures in rich-burn and lean-burn zones are low, however there can be some hot spots near the quench or quick-mix region. Therefore, for RQL to be effective, it is pertinent that the mixing of dilution air in the quench zone with rich combustion products is extremely fast. This is achieved by transversely issuing dilution air jets into the vitiated crossflow of products from the rich-burn zone. The background on flowfield and flame characteristics of such jets in crossflow (JICF) configuration is discussed in more detail in this chapter.

1.2.2 Premixed Fuel-Air Staged Lean Burn-Quick Mix-Lean Burn (LQL) Combustion

Lean Burn - Quick Mix - Lean Burn (LQL) combustion technology is an approach being developed to meet the future legislative requirements for low NO$_x$ emissions for aeroengines. The lean-burn combustors such as the single annular combustor (SAC) RR

LDI (shown in Figure 1.3) has demonstrated promising results with reduced NO_x at high power conditions (as compared to RQL) using fuel staging to obtain full combustor operability and turn down ratios [29].
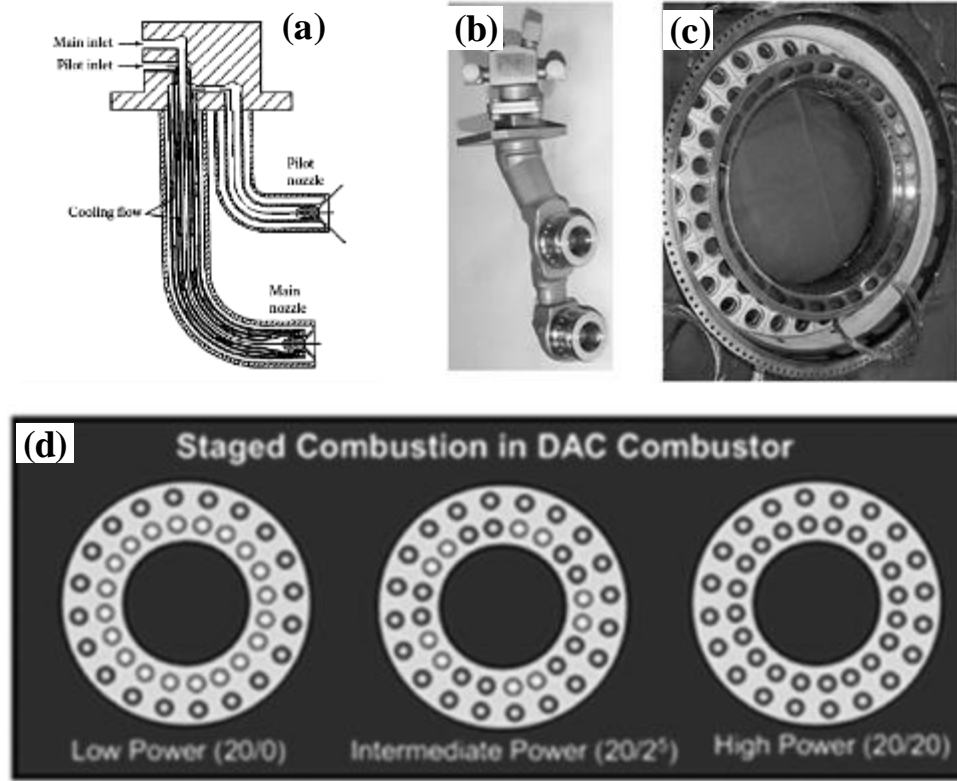
Figure 1.6: (a) DAC combustor fuel nozzle. (b, c)Fuel nozzle and dome hardware in DAC TAPS combustor. (d) DAC combustor operation routine at various power settings [18, 22].

In the DAC combustor shown in Figure 1.3 and Figure 1.6 (d), radial staging is utilized where fuel nozzles are spaced radially and are separated by a center body. The fluid path for the fuel nozzle is illustrated in Figure 1.6 (a). Here, the combustor equivalence ratio and temperature is maintained by controlling the fuel injection in these radially separated zones. For example, the dark circles shown in Figure 1.6 (d) for low, intermediate and high power modes represent the injectors that are fueled and ignited. The

pilot zone consisting of the fuel injectors located in the outer annulus can operate at up to $\phi \sim 0.8$ for low power settings. The local high ϕ helps mitigate the risk of lean instability. The main combustion zones (inner annulus) is fueled and ignited at high power settings, typically at approach conditions. Typically, lean combustion at $\phi = 0.6$ is used for both zones with the objective of attaining low NO_x and smoke reduction at high power settings [18]. Only some of the fuel injectors in the main zone are fueled at intermediate power level to increase the transition efficiency.
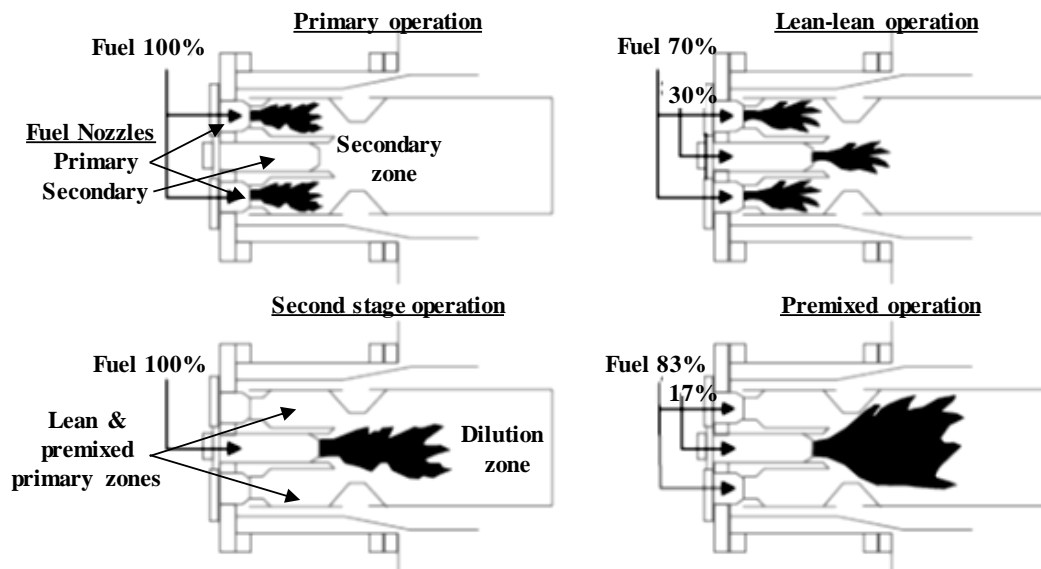
Figure 1.7: Architecture and operation modes of fuel staged GE DLN combustor [30].

The premixed fuel-air-staging developed for land-based gas turbines, e.g., GE's DLN (Dry-Low NO_x) combustor shown in Figure 1.7, has demonstrated reduction of NO_x emissions along with flexibility for natural gas and liquid fuel operation [30, 31]. DLN utilizes two premixed fuel-air stages that are designed for use with natural gas fuel and also have the capability of operating on liquid fuel. The primary and secondary zones along with their fuel nozzles are illustrated in Figure 1.7. All the fuel is injected through the

primary fuel nozzles in the primary operation mode, which is used for ignition to 20% load. Both primary and secondary nozzles are fueled in lean-lean operation mode, which is used for intermediate (20% - 50%) loads. Second stage operation with all the fuel carried through the secondary nozzle is used while transitioning between lean-lean and premix operation modes. Lastly, in premix operation mode which is used for 50% - 100% load, both primary and secondary nozzles are fueled but the flame is in the second stage only while premixing occurs in the primary zone. Premixed operation produces optimum emissions while reaching combustion reference temperature design point [30].

As shown with GE's DLN combustors, premixed fuel-air-staging has been successfully employed for gas turbines in power generation sector. The aviation industry is still evolving from non-premixed air-staged RQL combustors to premixed fuel-air-staged LQL combustion technology [32-35]. Both RQL and LQL techniques rely on JICF configuration for rapid mixing and combustion which is discussed in the following sections for non-reacting and reacting environments with non-premixed and premixed combustion.

1.3   Single Jet in Crossflow (JICF)

Overall, research on the single jets in crossflow (JICF) configuration has evolved extensively over several decades, in part due to their widespread application in air-breathing engines for dilution air jets, fuel/air mixers, film cooling, ramjet/scramjet fuel injectors, V/STOL aircrafts as well as in rocket engines for thrust vector control [34, 36-41]. Particularly, JICF application in staged combustion has been studied extensively, since it is considered to be a remarkably effective configuration to attain rapid and effective mixing of two dissimilar gaseous fluid streams.

1.3.1   Mixing and Velocity Field Characteristics of a Single JICF

The most widely studied JICF configuration is a single, unconfined jet in crossflow. In this configuration, a typically small diameter jet carrying a relatively small amount of mass issues vertically into a horizontal crossflow that has a relatively large amount of mass. The crossflow is able to turn the jet horizontally within a reasonable distance due to momentum transfer. This unconfined JICF configuration can be parameterized as a jet with mean velocity U_j injected perpendicularly into a crossflow of fluid traveling at mean velocity U_∞ as shown in Figure 1.8.
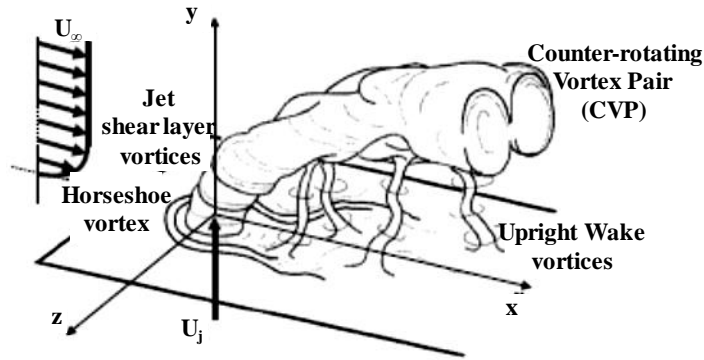
Figure 1.8: Characteristic flow features of an unconfined single JICF [9, 42].

The coherent vortical structures associated with the non-reacting unconfined single JICF have been studied by numerous authors and their findings are summarized here [9, 36, 42-45]. These distinct JICF flow features as illustrated in Figure 1.8 include: counter rotating vortex pair (CVP), jet shear vortices, upright wake vortices and horseshoe vortex system. The majority of the mixing in JICF is associated with the CVP. The interaction of crossflow and jets leads to roll up of jet shear layer which moves along the jet column and develops into CVP in the far field. Along the jet trajectory, the CVP continues to grow into

13

a dominant mixing structure in the downstream of the jet where the jet trajectory turns horizontal. Jet shear layer vortices are formed in the jet-crossflow boundary, especially along the windward shear layer. Downstream of the jet, the tornado-like upright wake vortices are formed extending from the bottom wall to the jet column. The flow visualization studies performed by Fric and Roshko [42] using smoke injection have confirmed the existence of wake vortices that result from the entrainment of crossflow boundary layer fluid into the jet column. The horseshoe vortex is another interesting feature shown in Figure 1.8; it initiates upstream of the jet exit and wraps around the main jet column. The horseshoe vortex originates from the separation and roll up of the oncoming crossflow due to adverse pressure gradient imposed by the jet which acts as a "non-rigid" fluidic blockage to the crossflow.

$$ J = \frac{\rho_j U_j^2}{\rho_\infty U_\infty^2} \tag{1.1} $$

The coherent structures deform and distort the jet/crossflow interface, which leads to the rapid entrainment of crossflow fluid into the jet. One of the most important controlling parameters that govern JICF mixing and velocity characteristics is the J ratio defined in Equation (1.1), which is the ratio of the momentum flux of the jet to the momentum flux of the crossflow. Here ρ_j is the jet fluid density, U_j is mean jet exit velocity, ρ_∞ is crossflow fluid density and U_∞ is mean crossflow velocity.

Acetone PLIF experiments performed by Smith and Mungal [46] measured the scalar concentration fields in JICF with high J ($25 \leq J \leq 625$) for a jet with a top-hat velocity profile. They found the scalar concentration in the jet potential core to be constant along

the jet center streamline and to decay with a rate proportional to $(s/d_j)^{-1.3}$ in the nearfield of the jet, where s is the arc length distance along the mean jet center streamline and d_j is the jet diameter. In the far-field of the jet, the concentration decay rate is notably lower. The distance at which the mixing decay rate changes from high to low, scales with J, and $s/d_j = 0.3J$ is suggested as a transition point between near field and far-field scaling in JICF [46].

More recent work by Su and Mungal [47] at J = 32.49 with a jet with a fully-developed pipe flow velocity profile suggests that the inlet velocity profile can strongly affect mixing in the jet nearfield region as compared to the J effect. Although most of the JICF mixing and velocity field studies have examined unconfined jets, the confinement effects have not been well studied. However, the existing knowledge of unconfined JICF flowfields sets the basic foundation for more recent confined JICF studies such as the one presented in this thesis.

Single JICF velocity fields obtained from Stereo Particle Image Velocimetry (SPIV) measurements conducted by Wilde [9] and Wagner [48] are presented in Figure 1.9 for reacting and non-reacting environments. While Wilde's study focused on understanding the dynamic response of unconfined jets, the research effort by Wagner, which was contemporaneous with the work presented in the current thesis, focuses on the effects of confinement on a single, premixed, ethylene-air jet in a high temperature $(T_\infty \sim 1500\ K)$ vitiated lean crossflow. It suggested that the jet trajectories can be significantly affected by the confinement for both reacting and non-reacting jets specifically for low J. The study indicates reduced dilatation or jet expansion due to heat

release in the presence of confinement, signifying the importance of jet-wall interaction in governing the flow-field [32].
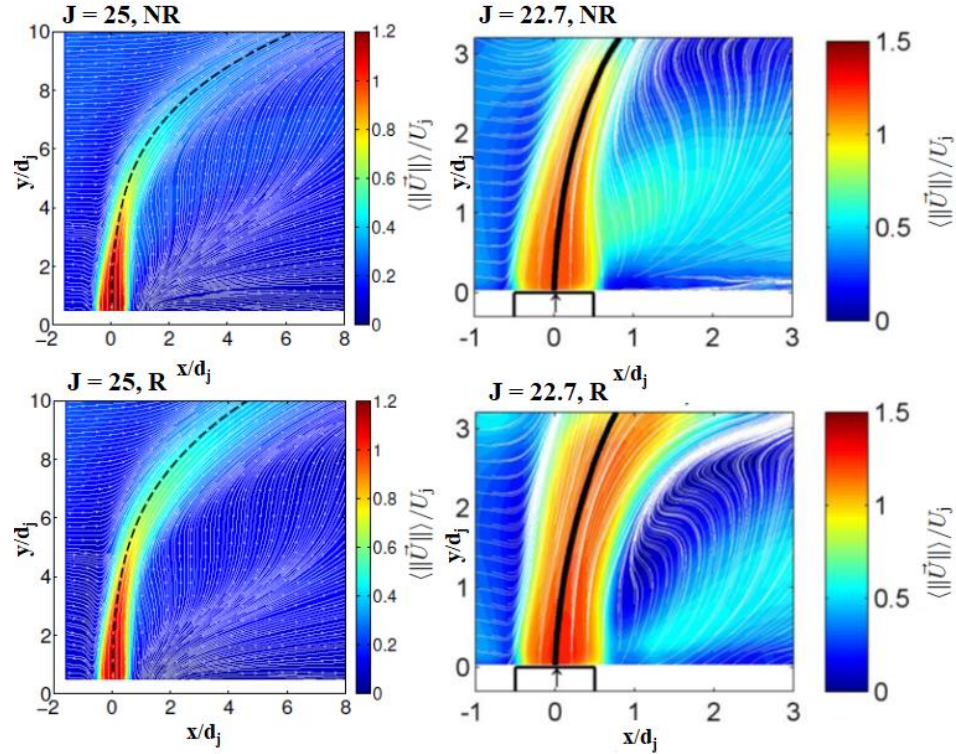
Figure 1.9 Average JICF velocity fields of non-reacting (top) and reacting (bottom). J =25, unconfined (left) [9]. J = 22.7 confined (right) [48].

These velocity field results show a stagnation region in the windward side of the jet, which is expected as the oncoming crossflow is obstructed by the jets and redirected to flow around the jets while stripping some of the jet fluid along with it. A two-dimensional velocity node is observed in the leeward side of the jets, which is consistent with the findings from other researchers [49, 50]. Also the velocity node is found to shift upstream at higher *J*. The streamlines on the leeward side can be seen to follow two divergent paths. The streamlines upstream of the node bend upstream (with negative velocity in the crossflow, x-direction) and are entrained into the jet. The streamlines downstream of the

16

node continue moving downstream along the wall and are not entrained into the jet within the observed field of view. On the windward side, the streamlines in the nearfield of jet first descend downwards (with negative velocity in y-direction) towards the bottom wall, then turn upwards and are entrained into the jet. This indicates the influence of pressure field on velocity. High pressure in the stagnation zone upstream of the jet deflects the crossflow and streamlines descend downwards at first. The low pressure region created in the leeward side of the jet from the aerodynamic blockage attracts the fluid flowing around the jets to turn upstream and fill in the wake region of the jet. For reacting jets, streamlines in the windward side show stronger descend since the dilatation from combustion introduces a stronger blockage. The heat release in reacting jets also increases the jet width as expected due to dilatation in the shear layer.
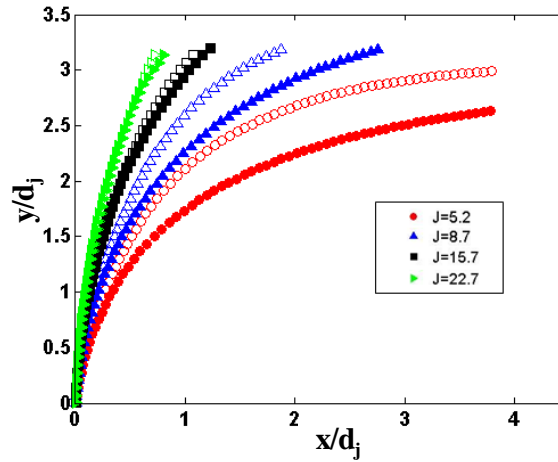
Figure 1.10: JICF jet trajectories based on the jet center streamline for non-reacting (closed symbols) and reacting (open symbols) cases for $5.2 \leq J \leq 22.7$ [48].

The jet trajectories shown in Figure 1.10 show that for unconfined conditions the reacting jets have higher penetration as expected due to an increase in velocity from the near field heat release and consequently increased local J [9]. In the case of lifted jet flames

17

with high J, the effect of heat release on jet trajectory is relatively small although it does induce acceleration in some regions. It has been suggested that a large reduction in density due to combustion adjusts for the flow acceleration while conserving the momentum [50]. For increased J, as the jet is expected to be more confined, the jet trajectory (defined as the jet center streamline), does not seem to change much between reacting and non-reacting cases (at least within the given field of view) as shown in Figure 1.10 [32]. Confinement seems to play a more important role on the jet trajectory and the windward flowfield than the presence of reactions and heat release suggesting a pressure driven flow field rather than heat release or dilatation driven flowfield. Although the ranges of J covered in the literature are much lower than the results presented in this thesis, the flow field characteristics of single unconfined and confined JICF discussed above provide a simplified understanding to further explore a more complex multiple CJICF scenario.

1.3.2   Flame Characteristics of a Single JICF

Traditionally, most of the research on JICF flames have focused on non-premixed fuel jets and recently some of the research has been performed to investigate the flame behaviors of premixed jets. Flame characteristics of air staged RQL type combustors with multiple CJICF have not been studied extensively. Typically, the amount of air required for oxidation of hydrocarbon fuels is much higher than the amount of fuel that needs to be oxidized. So, the air jets are expected to be much larger in size and carry higher amount of mass flow when compared to the jets used for fuel injection. However, the flame characteristics of single fuel jets such as flame stabilization modes, flame extent, attachment and lift-off behaviors that have been studied in the existing literature can be

used as a starting point to explore the multiple CJICF flame characteristics for air-staged and premixed-staged combustion systems.

Non-premixed JICF flames primarily show two distinct behaviors, i.e., attached and lifted flames. Mixing between the fuel and oxidizer is necessary for non-premixed flames, which strongly governs flame stabilization. For highly reactive fuel jets containing H_2/N_2 reactants, flame stabilization characteristics for low J jets injected into high temperature, vitiated air crossflow exhibit attached flames on the windward side near the jet exit, as shown in Figure 1.11 (adapted from Wilde et al. [9]).
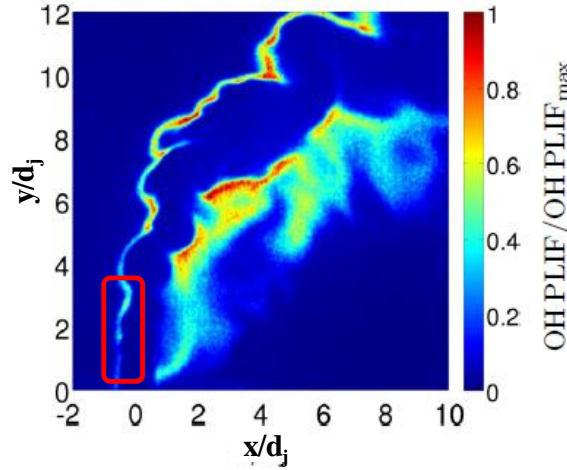
Figure 1.11: Instantaneous OH PLIF intensity result at J = 25 for H_2/N_2 fuel JICF showing attached windward flame [9].

In non-premixed, reacting JICF cases with a low temperature air crossflow, flame stabilization is expected to occur at the location where Damköhler number ($Da = \tau_{flow}/\tau_{chem}$) is of order one, i.e., where the chemical reaction rate ($\sim 1/\tau_{chem}$) is comparable to the rate of entrainment/mixing ($\sim 1/\tau_{flow}$). A study using simultaneous planar PIV and OH PLIF for high J, methane (CH_4) jets injected into low temperature air crossflows exhibited lifted jet flames suggesting a partially-premixed flame stabilization

19

mechanism [50]. In more practical staged combustor scenarios with a high temperature

vitiated crossflow ($T_\infty > 1000K$), however, the chemical reaction rates are much faster

(often by several orders of magnitude) due to an exponential temperature dependence, thus

resulting in much higher Da and hence can involve entirely different flame stabilization

mechanisms. At such high temperatures, the possibilities of autoignition and flame

stabilization at flow velocities and strain levels that are not possible otherwise (especially

on the windward side) clearly sets apart the JICF problem involving vitiated, highly

reactive fuels such as H_2/CO (in RQL) from the non-vitiated and lesser-reactive fuels such

as hydrocarbons (CH_4, C_3H_8 etc.) in LQL type JICF setup.

In a DNS (Direct Numerical Simulation) analysis of a low J, diluted fuel jet (70%

H_2, 30% N_2 by volume) with a moderate temperature (750K) air crossflow [51], flame

stabilization is noticed in the far-field on the leeward side of the jet, where the jet has

significantly deflected into the crossflow direction leading to low strain levels and near

stoichiometric mixture fraction. The intense shear in the windward side near the jet exit is

found to prevent flame stabilization despite the preheating and high reactivity of the H_2

fuel in the jet [51]. In this highly strained region, the shear layer vortices govern the rapid

mixing of jets and crossflow fluid. Another DNS analysis showed intermittent broken

flamelets in the highly-strained shear layer noting that the combustion occurs on the

windward edge in the far-field after complete jet deflection [52].

In high temperature, vitiated crossflows, flame stabilization can occur in the highly

strained windward jet shear layer [53] resulting in a nearly attached flame, even at high J

and very high jet Reynolds number (Re_j) [54]. At such high temperatures, the autoignition

time scales (τ_{auto}) are significantly reduced due to highly accelerated chemical kinetics

and autoignition is expected to play an important role in flame stabilization [55]. Shear layer flame stabilization has been studied with focus on velocity scaling of blowoff limits [56]. An investigation of non-premixed fuel jets injected into a high temperature ($T_\infty = 1390\ K$), high velocity ($U_\infty \approx 470\ m/s$) air crossflow proposed a three-region model in these highly-strained JICF "autoignition assisted flames". The initial lifted region consists of an autoignition kernel that supports a secondary region characterized as a premixed flame base followed by a non-premix, thickened and broken flamelets region [57].
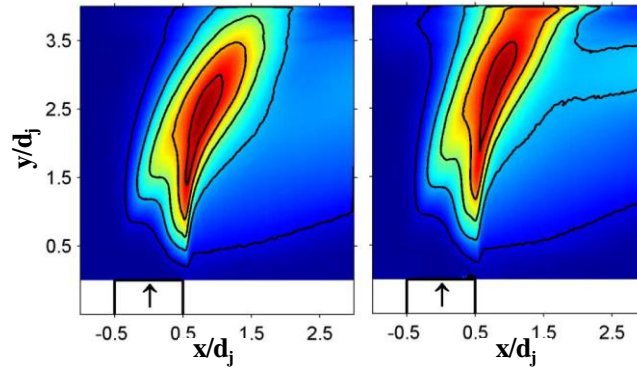
Figure 1.12: Mean chemiluminescence images for premixed ethylene-air single JICF under confinement for J = 15.7 (left), J = 22.7 (right) with 10%-90% of maximum intensity contour lines [32].

Premixed JICF flames studies are limited in traditional literature. Some recent work by Wagner et al. [32] and Schmitt et al. [58] studied flame stabilization and flow field characteristics of premixed jets for single JICF configurations. Wagner et al. [32] used ethylene-air jet injected into a vitiated crossflow of fuel lean pilot for low J (5-23) and studied the effect of confinement. The time-averaged result shown in Figure 1.12 reveals a lifted flame on the windward side and an attached flame on the leeward side. The confinement lead to jet impingement on the opposite wall for high J where a slight amount of heat release can be noticed upstream of the jet on the top wall. Wagner et al. [32] suggest

21

that based on the consistencies between strain rate and ignition delay time at the windward flame edge, autoignition is the dominant flame stabilization behavior.

1.4   Multiple Confined Jets in Crossflow (CJICF)

As mentioned earlier, most previous studies on jets in crossflow have focused on single jets in a quasi-infinite (unconfined) crossflow. These studies have examined characteristic flow features such as the presence of counter-rotating vortex pairs (CVP), horse shoe vortices and wake vortices that originate as the jets interact with the crossflow and wall boundary layer [36, 42-45]. These features, however, typically dominate only after a number of jet diameters downstream of the jet exit, whereas current trends in compact combustor designs depend on jet interactions close to the jet exit. Also, the majority of single jet in crossflow (JICF) studies involve fuel jets that are relatively small and are less confined in a crossflow. On the other hand, dilution air jets in RQL and premixed fuel/air in LQL approaches typically employ jets that are large in size relative to the cross stream dimension of the combustor and involve significant mass flow rate that is comparable to the crossflow. Thus the presence of confinement in modern compact combustors is a more realistic scenario than the typical unconfined JICF configuration in previous studies.

As noted in Section 1.2 on the RQL and LQL staged combustion techniques, rapid and effective mixing in the quick-quench region is typically achieved with multiple dilution air or fuel/air jets. Revisiting Figure 1.1 that illustrates an RQL type (RR Phase 5) combustor, the quick-quench region uses multiple confined jets in crossflow (CJICF) configuration, with rows of air jets issuing through the inner and outer combustor liners

22

into a crossflow of vitiated products from the rich "pilot" burners located upstream. The interactions among the jets, vitiated crossflow and liner walls control the interplay of mixing and combustion in the staged zones.

The mixing characteristics of multiple CJICF based on species and thermal mixing using probe measurements for single, double and opposed rows of jets both in-line and staggered was investigated by Holdeman [59] for circular and non-circular orifices that are typically used in gas turbine combustors to control or tailor the pattern factor. The numerical and empirical models developed through this and other studies highlight the important parameters such as the jet-crossflow momentum flux ratio (J), injection hole diameter (d_{jet}), hole spacing (s), test section height at injection plane (H), density ratio (S) and crossflow temperature (T_∞) [59-63]. Among these parameters, the J ratio defined in Equation (1.1) is found to be the most significant flow variable as highlighted earlier from single JICF literature. For constant J, these studies indicated the density ratio has a weak effect on jet penetration and profile shape. The effect of shape for the orifices that are symmetric with respect to the crossflow is significant only within the first few jet diameters downstream of the injection plane [64].

$$\theta = \frac{T_\infty - T}{T_\infty - T_j} \tag{1.2}$$

In the thermal mixing studies performed by Holdeman [59], illustrated in Figure 1.13, the temperature field is represented as plots of temperature difference ratio, θ defined in Equation (1.2), where T_∞, T_j and T are crossflow, jet and measured temperatures respectively.
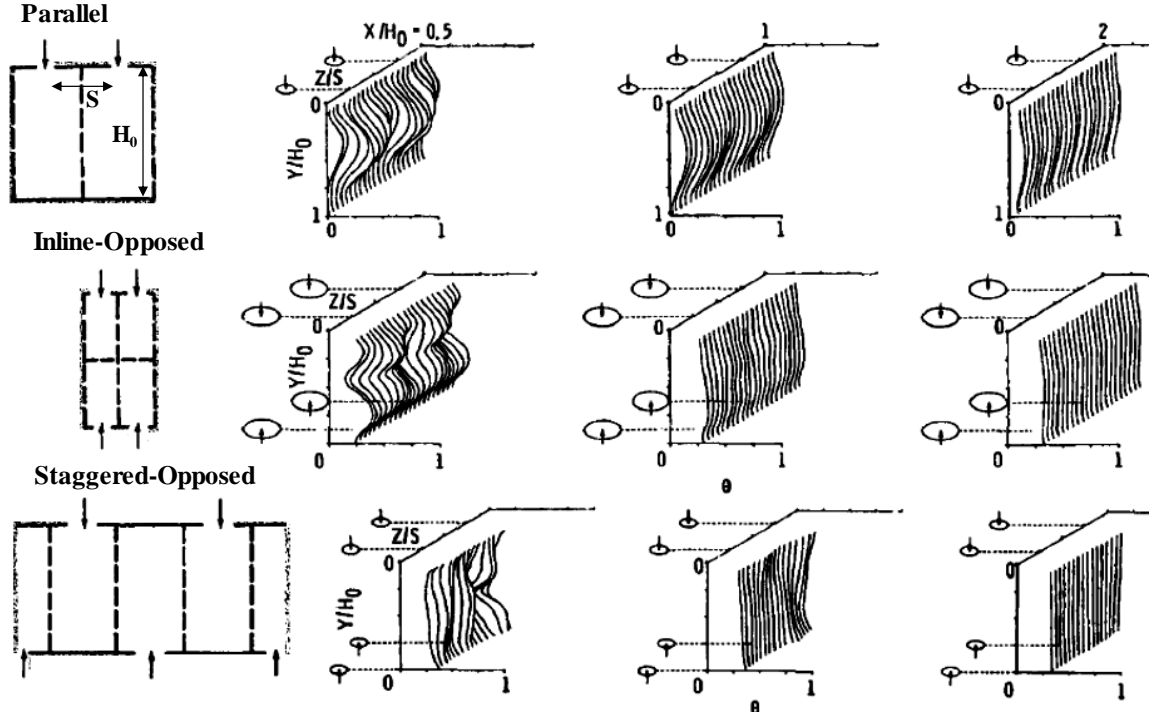
Figure 1.13: Comparison of thermal mixing profiles (parameter θ) for parallel, inline-opposed and staggered-opposed multiple CJICF configurations by Holdeman [59].

For multiple CJICF, the jet configuration can play an important role in mixing, as shown in Figure 1.13. For example, the mixing is enhanced if the alternate jets for optimum one-sided injection are moved to the opposite wall. In other words, with constant J, the optimum S/H_0 ratio (jet spacing/duct height) for staggered-opposed jets is double than that for single row jets where the optimum is defined based on achieving uniform temperature distribution in a minimum downstream distance [65, 66]. Opposed jets with in-line centers have shown better *initial* mixing than staggered configurations. In the downstream region ($x/H_0>1.5$, with x being the distance downstream of jet), staggered-opposed jets mix better than in-line opposed jets for high J ratios (i.e. J > 64) [40].

In conjunction with the flow field, the flame characteristics of reacting multiple CJICF demonstrate the physio-chemical processes involved in staged combustion. Most of

the previously published RQL research in this area was motivated to reduce NO_x emissions. Measured scalar quantities included species and temperature to understand mixing characteristics and the effects of temperature, pressure and mixing on NO_x emissions [24, 33, 34, 62, 67]. These studies suggest that: 1) an "optimum" mixing (not necessarily the most uniform) is required for low NO_x production, 2) the crossflow air preheat increases NO_x more than jet air preheat and 3) formation of prompt NO_x (in fuel-rich primary zone) is relatively insensitive to pressure while the thermal NO_x (in the Quench region) increases significantly with pressure.

Besides NO_x emissions, other flame characteristics for multiple jet injection, such as flame stabilization mechanisms, lift-off distances, combustion modes, and effect of heat release on the flow-field have received little attention in the literature. The velocity field of multiple CJICF has not been studied extensively either. So far, these issues have been examined primarily for unconfined, single jet configurations. The physio-chemical processes governing the mixing and combustion of multiple reacting jets in a highly confined and high temperature vitiated crossflow need to be explored further since it better depicts the practical scenario in aeroengines operating over a vast range of flight regimes [41] and in land-based gas turbines employing premixed fuel-air staging.

1.5   Objectives and Thesis Outline

To provide the knowledge needed to push the limits of air-staged (RQL) and premixed-staged (LQL) combustion technologies further, the objective of this thesis is to examine the flowfield and combustion characteristics in non-premixed air-staged (RQL) and premixed fuel-air-staged (LQL, Lean-Quench-Lean) combustor configurations. The

experimental and numerical investigations conducted here are designed to explore the following objectives:

1) Determine the unique mixing and flow field (e.g., velocity field) characteristics that distinguish highly confined multiple jets in crossflow from the widely studied, single, unconfined JICF situation. More specifically, the goal is to examine the impact of jet-jet and jet-wall interactions on mixing by varying jet configurations and other flow parameters.

2) Understand the controlling flame characteristics such as flame stabilization mechanisms, liftoff height and burnout distance involved in staging of highly confined reacting jets in a high temperature, vitiated crossflow. Specifically, the goal is to examine the non-premixed RQL (air-staged) type configuration currently employed in various aeroengines, and also premixed staging (LQL) where lean fuel-air jets are injected into a vitiated crossflow of lean combustion products.

The remainder of this thesis is organized around these two primary objectives. The experimental approach is detailed in Chapter 2, along with a description of the modeling approach used to examine chemical time scales. The experimental description includes an overview of the test facility and its subsystems, the control and measurement devices used to operate the facility, and the flow conditions tested. The chapter also describes the imaging diagnostics techniques employed in the experiments, namely particle image velocimetry (PIV), planar particle scattering and chemiluminescence imaging.

Flowfield characteristics of the multiple CJICF, including the results obtained from mixing and velocity field measurements, are presented in Chapter 3. The differences in mixing properties of staggered-opposed and parallel jet configurations are presented for

low to high confinement scenarios in non-reacting multiple JICF systems. Preliminary velocity field comparison in reacting and non-reacting conditions are drawn using low speed planar PIV measurements. High resolution velocity field results obtained in non-reacting environment using 10 kHz SPIV diagnostics technique are presented for the two jets configurations while exploring the effects of variation in air split and J ratios.

Chapter 4 examines the flame characteristics of CJICF under RQL operating conditions. Flame stabilization modes and flame boundaries (or extents of heat release) are studied using experimental results obtained from low and high speed chemiluminescence techniques along with the chemical reaction timescale modeling results. Differences in the average and instantaneous flame characteristics of staggered and parallel jet configurations are compared for CJICF conditions.

Similar flame characteristics are studied for LQL conditions in Chapter 5. Differences between the jet configurations along with non-premixed and premixed jet configurations are outlined for the instantaneous and mean flame properties. The effect of jet impingement on flame shapes for non-premixed and premixed flames are compared. Possible flame stabilization modes are studied by varying the amount of fuel supplied in the pilot, bottom and top jet flows.

The investigations performed in this thesis are summarized Chapter 6, including the observed relations between the flow field, its mixing characteristics and the combustion processes. Important conclusions from the present study and recommendations for future research work are also provided.

CHAPTER 2.   APPROACH

This chapter describes the experimental methodology used for the investigation of flame and flowfield characteristics of staged combustors presented in this thesis. An overview of experimental facility along with the advanced laser diagnostics and imaging techniques are presented here. In addition, the numerical and analytical methods used for data reduction and interpretation are presented in this chapter.

2.1   Overview of Test Facility

The experimental rig designed, manufactured and assembled for the CJICF studies performed in this thesis is illustrated using Computer Aided Design (CAD) graphics in Figure 2.1. The rig primarily consists of two major sections, namely, the pilot flow section and an optically accessible test section in which three jets are perpendicularly injected from the bottom and two jets are perpendicularly injected from the top. The pilot flow section consists of a low-swirl circular geometry pilot combustor which is 21.59 cm long and a 15.742 cm long transition piece that evolves from a circular to rectangular cross-section geometry test section that is 65.272 cm long, 7.62 cm in height and 10.16 cm in depth. There are a total of 5 jets that can be used to attain two jets configurations, namely staggered-opposed and parallel jet configurations. Each jet is 1.27cm (0.5 inch) in diameter (d_j), so the test section is $6d_j$ in height and $8d_j$ in depth. The quartz window for optical access from the side of the test section covers the entire height of the test section and is 20.32 cm (8 inch) or 16 d_j long. The side window extends $4d_j$ upstream and $12d_j$ downstream of the center of the jet injection plane.
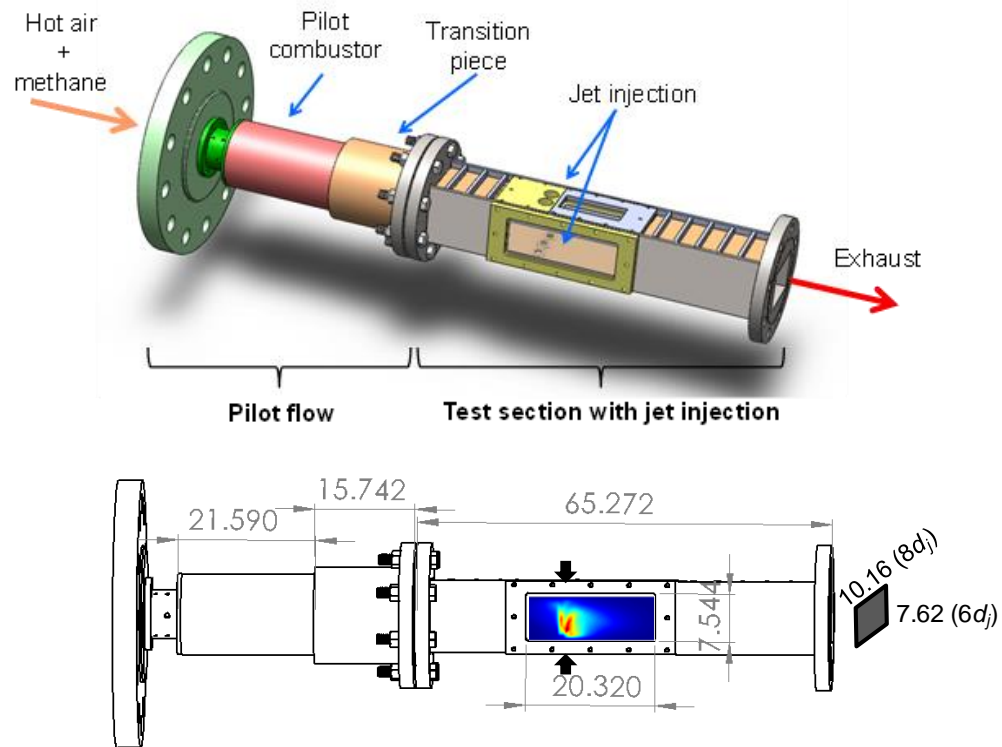
Figure 2.1: Rig assembly including pilot combustor, transition piece, test section with jet injection (dimensions in cm).
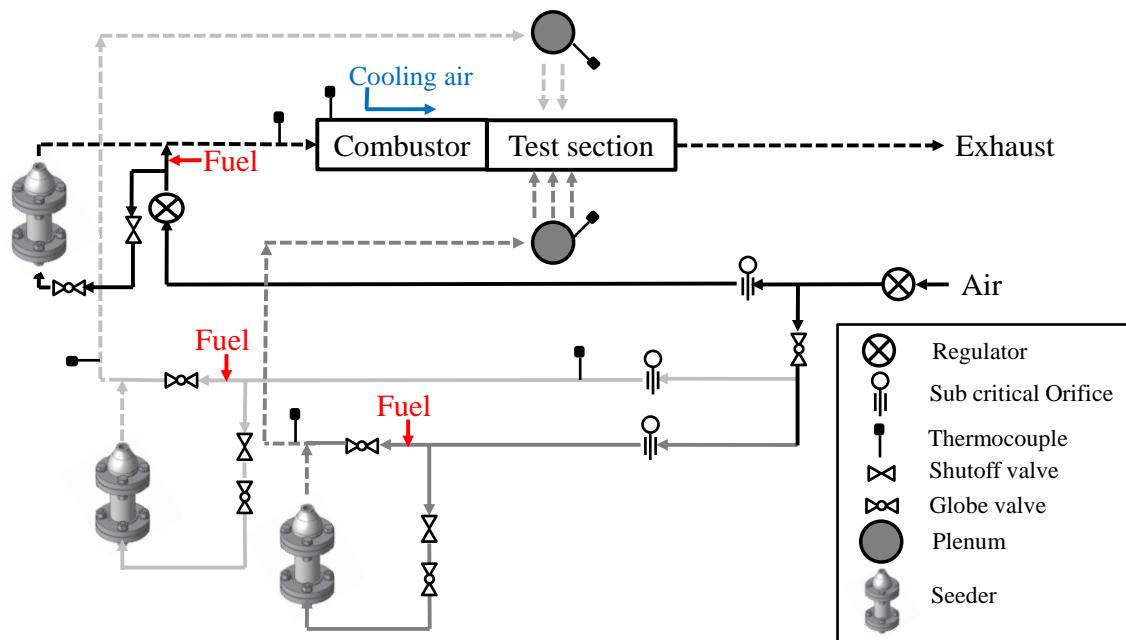
Figure 2.2: Schematic diagram of the multiple CJICF experiments flow facility.

The overall schematic of the flow facility developed for this study is shown in Figure 2.2. The air, from the high pressure supply in the BTZ Combustion Lab, is distributed between the pilot combustor air line, bottom jets air line and top jets air line. The air-split ratio (defined in Equation (2.1) as total dilution air mass flow rate through ALL the jets divided by the total air mass flow rate through the pilot combustor) is regulated using gate valves for each line. The fuel mass flow rates are negligible in comparison with the air mass flow rates and hence the air-split ratio (or split ratio) and the mass split ratio are essentially the same.

$$Air\ Split = \frac{\dot{m}_{a,jets}}{\dot{m}_{a,pilot}} \tag{2.1}$$

The total dilution air flow directed to the jets is further split among the bottom and the top jets as shown in Figure 2.2 and Figure 2.3 (a). Before entering the test-section, jet air is passed through plenums (settling chambers) for flow conditioning. These dilution air jets mix with the crossflow in the test section creating the quench region. In case of flame experiments, the secondary combustion follows the quench region where jets react with the crossflow containing vitiated combustion products from the pilot burner. For the flow diagnostics experiments, which involve particle scattering measurements, some of the air is also bypassed through three independently controlled seeders for the pilot flow, bottom jets and top jets. In reacting experiments, a simple cooling system is used to cool the surface of the pilot combustor and the test section windows using room temperature cooling air. A cooling air duct surrounding the pilot burner and the transition section is used along with several cold air jets that are directed to blow over the test section windows for cooling

purposes. Finally, the gases flow out of the test facility through an exhaust pipe into the building exhaust stacks. Various subcomponents that constitute the test facility are described in detail in the following sections.
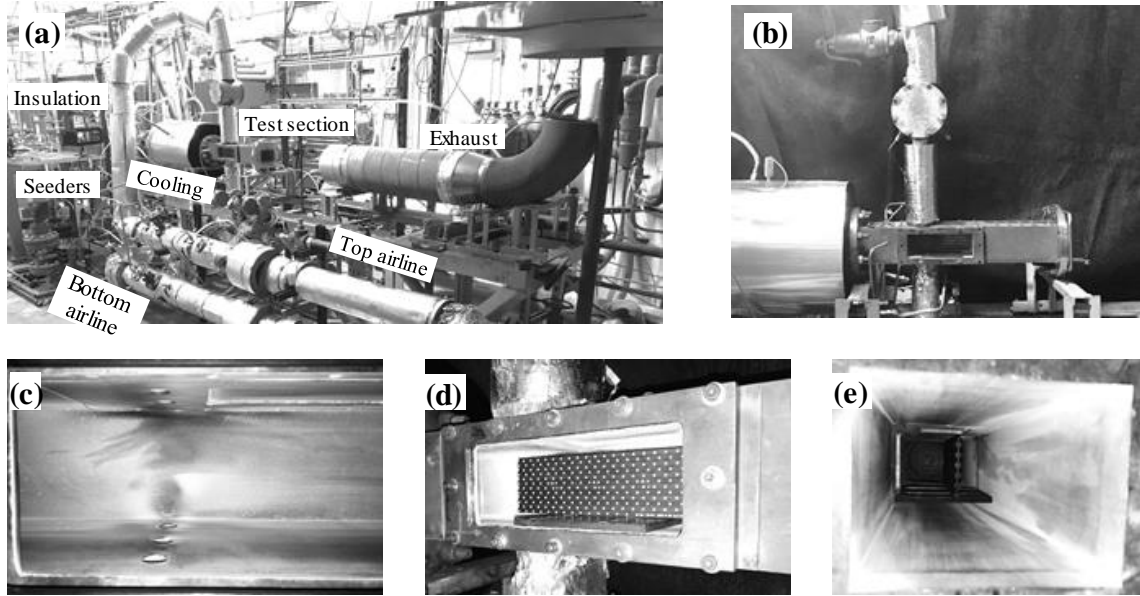
Figure 2.3: (a) Overall rig assembly hardware. (b) Test section hardware. (c) Test section inside view showing jet injection holes. (c) Calibration plate jig used for imaging diagnostics. (d) View from the exhaust end looking upstream at the pilot swirler and calibration plate.

2.2 Pilot Flow Section

The pilot flow section mainly consists of a low swirl stabilized pilot combustor and a transition section as shown in Figure 2.4. For flame measurements or reacting flow experiments, fuel (natural gas) at room temperature is premixed with the preheated air for the pilot flow and, in some cases, with the jets far upstream of the combustor using the fuel injectors shown in Section 2.6 to achieve a fully developed flow with a uniform fuel-air mixture. In the pilot flow, the premixed fuel-air mixture is then passed through a contoured nozzle into a ~40° vane angle swirler (swirl number ~0.5-0.6) with a 38 mm outer diameter.

This pilot combustor is derived from a low swirl burner design studied previously by Periagaram et al. [68].
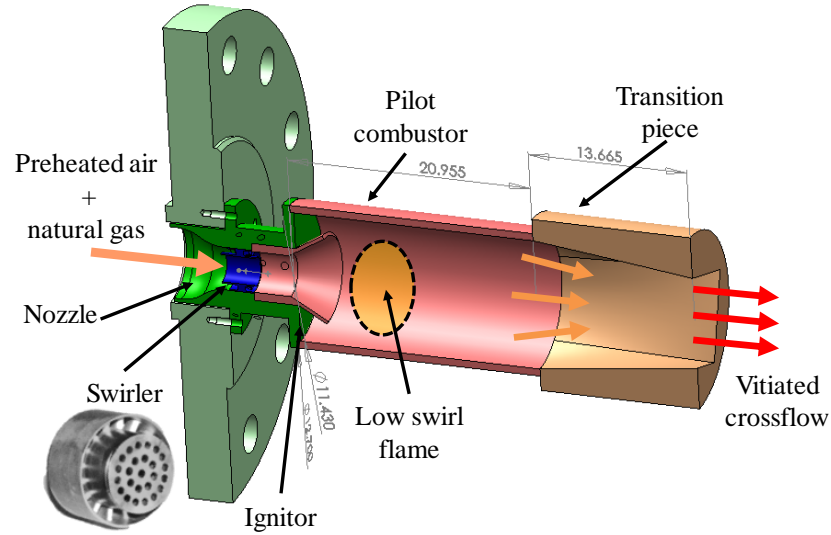
Figure 2.4: Pilot flow section subassembly consisting of the nozzle, swirler, pilot combustor and the transition piece.

As shown in the swirler image in Figure 2.4, the majority of the flow passes through a perforated plate in the center of the swirler such that mostly axial flow with low swirl is achieved in the pilot combustor. This low swirl flow is ignited using a high voltage spark and a H_2 fuel line which is injected in the recirculation region between the upstream pilot combustor wall and the center body. The burning gases are then passed through the pilot combustor pipe which is 21 cm long and has a circular cross-section of 11.4 cm inner diameter. The vitiated pilot combustor products are then passed through a 14 cm long transition piece that connects the circular cross-section of the pilot combustor to the rectangular cross section (7.6 cm height, 10.2 cm depth) of the test section as shown in Figure 2.4. This transition from circular to rectangular geometry further reduces the swirl to obtain a primarily axial crossflow that enters the test section. For the non-reacting

experiments, the same pilot flow section is used with room temperature or preheated air without fuel injection.

2.2.1 Vitiated Crossflow Temperature Distribution

The temperature distribution at the exit of the pilot burner ($\Phi_p = 0.57$, $T_{preheat} = 505°K$, $U_\infty = 15$ m/s) is characterized using an L-shaped, K-type shielded thermocouple inserted through a steel window blank with vertical slots to traverse the thermocouple. The cross section where inflow temperature is measured is located two jet diameters upstream of the jets. The jets are turned off for this pilot crossflow temperature characterization. The thermocouple probe measurement locations are illustrated in Figure 2.5 (a) and the pilot burner in operation is shown in Figure 2.5 (b). The flame image in Figure 2.5 (b) was taken by carefully placing an exposable inspection mirror which is then imaged using a low speed (15Hz) Foculus FO531TC color camera. The blue flame in the pilot burner is an indicator of lean-burn operation (at $\varphi_p = 0.57$).
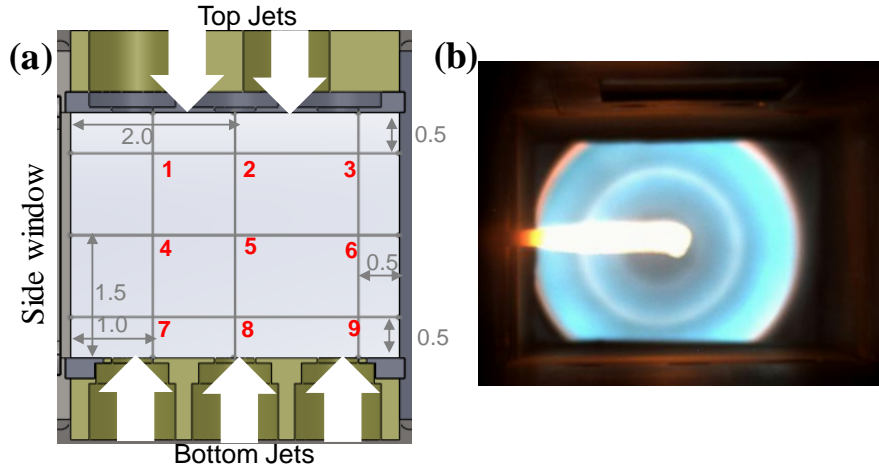
Figure 2.5: (a) Vitiated crossflow temperature measurement locations at a cross section ~2 d_j upstream of the jet injection plane. (b) Pilot combustor in operation as viewed from the downstream exhaust end.

Since the measuring thermocouple is exposed to the radiating walls, which are cooler than the gas temperature, the measured temperature is lower than the actual gas temperature. To get an improved estimate of the gas temperature, radiation corrections are applied using a heat transfer model for a cylinder in axial flow [69]. This model is primarily based on Equation (2.2) and (2.3).

$$Nu = CRe^e = \frac{hD}{K} \tag{2.2}$$

$$hA(T_g - T_p) = \varepsilon A\sigma(T_p^4 - T_w^4) \tag{2.3}$$

where, h = convective heat transfer coefficient; ε = emissivity (0.75-0.87 depending on oxidization level of the stainless steel); C =1.02-1.26; e = 0.5; T_w = wall temperature (assumed to be 505° K); and K = thermal conductivity and μ = viscosity. The latter two values are calculated for equilibrium combustion products and iterated for T_g using GasEq software.
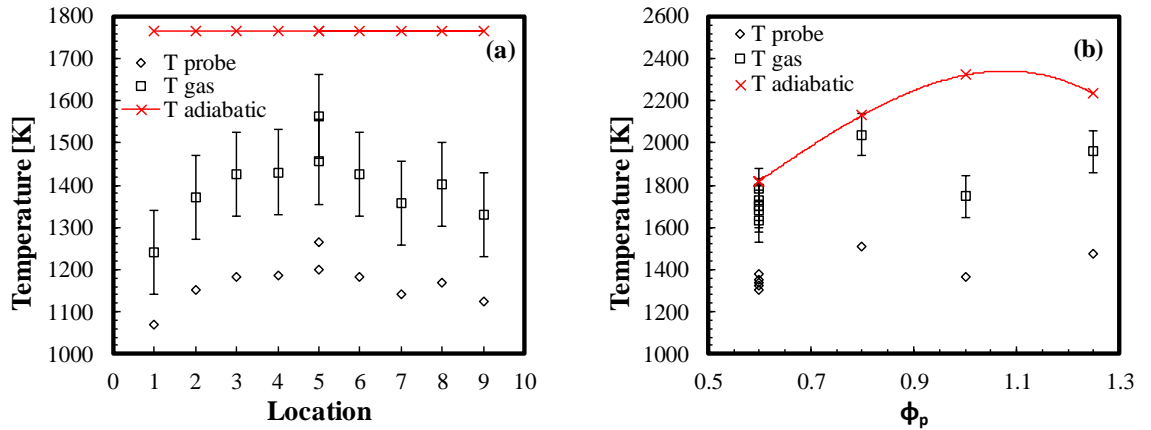
Figure 2.6: (a) Measure (T_{probe}), radiation corrected (T_{gas}) vitiated crossflow temperature distribution (ϕ_p = 0.57, $T_{preheat}$ = 505°K, U_∞ = 15 m/s, jets off). (b) Crossflow temperature at varying ϕ_p (jets on).

The measured temperatures and radiation corrected inflow temperatures are shown in Figure 2.6 (a) at the nine locations illustrated in Figure 2.5 (a). The central part of the cross-section, e.g., location 5, is hotter due to lower heat losses compared to locations near the walls. Overall, the temperature profile indicates a fairly uniform crossflow upstream of the jet injection location. The average radiation corrected temperature is ~1400 K (estimated error +/- 100 K) while the adiabatic flame temperature for the shown conditions is 1764 K. During a difference set of experiments, the crossflow temperature was characterized again in the center of test section (location 5 in Figure 2.5 (a)) for various Φ_p (0.6, 0.8, 1.0 and 1.25) to estimate the crossflow temperature for RQL and LQL experiments presented in this thesis. The repeated temperature measurements shown at Φ_p = 0.6 are carried with Φ_j = 0, 0.3 and 0.6. The takeaway from this set of experiments is that for the Φ_p =0.8, 1.3 which are of interest for the RQL and LQL experiments presented in this thesis, the measured crossflow temperature ($T_{\infty, measured}$) is roughly equal to 1500 K and the radiation corrected temperature can be approximated as T_{∞} ~1800-2000 K. This temperature follows from heat losses in the pilot flow section, as the adiabatic flame temperature of the pilot combustor is 2200-2400 K. Considering this temperature range and atmospheric pressure, the pilot crossflow mass flow rate corresponds to a velocity for reacting cases of ~35 m/s.

2.3   Test Section and Dilution Jets

In the test section, dilution air (for RQL) or the premixed fuel-air jets (for LQL) is injected normally into the crossflow of pilot combustion products for rapid mixing and combustion. For the non-reacting experiments such as for mixing and velocity

measurements, the same facility is used with room temperature or preheated air without using the fuel.
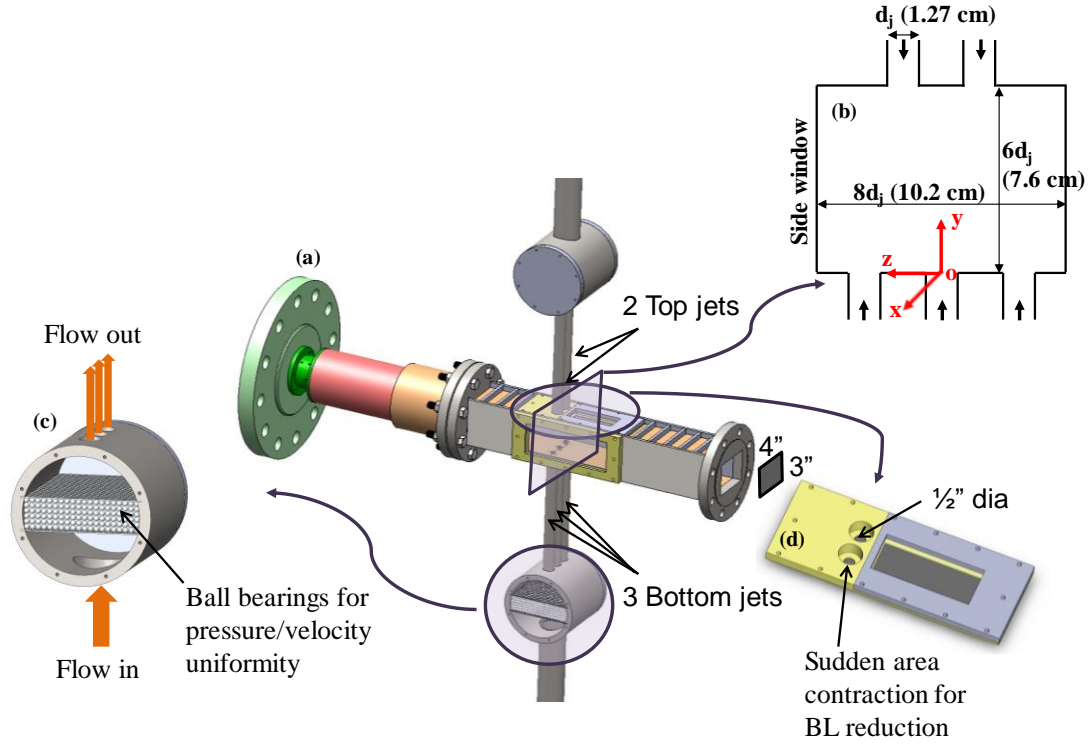
Figure 2.7: (a) Test section assembly including 3 bottom jets and 2 top jets. (b) Cross-section at jet injection plane and the coordinate system. (c) Plenum design with ball bearing arrangement. (d) Sudden area contraction design for jet injection.

As shown in Figure 2.7, a total of five jets (three on the bottom and two on the top of the test section) can be used to attain two jet configurations namely: (1) staggered-opposed jets with 3 bottom and 2 top jets on; or (2) parallel jets with either just the 3 bottom jets or just the 2 top jets on. Each jet has an inner diameter of 12.7 mm and the jet centerline spacing (the distance between centers of jets on each side) is 28.6 mm. The test section has optical access from two faces which are referred to as the side window and the top window. The side window extends throughout the height (6 d_j) of the test section and covers a large portion of the axial length (16 d_j) as mentioned previously in Section 2.1.

2.3.1   Flow Conditioning Section

Before the jets enter the test-section, the gases are passed through the plenums or settling chambers that have an arrangement of steel balls in order to create a uniform flow distribution among the various jets connected to the same plenum. The arrangement of steel balls also helps in preventing flashback for the runs with premixed fuel-air jets; pressure relief valves are installed just upstream of each plenum for added safety against flashback. The jet air passes through a sudden area contraction before entering the test section; this jet boundary condition, rather than a fully developed inlet, was chosen to more closely match typical engine hardware such as the holes in a combustor liner. Fully-developed injection without the sudden contraction adds additional boundary layers that can alter the interaction between the jets and the pilot flow.
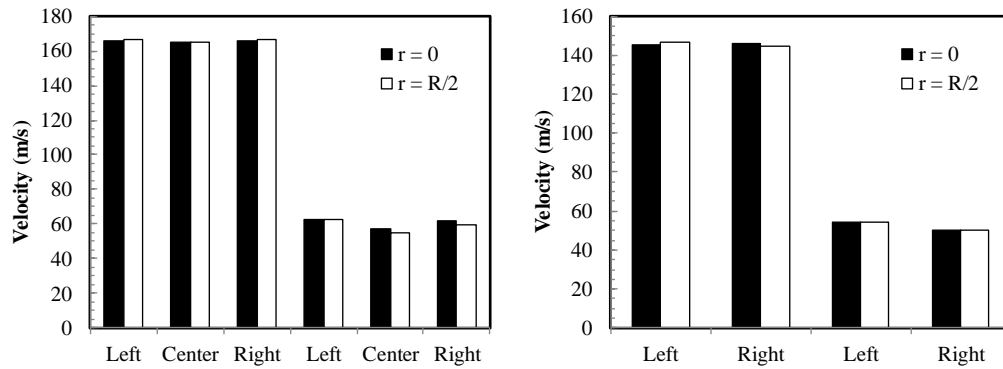
Figure 2.8: Uniform jet velocities from using plenums for 3 bottom jets (left image) and 2 top jets (right image), measured for high and low velocities using a pitot probe

Standalone testing is done for characterization of each plenum before the final assembly. The jet velocities for each jet welded to the bottom and top plenums are measured using a pitot probe at two radial locations and for two flowrates which cover the nominal flowrate conditions used throughout this study. Velocities are calculated by using

the isentropic flow Equation (2.4) and its derived Equation (2.5) with c, speed of sound defined in Equation (2.6) assuming room temperature (297.65 K) and R, gas constant for air (286.9 J/kg/K); γ, ratio of specific heat for air as 1.4.

$$\frac{P_0}{P} = \left(1 + \frac{\gamma - 1}{2} M^2\right)^{\frac{\gamma-1}{\gamma}} \tag{2.4}$$

$$V = c \sqrt{\frac{2}{\gamma - 1}\left(\left(\frac{P_0}{P}\right)^{\frac{\gamma}{\gamma-1}} - 1\right)} \tag{2.5}$$

$$c = \sqrt{\gamma R T} \tag{2.6}$$

The results from these velocity uniformity tests are presented in Figure 2.8 (a) for the three bottom jets and in Figure 2.8 (b) for the two top jets at each radial location and for the two different flowrates. For the jets connected to a single plenum, the velocities are found to agree within 1%. These results validate that the plenums distribute the incoming air equally among all the jets and also validate that the sudden area contraction method used for boundary layer reduction in the jet velocity exit profile is effective. Further analysis of the jets exit profile is presented through velocity measurements performed using the PIV technique.

2.4 Instrumentation and Controls

The flow facility is remotely monitored and controlled using LabVIEW data acquisition (DAQ) software which is linked with the National Instruments DAQ hardware

consisting of various modules such as NI9213 (for thermocouple voltage signals), NI9205 (for pressure transducer voltage signals), NI 9203 (for pressure transducer current signals) and NI9476 (for voltage output to control solenoid valves). The user interface for LabVIEW controls is show in Figure 2.9 for illustration. Note the flow parameter values shown in this illustration are arbitrary since the system was not running.
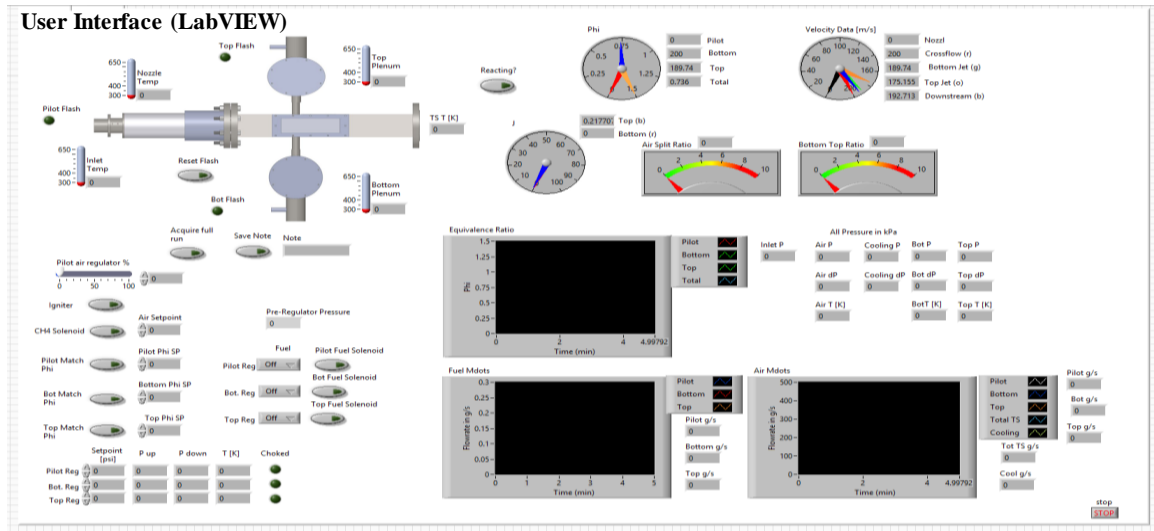
Figure 2.9: User interface developed to monitor and control the experiments using NI LabVIEW software.

Primarily two physical quantities, i.e., temperatures and pressures, were measured using relevant voltage and current measurement devices from which the derived quantities such as velocities, flow rates, *J* ratios, and split ratios were derived. A total of 12 thermocouples, 12 static pressure transducers, 4 differential pressure transducers, 5 solenoid valves, 5 flow regulators and a vortex flow meter were the instruments that were used and integrated with the LabVIEW software. These instruments along with their relevant identification properties are summarized in APPENDIX A.

39

2.5 Air Supply

For the reacting premixed jets experiments, preheated air is drawn from a high pressure (1000 psi) air supply, and the cooling air is drawn from a room temperature, low pressure (125 psi) supply. The facility is run in a blow-down mode with the test section at atmospheric pressure; the preheater can support up to 500-600 K temperatures when proper heat insulation is used over the air pipe lines. For the non-reacting CJICF flow field measurements, room temperature air from the high pressure (1000 psi) supply is used and no cooling air is required. The supplied air is split between the low-swirl pilot combustor and the staging jets as described in Section 2.1.

2.5.1 Air Flowrate Measurements

The air supply, fuel supply and particle seeding are separately monitored and controlled for three flows: 1) the pilot flow, 2) the top jets and 3) the bottom jets. The air split ratio (defined in Equation (2.1)) is regulated manually using globe valves. The mass flow rate of preheated pilot air is metered using a subcritical orifice plate instrumented with an Omega PX725A-1KGI pressure transducer to measure the upstream air flow pressure, an Omega PX771A-025DI differential pressure transducer to measure the differential pressure and K-type thermocouples to measure the air temperature. As the experimental facility evolved over time, a vortex flow meter was used for pilot air flow measurements. For the measurement of air mass flow rate in the bottom and top jets, similar subcritical orifice plate air flow meters are used. These are instrumented with upstream static pressure transducers (Omega Dyne Inc., PX309-500G5V), differential pressure transducers (Rosemount, 1151DP4522BIDF) and K-type thermocouples. The cooling air mass flow

rate is also measured using a subcritical orifice plate metering system equipped with an Omega PX181B-500G5V static pressure transducer, an Omega PX771A-100WCDI differential pressure transducer and K-type thermocouple. Specific details of the chosen instruments are tabulated in APPENDIX A.

2.5.2 *Seeded Air Supply*

The facility is equipped with three separate individually controlled seeders to selectively seed each of the three flows (pilot, bottom jets and top jets) using bypassed air from each line downstream of the subcritical orifices such that the air flow rates through the seeders are accounted for. The air is bypassed upstream of the globe valves and reintroduced into each line downstream of the globe valves as shown in Figure 2.2. Each seeder is equipped with a gate valve and an On/Off type ball valve. Once the flowrate through each seeder is fine-tuned using the gate valves, the ball valve is used to operate the seeders.

The particle seeders, with the design shown in Figure 2.10, are used to add alumina (Al_2O_3, 5 µm mean particle diameter) particles in the low speed PIV experiments and Dupont R-960 titanium dioxide (TiO_2, 0.5 µm mean particle diameter) particles in the high speed SPIV experiments. To avoid agglomeration of the particles between the experiments due to atmospheric humidity, the particles are baked in an oven at ~400°F for several hours. Prior to each experiment, freshly baked particles are filled in the cone at the bottom of the seeder.
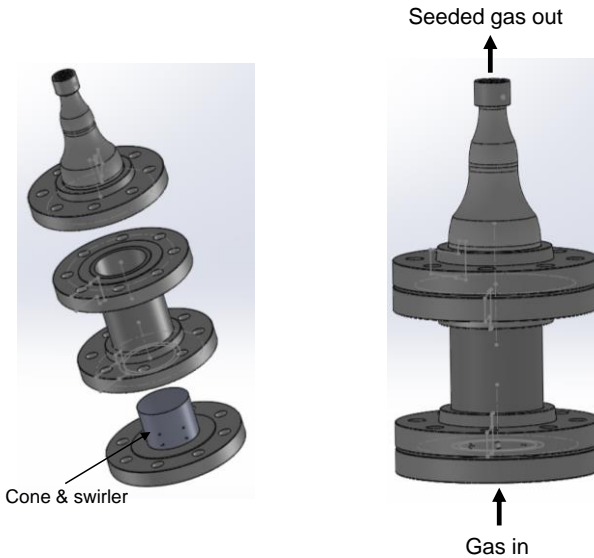
Figure 2.10: Particle seeder used for flow diagnostics experiments.

Air entering the seeder from the bottom passes through a swirler and picks up the seeding particles from the cone and produces a swirling fluidized bed in the middle chamber. The centrifugal momentum introduced in the swirling flow pushes the large particles radially outward to impinge on the wall and fall back in the cone with gravity. A perforated plate (not shown here) is used between the inlet pipe and the swirler to avoid the particles from clogging the inlet. It is deemed necessary to choose the bypass and reentry locations across the globe valves or 90° bends since they provide significant pressure difference (~10-30 psi) to overcome the pressure losses in the seeder due to flow constrictions from the perforated plate, swirler and the seeding particles.

2.6   Fuel Supply

For the reacting flow experiments involved in the RQL and LQL studies, fuel (natural gas) at room temperature is premixed with the preheated air for the pilot flow and the jets (for the premixed jets study) far upstream of the pilot combustor and the test section

to achieve a uniformly premixed fuel-air mixture. The fuel flow rate is low compared to the air flow, and since the premixing occurs far upstream, it is safe to assume the fuel is in thermal equilibrium with the preheated air at the pilot and jets inlets. For primary operation of the rig, natural gas is supplied from the building's 125 psig system. Bottled H_2 gas regulated from ~2500 psig to ~150 psig is used for the initial ignition along with a high voltage spark near the premixed fuel inlet as described in Section 2.2.

2.6.1 Premixed Fuel Injectors

In order to achieve a uniform fuel-air mixture within a short distance (~ 30cm) in the flow, a fuel injector assembly as shown in Figure 2.11 is designed and installed in the 5.08 cm (2 inch) air pipe lines. In each premixing location, fuel is split into four stainless steel tubes (6 mm outer diameter), each with four small injector holes (0.53 mm diameter) producing fuel jets in the air crossflow configuration, as shown by the small arrows in Figure 2.11. The holes are sized carefully such that the nominal jet trajectories at the lowest flow rates used in these experiments are able to penetrate sufficiently into the air lines so as to impinge at the opposite walls or impinge on an opposite facing jet within a short distance (~ 30cm) using the jet trajectory relations reported in previous studies [50]. In each line, two or three ninety degree bends and long flow lengths of ~1.5 m, 2.1 m and 3.7 m between the fuel injectors and pilot, bottom jets, top jets respectively are used to further ensure a uniform equivalence ratio at the pilot burner inlet and at the jet exits.
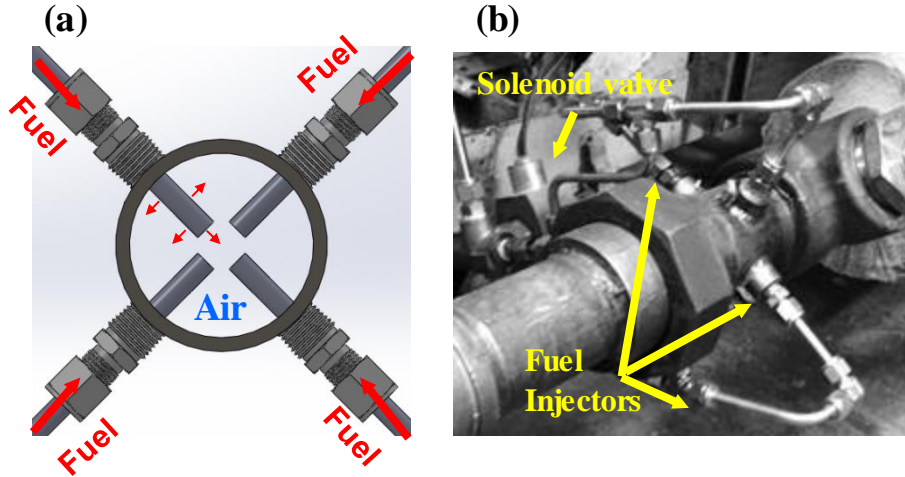
Figure 2.11: Fuel injectors design and installed hardware used for premixing fuel with air.

The fuel injectors shown in Figure 2.11 are used in the experiments that involve high speed chemiluminescence technique. In low speed chemiluminescence experiments reported in this thesis, preheated air and methane is premixed using a jet in coflow configuration at the head of a 1.8 m (6 ft) long, 85 mm (3.36 in) dia. straight pipe section before entering the low swirl pilot combustor. The straight pipe section also allowed for the flow to be fully developed and for the relatively cold fuel and preheated air to be fully premixed before the reactants enter the pilot combustor.

2.6.2   Fuel Flowrate Measurements

The fuel flow rates are remotely controlled using Tescom (ER 3000SI-1) regulators equipped with Omega Dyne Inc, PX309-5KG5V pressure transducers that measure the upstream stagnation pressure. The fuel mass flow rate is measured with critical orifices (O'Keefe: V-43-SS, V-26-SS, V-21-SS for pilot, bottom and top jets, respectively). Omega PX409-1.0KGI pressure transducers are used upstream of the critical orifices to measure

the stagnation pressure and Omega PX309-200G5V pressure transducers downstream of the critical orifices are used to confirm if the flow is choked. K-type thermocouples are used to measure the fuel temperature which is nominally room temperature. The fuel flow rates are shut on and off remotely using ASCO (Red Hat II) solenoid valves for safety. Each critical orifice plate is calibrated using a drum meter for upstream pressures ranging from 100-600 psi which is sufficient to cover the fuel flow rate conditions covered in this thesis. The calibration curves along with the necessary instruments are presented in APPENDIX A.

2.7 Optical Diagnostics Techniques

Diagnostics techniques including particle scattering and chemiluminescence imaging are used in this thesis to elucidate the flame and flow field characteristics of staged combustors involving CJICF. Particle scattering images using a low speed (15Hz) planar PIV setup are obtained in a non-reacting and reacting environment for preliminary velocity field analysis. An advanced high speed (10 kHz) SPIV system is used for mixing and three dimensional velocity field analysis in a non-reacting environment. Five measurement planes as shown in Figure 2.12(b) are used to perform the flowfield analysis. To characterize the flame properties in RQL systems, a low speed (10Hz) visible line-of-sight chemiluminescence technique is used for preliminary analysis. For a more detailed study of RQL and LQL flame characteristics, a high speed (10 kHz) line-of-sight OH* chemiluminescence technique is employed. Detailed diagnostics setups corresponding to each of these techniques are discussed in the following sections.

2.7.1 *Particle Scattering Imaging*

2.7.1.1 Low Speed (15 Hz) Planar PIV Setup

The low speed (15 Hz) planar PIV system used for the preliminary velocimetry of non-reacting and reacting CJICF is shown in Figure 2.12 (a). This system is equipped with a Big Sky 532 nm, ND:YAG laser and Lavision Imager ProX PIV camera, long focal lens and 532 nm notch filter to capture only the scattered laser light. The sheet forming optics include three 532nm mirrors (25.4 mm diameter) for beam turning, long focal length (750 mm) spherical lens (50.8 mm diameter) and a short focal length (15 mm) cylindrical lens to form a ~200-300 μm thick diverging sheet. The laser sheet enters the test section vertically at an inclination from the top window as shown in Figure 2.12 (a) and illuminates the flow which is seeded with 5 μm sized aluminum oxide (alumina) particles.
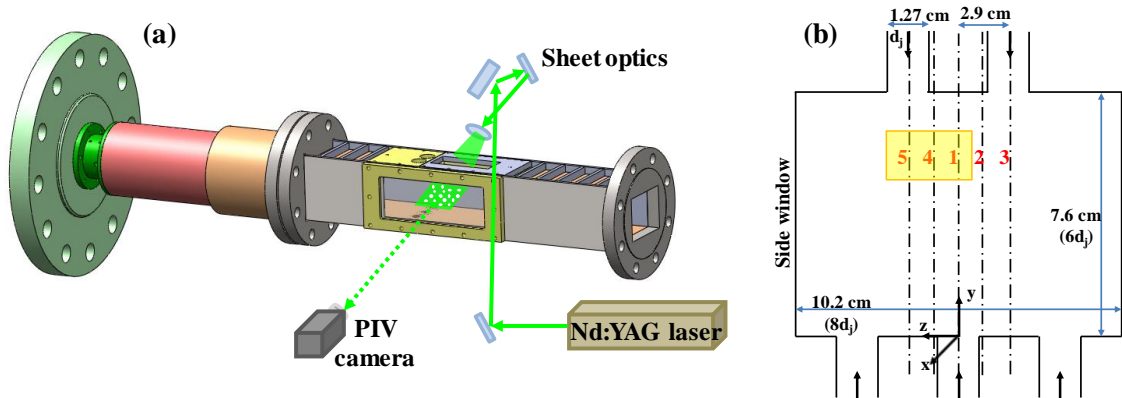
Figure 2.12: (a) 15 Hz low speed planar PIV system with laser sheet entering the test section from the top window. (b) Laser sheet planes defined for PIV measurements (planes 1, 4, 5 are used for low speed PIV measurements).

Three PIV measurement planes are studied where the vertical laser sheet passes through planes 1, 4 and 5 as shown in Figure 2.12 (b). Plane 1 refers to the center plane of the bottom jet located in the middle of the test section. Plane 4 (and plane 2) refers to the

intermediate plane between the middle bottom jet and the neighboring top jets. Plane 5 (and plane 3) corresponds to the center plane of the top jets. In most of the low speed PIV experiments presented here, 200-500 images are captured for each case at 15 Hz, under double frame, double exposure mode. The magnification of the optical system results in a scale factor of 6.945 pixel/mm. Multi-pass iterations in vector post-processing are chosen using a decreasing interrogation window size from 64×64 pixels after the first pass to 32×32 pixels for the second pass with 50% overlap in each pass. The goals is to have at least 10-20 particles in the interrogation windows. Since the vertical jet velocities can be as high as ~350 m/s for high air split ratio (~2), a nominal 5μs delay time (Δt) between the two laser pulses is used.

The DaVis^{TM} 7.2 software from LaVision is used for PIV post-processing with "subtract sliding minimum over time" feature enabled to reduce the background signal in the PIV images. For this purpose, 10-20 images are used for sliding background subtraction. To provide a meaningful region of interest, the area where the laser sheet is absent is masked out. In order to reduce outliers, correlation peaks are accepted in the defined range for V_x = 0-200 m/s and V_y = 0-500 m/s. A median filter is used to remove outliers by choosing the parameter "remove/replace if difference to average is greater than 1.8 times the rms of neighbors" in the DaVis software. Empty spaces are filled by vectors using the interpolation feature built into the software. From these instantaneous vector data, average and rms velocity fields are computed. Same diagnostics setup is used for both non-reacting and reacting flow conditions, however quality of images is reduced in reacting scenario firstly, due to inefficient seeding and secondly, due to adherence of seed particles on the quartz window.

2.7.1.2   High Speed (10 kHz) SPIV Setup

The diagnostics setup used for particle scattering measurements performed to study mixing and velocity fields in cold non-reacting CJICF experiments is shown in Figure 2.13(a). The particle scattering images are captured using two Photron SA5 cameras in a side scatter configuration where the angle between the two cameras is roughly 25°. Each camera is equipped with a Tokina lens (AT-X PRO, Macro 100 F 2.8D) mounted on a LaVision Scheimpflug adapter and a narrow band interference filter (Semrock Brightline 527/20). The f-number ($f/4.0$) is used to capture the images of elastic scattering from the seed particles. Image resolution of 704 x 520 pixels is used and the cameras capture a region (height = 76mm, length = 128 mm) spanning from the top to bottom of the test section and ~$2d_j$ upstream to ~$8d_j$ downstream of the jet injection plane. For each reacting case, 31274 single images at 20 kHz (or double frame 15637 image pairs at 10 kHz) are captured so the total data acquisition duration for each run lasts for ~1.5 s.
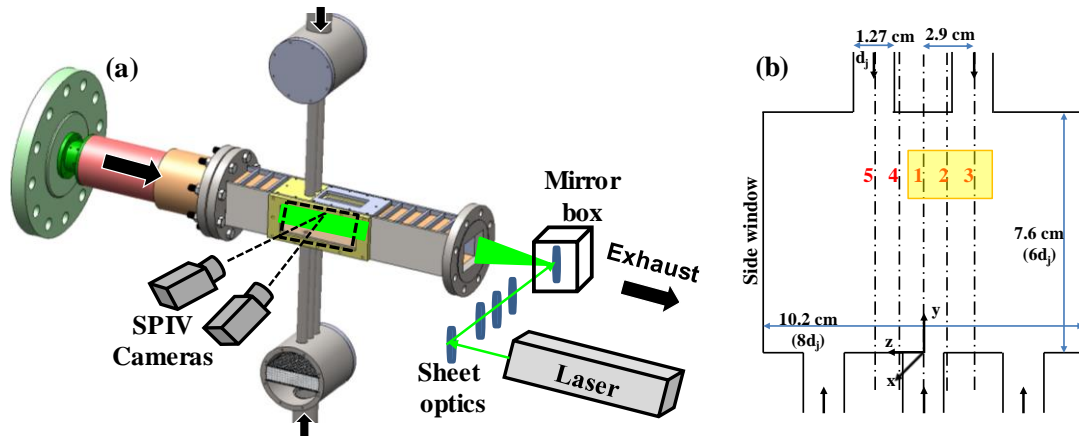
Figure 2.13: (a) 10kHz high speed SPIV system with laser sheet entering the test section from exhaust. (b) Planes 1, 2, 3 used for high speed SPIV measurements.

This setup employs a dual-head, frequency-doubled 527 nm Nd:YLF laser (Litron LDY-300PIV) operating at 10 kHz with pulse separation time of ~5 μs. The sheet forming

optics that expand the beam and form a ~1 mm thick sheet consist of three 2.5 cm diameter

mirrors coated for high reflectance at 527 nm, a quarter wave plate, one B-CC-1010-100

plano-concave cylindrical lens for beam divergence and a similar cylindrical lens for

thickness convergence. The laser sheet is aligned at the planes 1, 2 and 3 as shown in Figure

2.13(b). Again, plane 1, 2 and 3 correspond to the bottom jet center, intermediate and top

jet center planes respectively.
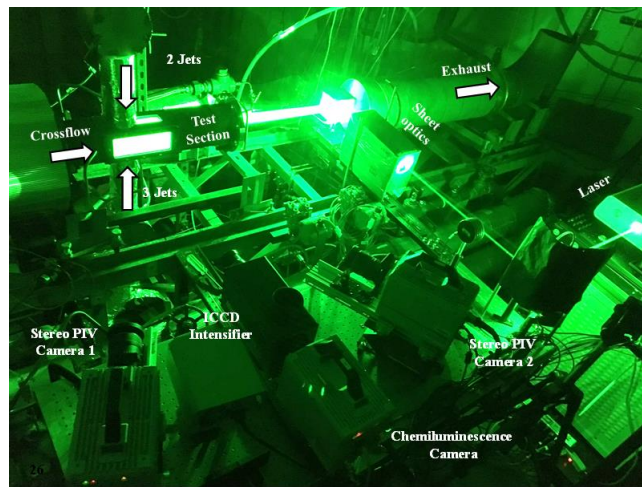
Figure 2.14: 10 kHz optical diagnostics hardware illustrating SPIV and chemiluminescence setup in operation.

The laser sheet is aligned at various planes using a calibration target mount as

shown in Figure 2.15. The calibration mount is attached to the bottom jets with a pin jig to

align itself with the test section. The calibration mount is also equipped with two high

precision rulers to align the calibration plate parallel to the side window at required

distances corresponding to each plane shown in Figure 2.13(b).
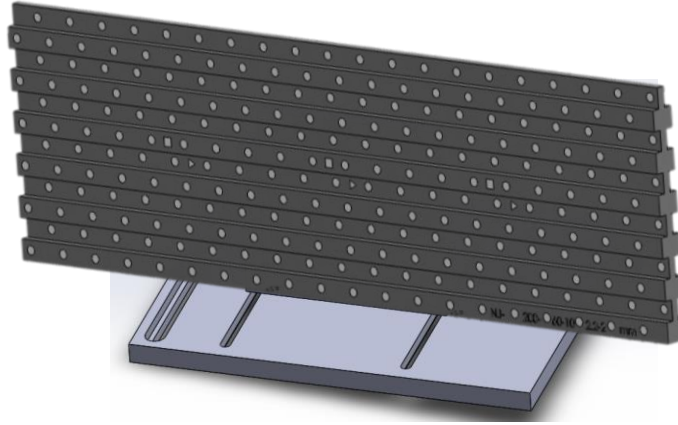
Figure 2.15: Calibration target plate and mount used in SPIV experiments.

The fabrication of calibration included cutting 2 mm deep planes on both sides of a 6 mm thick aluminum plate. The plate is then anodized and the dot pattern is then etched carefully on both the sides using a laser cutter. Standard corrections for perspective and distortion are made using this custom built 3D calibration dot target (200 mm × 60 mm x 6 mm) shown in Figure 2.15. The 2.2 mm diameter dots on each plane on the calibration target are separated by 10 mm (center to center) in horizontal and vertical directions. The distance between the two planes is 2 mm. The jet injection plane (x = 0) is in line with the left triangle etched on the plate.

Particle scattering images obtained using this high speed SPIV setup are used to explore the mixing and velocity fields of CJICF. For velocity field measurements, all the flows (pilot crossflow, bottom jets and top jets) are seeded while for mixing measurements, selective seeding is used to "mark" the fluid from these flows. LaVision Davis 8.2.1 and Davis 8.4 imaging software are used to post-process the particle scattering images where the raw scattering images are calibrated to apply correct physical dimensions Further processing techniques using Davis and MATLAB software are described in Section 2.8.

2.7.2   Flame Chemiluminescence Imaging Setup

2.7.2.1   Low Speed (10 Hz) Visible Chemiluminescence

The diagnostics setup for low speed visible chemiluminescence imaging is shown in Figure 2.16 (a) where a Foculus IEEE1394 black and white camera is used to capture the line-of-sight integrated chemiluminescence signal. The camera is used with a Nikon 55 mm lens and a 2 mm thick BG 28 filter that has the transmittance curve as shown in Figure 2.16 (b). This allows only visible emissions (320-650 nm) to be captured by the camera, hence getting rid of the infrared radiations from the hot surfaces. The software used for chemiluminescence imaging is FOControl 3.0.9.0 and a frame rate of ~7.5-10 Hz with exposure time ~10- 20 ms is used for imaging in most of the experiments. Thus the images obtained with this technique are averaged over this duration. The gain settings for imaging are also adjusted as needed to avoid camera saturation.
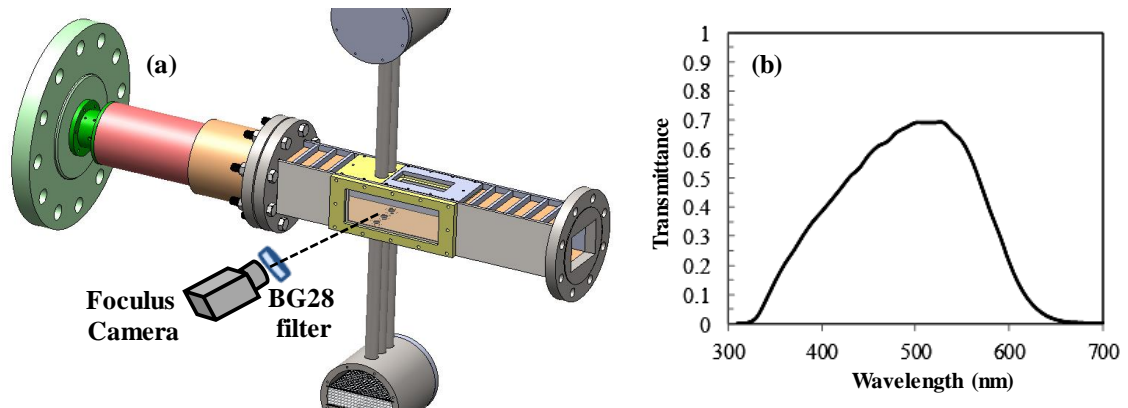
Figure 2.16: (a) Low speed visible spectrum chemiluminescence diagnostics setup. (b) Transmittance curve of BG 28 filter.

The chemiluminescence camera is placed ~ 1.14 m from the test section side window at a slight angle (~5^0) from the normal of the window. The side window (203mm

wide × 76.2 mm tall) aligns flush with the top and bottom walls and the entire window lies in the field of view of the camera. Images acquired using this technique are time stamped and matched with the run conditions stored separately through LabVIEW. Further image processing methods including averaging, detecting edges, plotting contours etc. are described in Section 2.8.

2.7.2.2   High Speed (10 kHz) OH* Chemiluminescence

The high resolution flame imaging employs the high-speed line-of-sight 10 kHz OH* chemiluminescence measurement setup shown in Figure 2.17. This system includes a LaVision Photron SA1 camera optically coupled with an image intensifier (LaVision IRO) and a 45 mm focal length UV lens. A 308 nm UV filter is used in front of the intensified camera to collect the OH* chemiluminescence.
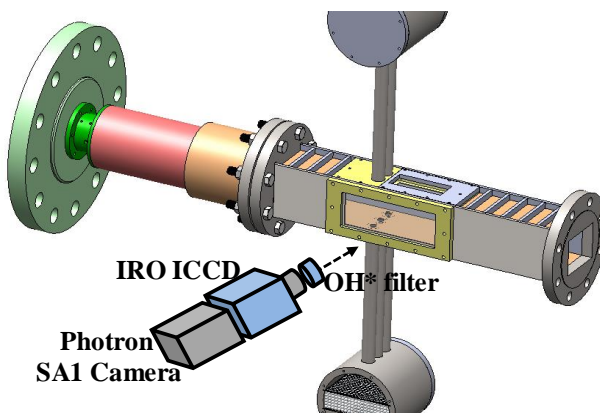
Figure 2.17: 10 kHz high speed OH* chemiluminescence setup.

The gain for the intensifier is varied between 60 and 75% depending on the signal levels for various reacting cases with the goal of obtaining high intensity signal without saturating the camera. Mainly two gate settings (5 µs and 10 µs) are used for the intensifier. The image resolution of 768 × 512 pixels is used to covers the entire optically accessible

test section. For each reacting case, 14,555 images are captured at a 10 kHz frame rate; so the total data acquisition duration is ~1.5 s. For background and calibration images, the IRO gain is set to 47% with gate = 20.02 ms. The images are captured and stored using the Photron FASTCAM Viewer (PFV) software with camera bit resolution and later converted to 16-bit images for further image processing using MATLAB. Section 2.8 describes the Matlab image processing routines used such as cropping, averaging, intensity plotting and edge detecting, and the DaVis routine for transformation to physical coordinates.

2.8   Image Processing and Analysis

2.8.1   Mixing Measurements

For a quantitative comparison of mixing under various jet configurations and J ratios, planar images of elastic laser scattering from the seeded particles are acquired for non-reacting (non-preheated) flow conditions by selectively seeding the jets or the crossflow. Images from one of the two SPIV cameras (Camera 1used here) are first imported into DaVis software along with a corresponding averaged calibration image. After a routine calibration procedure, the images are then de-warped from "raw to world" coordinate system using DaVis. The transformed images are then exported as an .AVI video file which is imported in Matlab for further processing. Firstly, the video file is converted into instantaneous which are cropped to exclude the regions that lie out of the test section boundaries (bottom and top walls).

An example instantaneous image for a parallel jets configuration (2 top jets) at plane 3 (as defined in Figure 2.13 (b)) with J=12 is shown in Figure 2.18(a). The

instantaneous Mie scattering images are analyzed to examine mixing by using two

uniformity metrics U_{rms} and U_{sym} as defined in Equations (2.7) and (2.8).

$$U_{rms} = \frac{\sigma_{strip}}{\mu_{strip}} \tag{2.7}$$

$$U_{sym} = \frac{I_{top} - I_{bottom}}{I_{top} + I_{bottom}} \tag{2.8}$$
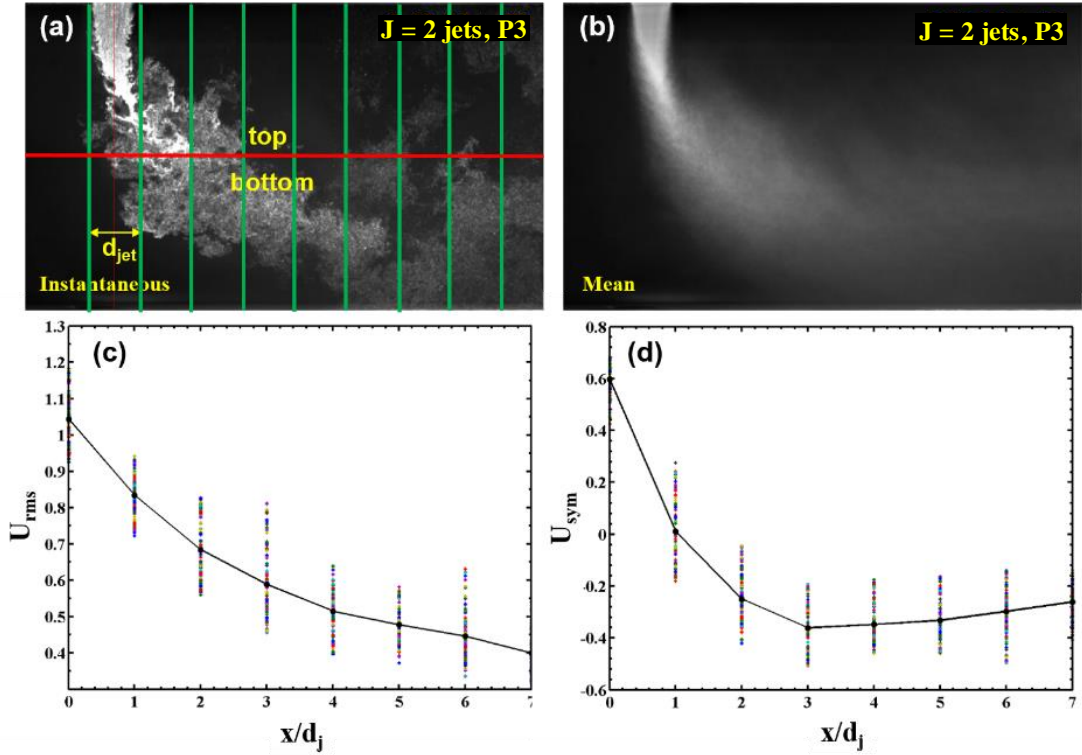
Figure 2.18: Example results for J=12, 2 jets, plane 3. (a) Instantaneous particle scattering image and regions. (b) Mean scattering image. (c) Temporal instantaneous (colored dots) and ensemble average U_{rms} (black dots and line). (d) Temporal instantaneous (colored dots) and ensemble average U_{sym} (black dots and line).

To calculate U_{rms}, an instantaneous particle scattering image is divided into vertical

strips of width equal to one jet diameter (d_j), as shown by the green vertical lines in Figure

2.18(a). The standard deviation normalized by the average intensity within each vertical

strip (or coefficient of variation for a strip) is calculated for 100 instantaneous images to calculate the mean uniformity profile. U_{rms} represents axial (left to right) mixing as the flow moves downstream, and it can range between 0 and ∞, where zero represents completely uniform mixing within a vertical strip.

To calculate U_{sym}, defined in Equation (2.8), each vertical strip is further divided into two regions (top and bottom) with equal areas as shown by the horizontal red line. It represents the symmetry in mixing between the top and bottom halves and is defined for each vertical strip based on their integrated intensities in the top and bottom regions. U_{sym} ranges between -1 and 1; when it equals zero, there is an equal amount of jet fluid in the top and bottom regions of the flow, i.e., a uniform distribution. When U_{sym} is positive, there is more jet fluid present in the top half and a negative U_{sym} value corresponds to more jet fluid being present in the bottom half. Mean scattering images are also calculated in MATLAB from the cropped instantaneous images gathered from the video file for each case. The MATLAB code used for mixing image analysis is attached in APPENDIX B.

2.8.2   Velocity Measurements

A typical processing algorithm used for high speed SPIV datasets using the DaVis 8.4 software is described in this section. For preliminary velocity calculations performed using low speed planar PIV setup, a similar but simpler processing routine is used while using image processing parameters as described previously in Section 2.7.1.1. As mentioned in Section 2.7.1, the main difference between acquiring velocity data and mixing data is that all the three flows (pilot, bottom jets and top jets) are seeded for velocity measurements while mixing measurements require selective seeding of only one or two of

these flows. The seeding levels in the velocity measurements are set manually for the individual flows by looking for equal scattering intensity in the downstream exhaust.

To begin, the scattering images are captured and stored separately for both cameras in the camera's native (12 bit) resolution in their respective destination folders using PFV. Each case is then reopened in PFV using the respective .cih files and converted and resaved into 16 bit resolution images (.tiff files). The reason for doing so it that the PFV software has an anomaly where if the images are stored directly as 16 bit files, PFV misses a large band of signal intensities, this was learnt through trial and error and by plotting the histograms of images stored using each method. A .bat code presented in APPENDIX C is used to create multipage (4 page) .tiff files that arrange the two image pairs from each of the two SPIV cameras for easier and faster import into DaVis software, where the rest of the velocity vector processing is performed.

For velocity vector processing, a project folder in DaVis is created for the datasets collected in each laser sheet plane and corresponding averaged background images are imported for each camera. The multipage .tiff files for each case in that plane is then imported from the respective folders along with the correctly assigned camera attributes (such as the time between frames, Δt between laser pulses etc.). A routine calibration procedure is then followed to align the two camera views with the physical coordinates defined using the custom built calibration plate. For SPIV analysis, an extensive self-calibration procedure is used for each dataset to get an accurate spatial alignment of the two cameras. The self-calibration procedure is repeated several times while using inbuilt functions such as "subtract sliding background" and "additionally correct remaining disparities" until the computed average disparities and computed remaining disparities are

low (~ 0.1 mm). The scale factors obtained for the SPIV data presented in this thesis are 5.477 pixel/ mm for plane 1 and 5.4377 pixel/mm for plane 2.

After self-calibration, the next step is to compute velocity vectors with the inbuilt PIV routine from DaVis. For the data obtained in the SPIV experiments reported in this thesis, the image pre-processing option in DaVis is not used due to the high quality of the raw data. A geometric mask slightly larger than the laser illuminated region is selected to obtain vectors as close as possible to the walls. Velocity vectors are calculated with the stereo cross-correlation mode using the multi-pass processing and adaptive interrogation windows options. A total of four passes are used, where the first two passes employ a 64×64 square shaped interrogation windows with 50% overlap, and the second two passes use 12×12 auto-adjustable windows with 50% overlap; the high accuracy option is selected for the final pass. This results in the final vector spacing of 6 pixels or 1.1 mm which essentially means that 11-12 vectors are determined within a single jet diameter.

For vector post-processing, allowable velocity vector magnitudes of 150 m/s (V_x), 300 m/s (V_y), and 150 m/s (V_z) are used for the high air split cases. Two passes of a median filter with the "strongly remove and iteratively replace" option are used to remove outliers if the difference from the average is $>2\sigma$ of neighbours and reinserted if the difference from the average is $<3\sigma$ of neighbours. These parameters (2, 3) are used for the air split $= 1.3$ datasets in plane 1 and parameters (1.5, 0) are used for the remaining datasets. Groups containing less than 5 vectors are also removed in post-processing, and a default basic smooth filter in a 3×3 neighbourhood is used. The missing vectors in the instantaneous

images are not filled since the data quality was good and since over 15,000 images are used, meaningful statistics are obtained without interpolations or extrapolations.
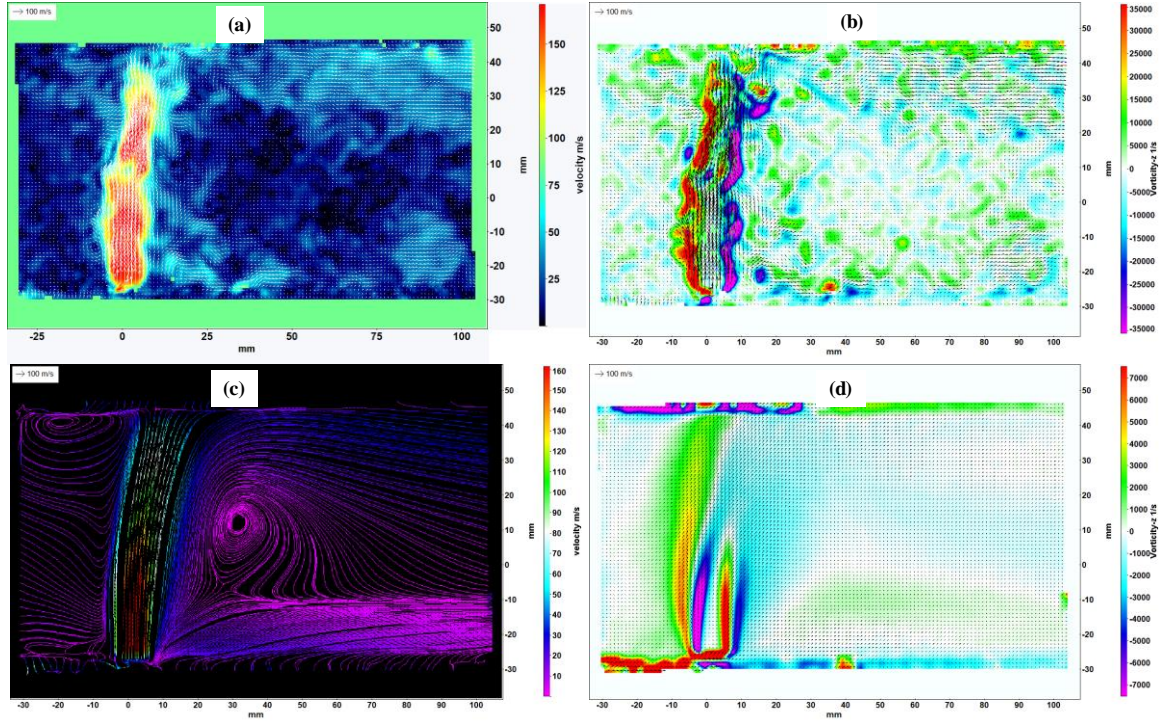
Figure 2.19: Examples of calculated vector fields for staggered jets with split = 1.3 in plane 1 (a) Instantaneous velocity. (b) Instantaneous vorticity. (c) Mean velocity. (d) Mean vorticity.

Average velocity vector fields along with velocity uncertainties and vorticity fields are calculated in DaVis using an effective number of samples requiring a minimum of 10 vectors to be present at a location for computed results and only average velocities within 5σ are included. Example results obtained for instantaneous and mean velocity and vorticity fields are presented in Figure 2.19.

2.8.3   Flame Measurements

The line-of-sight chemiluminescence techniques described in Section 2.7.2 are used to obtain flame images for RQL and LQL conditions. For low speed visible spectrum chemiluminescence data, simple averaging and edge detection methods are used in MATLAB. The image processing techniques and methods used for high speed images are described in this section. The data collection process including storage and conversion from camera bit (12 bit) image resolution to 16 bit for the 10kHz chemiluminescence measurements (in the same matter and for the same reason described in Section 2.8.2). After converting the data sets into 16 bit .tiff format, the images are imported in MATLAB, and the images are cropped such that the region outside of the test section optical window is removed in order to minimize the computation time by processing only the data in the region of interest.

The saturated instantaneous images are converted from 16 bit integers to double precision format before any calculations to increase precision. The output results from the processed data are converted back to 16 bit integer formats for display and plotting. The average images are calculated from 14,552 instantaneous images for each data set presented in the high speed RQL and LQL chemiluminescence studies. This implies that the mean statistics are reported for ~1.5 seconds, thus providing a fair estimate of the steady state results as shown in the Figure 2.20 (b). The intensity magnitudes are adjusted for the changes in gain and gate settings of the intensified camera using results from a calibration experiment where intensities from a constant flame source (a MAP blow torch) are recorded while varying the gate and gain settings of the same intensified camera setup used in the RQL and LQL experiments.
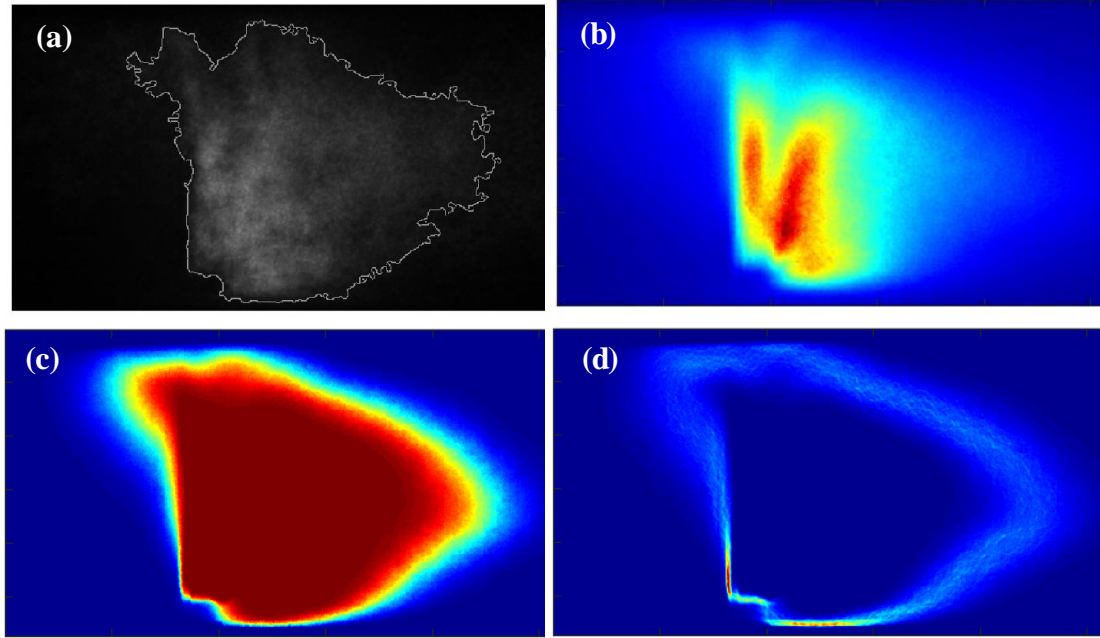
Figure 2.20: Example 10 kHz OH* chemiluminescence results. (a) Instantaneous image with edge. (b) Mean image. (c) PDF image. (d) Mean edges.

To detect the flame extent or heat release region edges, binary instantaneous images are calculated using a threshold that is 0.5 times the threshold determined by Otsu's method [70]. It was observed that the Otsu's method generated a high threshold for the images obtained in these experiments. The multiplication factor (0.5) was determined through trial and error by manually confirming that the image region with luminosity was approximately included within the detected edge boundaries as illustrated in Figure 2.20 (a). From the binary instantaneous images, an average is calculated which corresponds to the mean probability density function (PDF) image indicating the regions where flame is present most of the times as shown in Figure 2.20 (c). The instantaneous edges are also averaged to illustrate the flame brush and intermittency of flame extent as shown in Figure 2.20 (d). Further the mean intensity images are filtered using Gaussian filter for two standard

deviation filtering and intensity contour maps are drawn. The MATLAB code used for flame image processing is presented in APPENDIX D.

2.9 Experiment Design and Flow Conditions

The test facility is used in reacting and non-reacting modes of operation in order to experimentally investigate the flame characteristics, mixing and velocity field of staged combustors that involve staggered-opposed and parallel CJICF configurations. The experiments are designed around these two jet configurations and other main parameters that are varied are: 1) pilot and jets equivalence ratios which governs the adiabatic flame temperatures which in turn governs the reaction time scales, 2) air split ratios which govern the J ratios for a given geometry or the jet configurations and which also govern the confinement conditions inside the combustor and thereby governing the flow or residence time scales. A summary of the overall range of nominal flow conditions that are used to run the test facility are tabulated in Table 2.1.

Table 2.1: Overall range of nominal flow conditions.

	Pilot	Jets
Φ	0, 0.6, 0.8-1.3	0, 0.3, 0.6, 0.8
$T_{preheat}$ (K)	500-600	450-550
Velocity (m/s)	5-35	48-270
$T_{adiabatic}$ (K)	1851-2230	1184-1851
Reynold's #	1313-7696	49000-12200
Air split	0.4-2	
J-ratio	12,30, 75-250	

For flame analysis, the reacting conditions are attained by fueling either just the pilot flow to study RQL scenario, or by fueling both the pilot and jets to study the LQL

scenario. Both fueling configurations require the preheated air supply for the pilot and the jets. The equivalence ratios for each flow are the main parameters that are controlled here while the air split is fixed at 1.3 for most cases. A few cases with a different air split (0.78) are used to relate the flame properties between staggered and parallel jet configurations to explore if the J ratio plays an important role in such confined flows. The low speed and high speed chemiluminescence experiments described in Section 2.7.2 are used to answer questions related to the flame characteristics of staged combustors. Nominal flow conditions for the chemiluminescence or flame experiments are presented in Table 2.2.

Table 2.2: High and low speed chemiluminescence cases and nominal conditions.

High speed OH* chemiluminescence								
		Name	Split	ϕ_p	ϕ_{bj}	ϕ_{tj}	# Jets	J
RQL	Staggered	130800005	1.3	0.8	0	0	5	64
		138500005	1.3	0.85	0	0	5	62
		131300005	1.3	1.3	0	0	5	62
		131700005	1.3	1.7	0	0	5	75
	Parallel	138500003	1.3	0.85	0	0	3	173
		131300003	1.3	1.3	0	0	3	173
		781300003	0.78	1.3	0	0	3	62
LQL	Staggered	130603035	1.3	0.6	0.3	0.3	5	75
		130608085	1.3	0.6	0.8	0.8	5	75
		138503035	1.3	0.85	0.3	0.3	5	62
		138508085	1.3	0.85	0.8	0.8	5	62
		138508035	1.3	0.85	0.8	0.3	5	62
		138508005	1.3	0.85	0.8	0	5	62
	Parallel	138508083	1.3	0.85	0.8	0	3	173
		138508003	0.78	0.85	0.8	0	3	62
Low speed OH* chemiluminescence								
		Name	Split	ϕ_p	ϕ_{bj}	ϕ_{tj}	# Jets	J
RQL	Staggered	131100005	1.3	1.1	0	0	5	59
		131200005	1.3	1.2	0	0	5	60
		131300005	1.3	1.3	0	0	5	62
		131400005	1.3	1.4	0	0	5	65
		218600005	2.1	0.86	0	0	5	161
		211000005	2.1	1	0	0	5	155
		211200005	2.1	1.2	0	0	5	157

For flow field analysis, the test facility primarily runs in a non-reacting mode of operation since the particle scattering based diagnostics techniques are adversely effected by the presence of reacting flows. One of the biggest challenges in this facility is to send in a laser sheet from the exhaust end of the test section; this is extremely difficult if hot exhaust gases are present. Mounting a cooled mirror in the exhaust is challenging in itself but a bigger challenge would be the steering and misalignment of the illuminating laser beam (or sheet) as it travels through a turbulent reacting flow medium with a non-uniform refractive index. However, a preliminary low speed PIV study comparing non-reacting and reacting flow fields is performed by sending a laser sheet from the top illuminating a smaller region of the test section. As the results suggested that the flow features of highly confined jets in crossflow are not drastically different in the presence of reacting environment, advance high speed SPIV experiments were designed for non-reacting operation mode of the test facility.

Table 2.3: Nominal flow conditions used in non-reacting mixing and velocity field experiments.

High speed SPIV Velocity			
Air Split	5 Staggered	3 Parallel	2 Parallel
1.3	252 (1,2)	701 (1,2)	1578 (1,2)
0.71	75 (1,2)		
0.43		75 (1,2)	
0.28	12 (2)		75 (1,2)

High speed SPIV Mixing			
Air Split	5 Staggered	3 Parallel	2 Parallel
1.3	252 (1,2)		
0.71	75 (1,2)		
0.45	30 (1,2,3)		
0.28	12 (1,2,3)		75 (1,2,3)
0.18			30 (1,2,3)
0.11			12 (1,2,3)

In the flow field analysis, the primary focus is laid on elucidating the mixing and velocity fields in CJICF. The same optical diagnostics setup as described in Section 2.7.1 is used for these studies, with the difference being that of the seeding technique as discussed earlier. The experiments are designed to explore the flow fields of staggered and parallel jet configurations while the air splits and J ratios relevant to the reacting flame conditions are studied. The flow conditions for velocity and mixing field studies are summarized in Table 2.3

2.10 Autoignition Time Scale Modelling Approach

In addition to the experimental investigations, chemical time scale modelling is also employed in this thesis. Autoignition times are calculated using a plug flow reactor (PFR) model in the Chemkin Pro simulation software as shown in Figure 2.21. It should be noted that autoignition is hard to define here as the vitiated products are at very high temperature and the typical high activation energy autoignition behaviour is not observed, instead the reactions occur almost instantaneously.
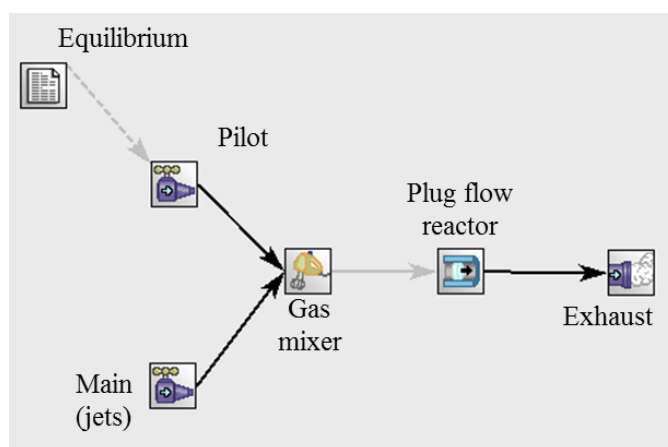
Figure 2.21: Plug flow reactor (PFR) setup in Chemkin Pro used for autoignition timescale modelling.

First, the equilibrium composition and temperature are calculated for a given pilot fuel-air mixture using an adiabatic, constant-pressure and constant-enthalpy equilibrium model. The pilot inlet composition uses the final product composition from the equilibrium calculator as the initialization data set. For the pilot inlet temperature, the adiabatic flame temperature is used to simulate an adiabatic flow from the pilot combustor. However a real laboratory experiment will include pilot flow heat losses, for example due to cooling flow around the combustor walls; additional pilot temperatures of 1400, 1500, 1600 and 1700 K are used to estimate the variation of autoignition time scale with heat losses in the pilot flow. The final product composition equilibrium calculator and varying temperatures constitute the pilot flow, which is mixed with the dilution air from the jets in an instantaneous, adiabatic, non-reacting gas mixer.

The plug flow reactor (PFR) code solves the 1-D energy and momentum equations. San Diego chemical mechanism is used for the CH_4 - air chemistry [71]. The starting axial position for the PFR is zero cm and the ending axial position is varied for each case to best resolve the data points near the ignition process while achieving almost complete combustion marked by the product temperature approaching its maximum value. Finally the products from the PFR are passed to the exhaust model which records the output conditions.
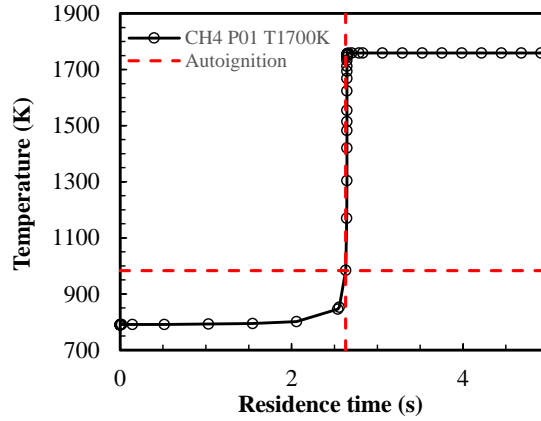
Figure 2.22: Example of autoignition time calculated at 20% ΔT rise for T_{pilot} = 1700 K, $\dot{m}_{jet}/\dot{m}_{pilot}$ = 3.

After completing the parametric study for different fuel-air mixtures, pilot temperatures and pilot-jet mixedness, the output data is analyzed in MATLAB to calculate the autoignition times based on temperature rise and peaks of H and HCO radicals. The most reliable, consistent and physically meaningful definition of autoignition time is found to be the one based on temperature profile across the PFR. In this study, autoignition time is defined as residence time in the PFR where temperature rise is 20% of ΔT ($T_{final} - T_{initial}$) as shown in Figure 2.22. The MATLAB code used to calculate and plot autoignition times is attached in APPENDIX E.

CHAPTER 3.   FLOWFIELD OF CJICF

The flowfields for confined jets in crossflow (CJICF) are examined in this chapter for two types of jet configurations: parallel (unopposed) jets and staggered-opposed jets (also denoted simply as staggered in the following). The low-speed planar and high-speed (10 kHz) stereo PIV setups described in Chapter 2 are used to obtain particle scattering images to explore mixing and calculate velocity fields of CJICF for conditions relevant to the RQL and LQL flame studies presented in Chapters 4 and 5.

Firstly in Section 3.1, the mixing field is analyzed for non-reacting CJICF for the two configurations for a range of air split (0.28–0.71) and J (12–75) ratios to elucidate the jet-crossflow, jet-jet and jet-wall interactions and their effects on mixing and uniformity of the flow. Secondly in 3.2, preliminary planar PIV results are presented to compare the reacting and non-reacting CJICF flowfields. Thirdly in Section 3.3, the velocity field results from non-reacting, high-speed SPIV technique are presented for the two configurations for fixed air split and for fixed J values.

3.1   Mixing Field

This section presents the results from mixing analysis performed using high speed (10 kHz) planar imaging of particle scattering with non-reacting, room temperature jets. As shown in Table 3.1, two jet configurations: parallel (using 2 top jets) and staggered-opposed (using all 5 jets, i.e., the configuration used in most of the reacting experiments) are compared at low to high J ratios to elucidate the effects of jet configuration and momentum ratio on mixing. The two uniformity metrics, U_{rms} and U_{sym} as defined in

Equation (2.7) and Equation (2.8), are used to quantitatively compare the mixing behavior of each jet configuration. Results are presented for three planes as defined in Figure 2.13 (b), where plane 1 passes through the centerline of the middle bottom jet, plane 2 is the intermediate plane between the bottom and top jet; and plane 3 is at the center of the top jet farthest from the optical access window.

Table 3.1: Nominal conditions for mixing analysis experiments.

Jet configurations	J ratios	Planes
Parallel (2 jets)	12, 30, 75	1, 2, 3
Staggered-opposed (5 jets)	12, 30, 75	1, 2, 3

First, we examine the U_{sym} metric for parallel jets, as indicated by dashed lines in Figure 3.1 (a, b, c). Generally, across all three planes, the flow becomes more uniform (top to bottom) moving downstream, as seen by the decrease in U_{sym} with increasing x/d_j. Planes 1 (Figure 3.1 (a)) and 2 (Figure 3.1 (c)) are outside the initial jet region for the parallel injection configuration. In these planes, the jet fluid for each J condition is entrained by the crossflow and is dispersed almost evenly across the length and the height of the test section as shown by nearly zero U_{sym} values.

In plane 3 for the parallel configuration, which is the center plane for one of the injected jets, the least amount of top-bottom uniformity might be expected. This is evident in Figure 3.1 (c). The results suggest that for the low J case ($J = 12$), the jet turns rapidly and mostly stays near the bottom half of the test section height, as indicated by the U_{sym} value going from positive to negative after ~ 1 jet diameter downstream of the injection location. For the parallel jets with medium J (30), the jet fluid penetrates towards the

bottom wall before turning since U_{sym} is nearly zero at the injection location, and then stays

partly in the bottom half of the test section as the flow progresses downstream.
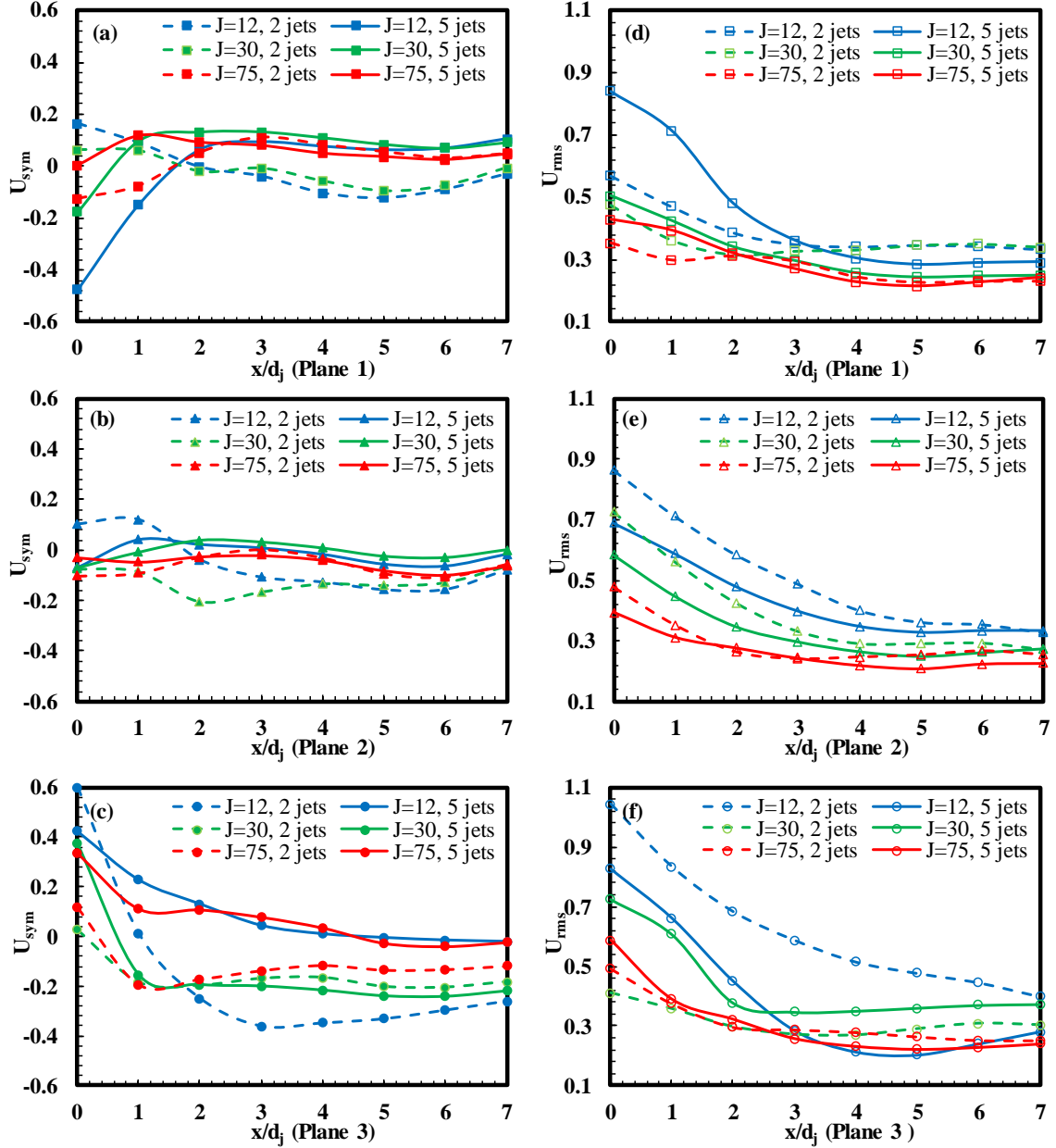
Figure 3.1: Uniformity numbers for planes 1 (a and d), 2 (b and e), and 3 (c and f) for J = 12, 30, 75 with two jets (parallel) and five jets (staggered).

For the parallel jets with high J (75), the jets impinges strongly on the opposite wall

as evidenced by $U_{sym} \sim 0$ at the injection location. For high J, a larger amount of jet fluid is

dispersed in the upper portion of the test section as indicated by the lesser negative U_{sym} values when compared to the lower J (12, 30) cases, suggesting rapid mixing due to higher amount of jet-wall interaction at higher J. These effects of J ratio on jet trajectories are also illustrated in the mean scattering images shown in Figure 3.2 for plane 3.

For the staggered-opposed configuration, the results for U_{sym} in plane 3 (Figure 3.1 (c)), now passing through the center of a top jet, indicate that the low J (12) and high J (75) cases provide better top-bottom uniformity in the downstream regions when compared to the medium J (30) case. For low J, the jets turn well before reaching the opposite wall, and interact with the opposed jets, likely breaking up and mixing along with the crossflow fluid. For high J, rapid mixing also occurs, though now likely due to the impingement on the opposite walls, which helps in redirecting the vertical momentum into the crossflow's axial direction. The U_{sym} metric in plane 1 (Figure 3.1 (a)) suggests that for high J, better top-bottom mixing occurs closer to the jet injection possibly due to the wall impingement as well as due to interaction of the opposed jets. Jet fluid in all the cases reaches plane 2 through transport of jet fluid from lateral jet fluctuation, as illustrated in Figure 3.3. The trends for U_{sym} in plane 1 of the 5 jets configuration are similar to that of plane 3, since both the planes are at the center of a jet sandwiched between two jets from the opposite wall and hence represent a similar flow field. Across the three planes, the staggered five jets with highest J provide the best top-bottom uniformity going downstream in the test section. This is consistent with the average particle scattering images shown in Figure 3.2.
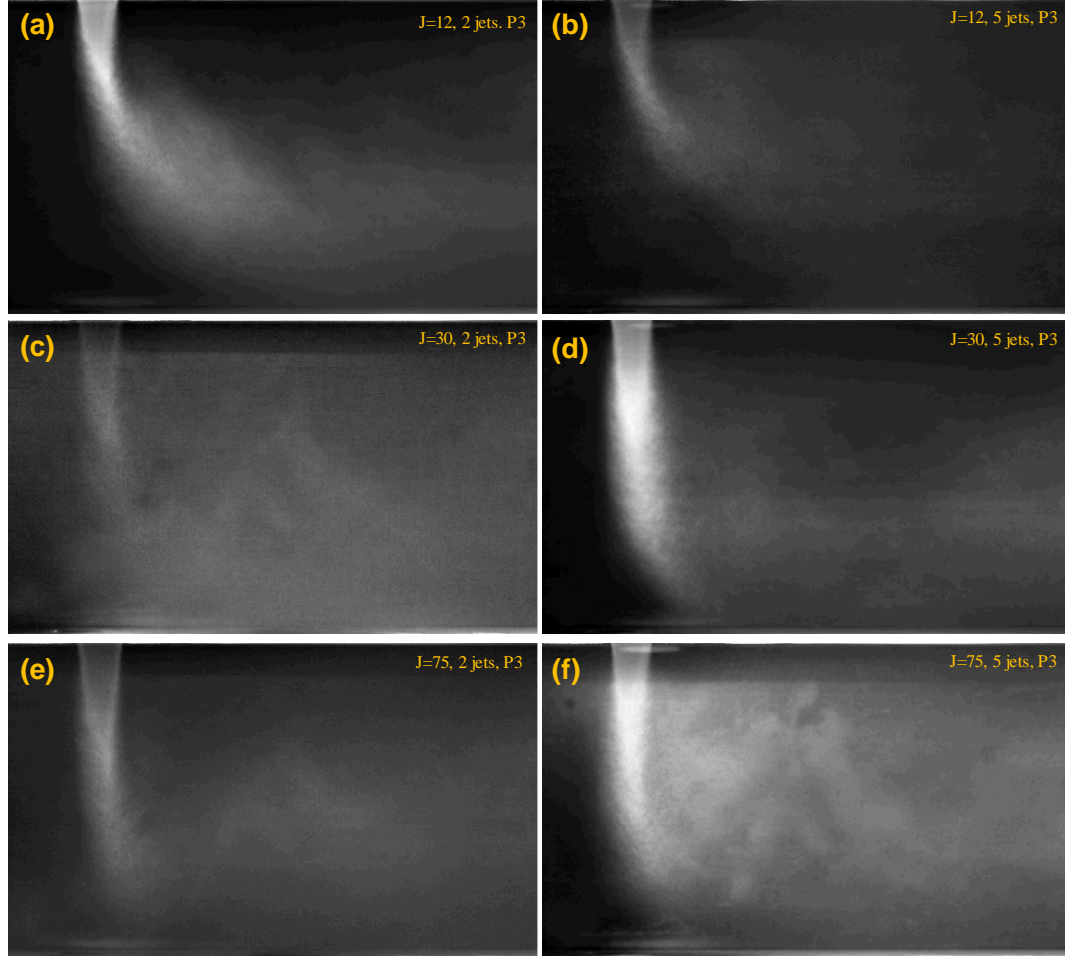
Figure 3.2: Average particle scattering images illustrating the effects of jet configuration (left vs. right) and *J* ratio (top vs. bottom) on jet trajectories and mixing.

Overall, in Figure 3.1 (d, e, f), decreasing U_{rms} values with downstream distance suggest improved mixing of jet fluid with the crossflow. Again, the staggered configuration for planes 1 and 3 show similar trends for the reasons discussed above. Consistent with the U_{sym} results, the U_{rms} values also show better mixing is achieved with downstream distance as the jet momentum is increased. Again this is possibly due to stronger jet-jet and jet-wall interactions at higher *J* values. Thus one might conclude that increasing the *J* of the jets will always tend to enhance mixing, though with diminishing results. Across different planes, U_{rms} is a better representative of the uniformity variation. As depicted in Figure 3.1

71

(d, e, f), the U_{rms} values towards the end of the test section are closely matched between the different planes, suggesting that the jet fluid is well dispersed in the lateral direction and nearly uniformly mixed with the crossflow across the different planes.
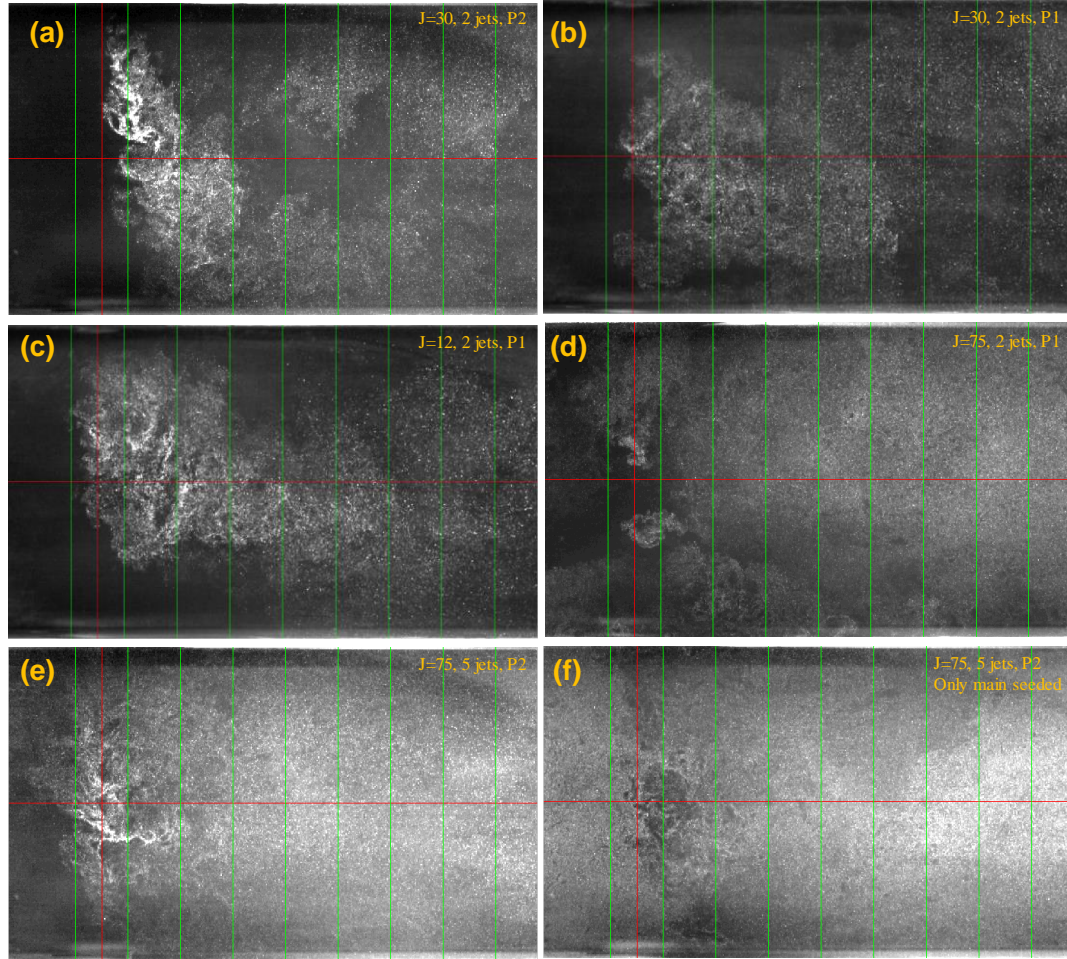
Figure 3.3: Instantaneous images of particle scattering for planes between jets in the parallel configuration (a-d) and staggered-opposed configuration (e, f) showing lateral jet penetration.

The lateral movement of the jet fluid is illustrated through instantaneous particle scattering images from the off-center planes for the parallel and staggered jet configurations (see Figure 3.3) for the three J values. These results are consistent with the U_{rms} plots shown in Figure 3.1. For example for J = 30, the one-sided parallel jets

72

configuration, Figure 3.3 (a,b) shows the dispersion of jet fluid in planes 2 and 3 that mixes with the crossflow and becomes fairly uniform downstream. Comparing the parallel jets configuration for low J (12) and high J (75) in Figure 3.3 (c, d), the high J case attains faster mixing into plane 1 due to wall interactions. Two results are shown for the high J (75) case in the opposed-staggered configuration at plane 2; Figure 3.3 (e)) shows a result with the jets seeded, while Figure 3.3 (f) presents a result when the seeding is reversed, i.e., the crossflow rather than the jets is seeded. In these cases, the similarity in the downstream regions of the particle scattering images shows that the crossflow and jet fluid are well mixed.

The high J (30, 75), staggered jets configuration corresponds most closely to the reacting cases presented in the RQL (Chapter 4) and LQL (Chapter 5) studies. Therefore, it is useful to summarize an important finding for mixing in these cases. Throughout the transverse direction in the test section, both uniformity metrics presented in Figure 3.1 reveal the flow is nearly uniform within a short distance downstream of the jet injection location ($\sim 4 - 6d_j$). This result will be important to understanding the extent of the combustion zone for the reacting CJICF flows.

3.2   Mean Velocity Field of Non-Reacting and Reacting Staggered CJICF

Initial velocity measurements were obtained for the staggered CJICF configuration using a low speed (15 Hz) planar PIV setup, as described in Section 2.7.1.1. Given the limited optical access limitations under reacting conditions, but the ability to make much higher quality cold flow measurements, the goal of these experiments was to determine the similarity between the non-reacting and reacting flowfields.

73
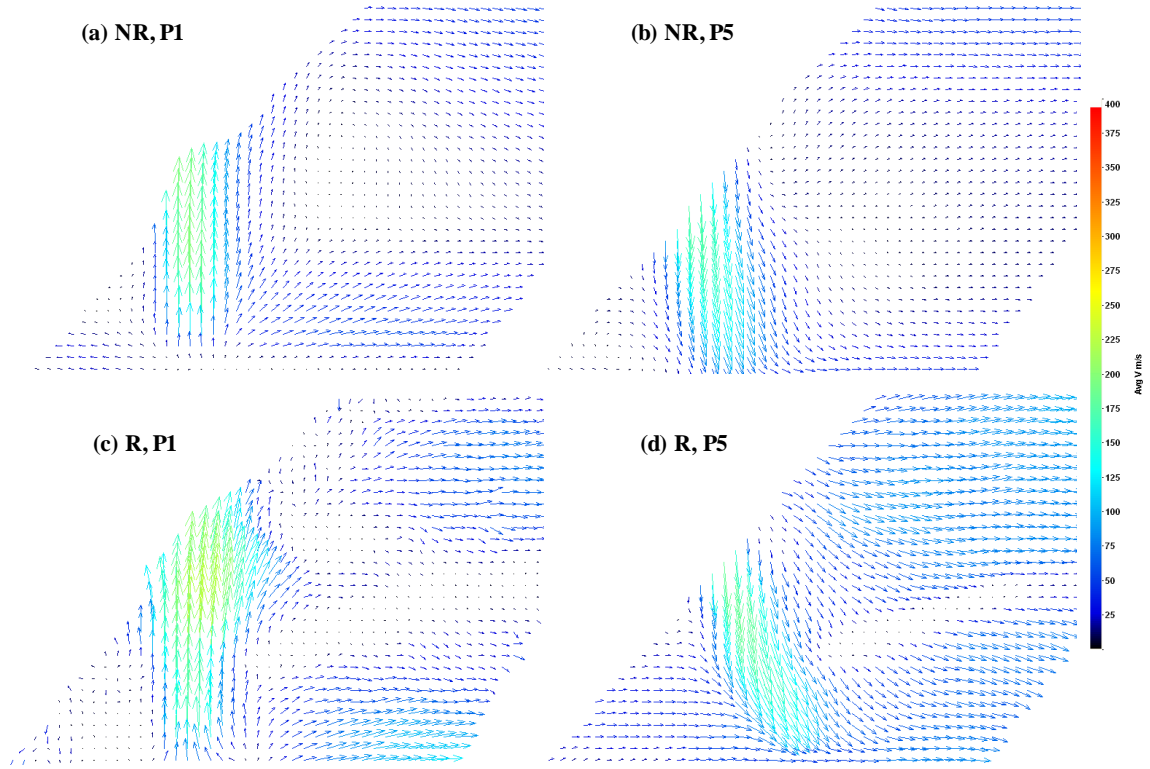
Figure 3.4: Mean velocity field of staggered CJICF using low speed PIV at split = 1.3. (a) Plane 1, non-reacting. (b) Plane 5, non-reacting. (c) Plane 1, reacting ϕ_p = 1.3. (d) Plane 5, reacting ϕ_p = 1.3.

Mean velocity fields are presented in Figure 3.4 for both non-reacting (preheated air but unfueled pilot combustor) and reacting conditions. As described in Chapter 2, the PIV laser sheets entered the test section from the top window at an oblique angle. Thus, the laser illuminates a trapezoidal region in the test section, as illustrated in Figure 2.12 (a). The results in Figure 3.4 clearly illustrate a major drawback for obtaining high quality velocimetry data in this arrangement; the inability to capture the full vertical extent of the jet flow. In plane 1 (defined in Figure 2.12 (b) and shown in Figure 3.4 (a) and (c)), the middle bottom jet can be visualized starting from the jet exit to a height just beyond the middle of the test section. To capture the remaining portion of the jet, plane 5 (defined in Figure 2.12 (b) and shown in Figure 3.4 (b) and (d)) is used. Assuming the middle bottom

and the top jets are symmetric on average, they collectively represent the flow features of a jet that is interlaced between two opposing jets.

It should be noted that the PIV diagnostics is adversely effected by the reacting flows due to reduced seed density and increased background reflections from the seed particles adhering to the window. As a result, only ~25-30 instantaneous images for the reacting case (and 500 images for the non-reacting case) were used to compute the mean velocity fields shown in Figure 3.4 (c, d). Hence, these results provide only a preliminary understanding of the flow field.

Generally, non-reacting conditions (bottom images) produce a similar (average) flowfield to the reacting case (upper images) in both measurement planes. The jet widths are similar, and the jets penetrate nearly vertically, impacting the opposed wall with most of their vertical momentum intact, as seen in the far field of the downward moving top jets shown in Figure 3.4 (b) and (d). Beyond ~$4d_j$, the reacting jet turns downstream more than the non-reacting jet, but the deflection is still small (less than ~30°). As the mass flow ratio is roughly the same in both reacting and non-reacting cases, the difference in deflection could be attributable to the momentum flux ratio. In other words, the value of ρu for the crossflow is nearly unchanged with the addition of fuel in the reacting case, so it is likely that the increase in U_∞ due to combustion in the pilot burner leads to the increase in $(\rho U^2)_\infty$ or decrease in J which causes larger deflection for the reacting jet. The increased momentum flux of the cross-flow may also cause the difference seen in the near-field, specifically the leeward side of the reacting jet expanding farther downstream (image (c)),

though this could also be due to the low number of images used to produce the average reacting average flowfield.

These results establish that many of the essential flow features of the CJICF are similar in reacting and non-reacting environments. Thus further analysis of CJICF velocity fields is performed using a high resolution setup under non-reacting conditions, which allow a laser sheet to enter from the exhaust end with the use of a protective mirror box, thus illuminating the entire height of the test section and providing a much larger field of view.

3.3   Velocity Field of Staggered and Parallel CJICF

The velocity field results for non-reacting staggered (5 jets) and parallel (2 or 3 jets) CJICF configurations using the high speed (10 kHz) SPIV setup described in Section 2.7.1.2 are presented here. Results are shown for two image planes (see nomenclature from Figure 2.13 (b)). Plane 1, shown in the left images of the groups of figures presented in this section, is the center plane of the middle bottom jet, while plane 2, shown in the right images, is the center plane of the top jet farthest from the test section window. This arrangement of images within the figures is used consistently in this section unless otherwise indicated.

Note that plane 1 contains passes through the center of a jet exit in the staggered (5 jets) and 3-jet parallel configurations, but for the 2-jet parallel case, plane 1 lies midway between the centers of the two jet exits, so it does not contain an initial jet region. Plane 2 can be described as an intermediate plane for the staggered (5 jets) configuration, where it lies between the closely spaced edges of the interlacing bottom and top jet exits. For the

parallel (2 and 3 jets) configuration, it is best to describe plane 2 as passing along the edge of a jet injection hole. In the figures presented below, x = 0 is at the center of the jet injection plane in the axial direction, while y = 0 represents a height 30 mm above the bottom of the test section; the vertical zero location is based (arbitrarily) on a reference point chosen on the calibration target plate shown in Figure 2.15.

3.3.1   *Constant Air Split (1.3) CJICF Configurations*

Results for the mean velocity fields are shown in Figure 3.5 for a fixed air split of 1.3. The vertical velocity component (V_y) is indicated by the color; the total velocity profiles using vectors are overlaid on top of the color maps at specific heights in the test section to visualize primarily the jet characteristics such as the penetration depth and jet width. As indicated in the low resolution preliminary PIV results presented in Section 3.2, the jets penetrate across the entire test section height to the opposite walls. This is best seen in Figure 3.5 (a, c) in the results for plane 1, which cuts through a jet center for both the staggered and 3-jet parallel cases. The jet widths are also seen clearly in Figure 3.5 (a, c) for these two configurations. Again consistent with the preliminary findings, the jet widths remain fairly constant. More specifically, the width of the jets increase by only ~50% in going from a distance just above the initial (bottom) wall and the location where they nearly impact the opposite (upper) wall. It is interesting to note that the jet is also wider for the 5 staggered jets than the 3 parallel jets when comparing Figure 3.5 (a, c).
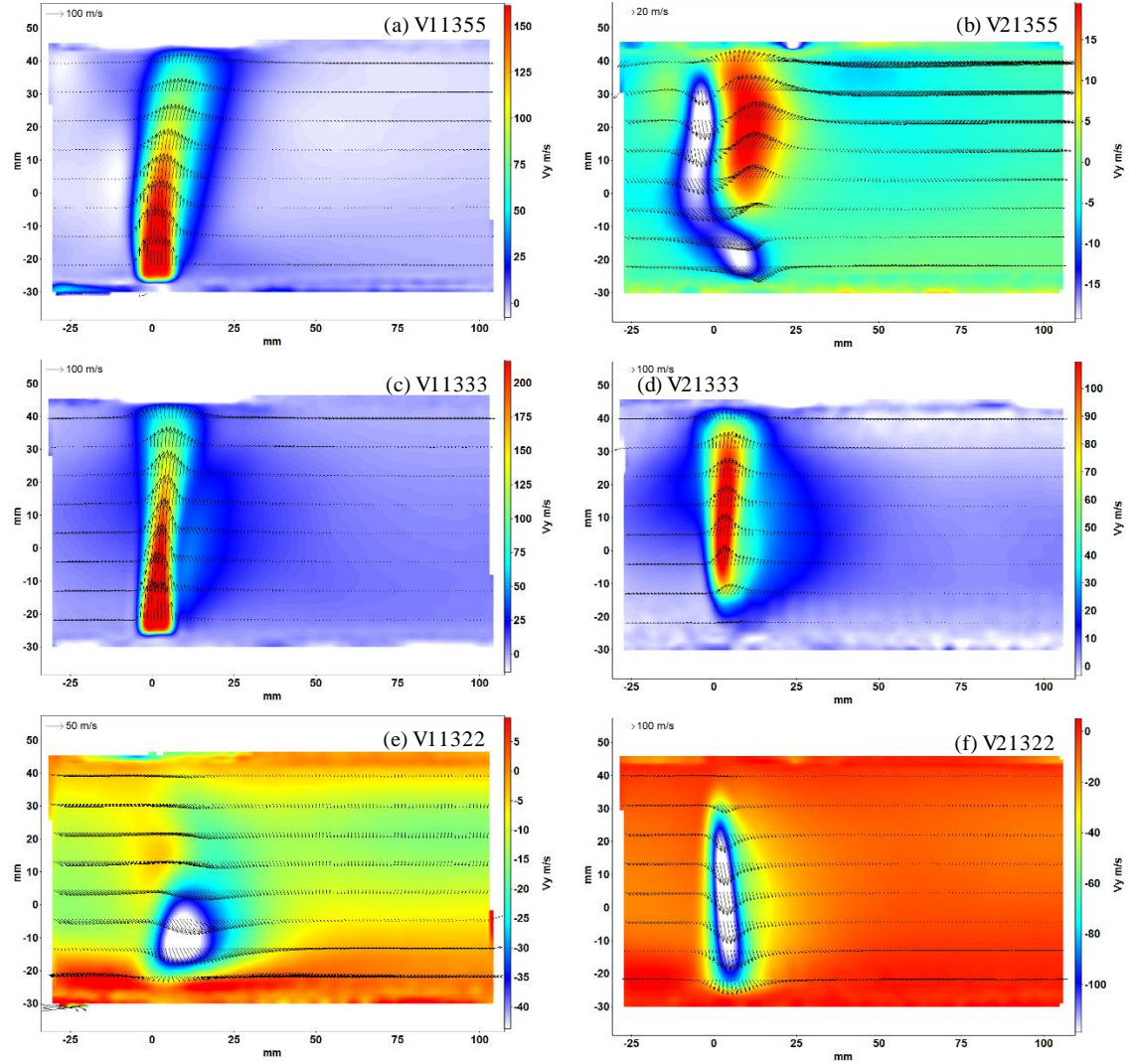
Figure 3.5: Mean V_y field (color) of CJICF (*Split* = 1.3) and velocity vectors at different heights for plane 1 (left) and plane 2 (right). (a, b) 5 staggered jets, $J = 252$. (c, d) 3 parallel jets, $J = 701$. (e, f) 2 parallel jets, $J = 1578$. Note the different color map scaling for each result.

The velocity results shown in Figure 3.5 (d, f) for the parallel (single-sided) configurations reveal the presence of jet fluid in the edge plane (2) and again show jet penetration to the far wall. The results in Figure 3.5 (e) show the influence of confinement on single-sided jets. The white region with downward velocity in that figure suggests that jet fluid (or possibly "entrained" cross-flow fluid) for the two (downward) parallel jets laterally spreads into plane 1 in the bottom third of the test section, i.e., nearer the opposite

wall. This may be surprising since plane 1 is midway between the two jet centers and is ~0.5d_j away from the closest edges of the jets.

Finally, the intermediate plane (at the edge of both upward and downward jets) for the staggered-opposed configuration shown in Figure 3.5 (b) reveals a more complex flowfield. Both downward (white region) and upward (red/yellow region) moving jets are present; this flow field is clarified through the following streamline analysis.

The two-dimensional streamlines based on the average velocity field, along with the mean velocity magnitudes for all three jet configurations are shown in Figure 3.6. Keep in mind that what appears to be the streamline sinks/sources in Figure 3.6 are likely an artifact of presenting an unsteady three-dimensional flow field using averaged two-dimensional streamlines where the fluid laterally moves to/from the other planes.

First, the staggered-opposed CJICF configuration shown in Figure 3.6 (a, b) is analyzed. This configuration is the most relevant case for understanding the RQL and LQL studies described in Chapters 4 and 5. As revealed in Figure 3.5 (a), the air split (1.3) in this case is high, such that the jet penetrates to the top wall without much deflection as the center streamline in the jet deflects only by ~0.5 d_j for a travel height of 6d_j. As noted previously, the jet width also remain fairly constant (spreads to ~1.5 d_j) as indicated by the distance between the windward and leeward streamlines. The centerline jet velocity remains nearly constant up to ~0.5H and drops to ~50% close to the top wall prior to stagnating. This means that the bottom jets reach the top wall with much of their momentum intact.
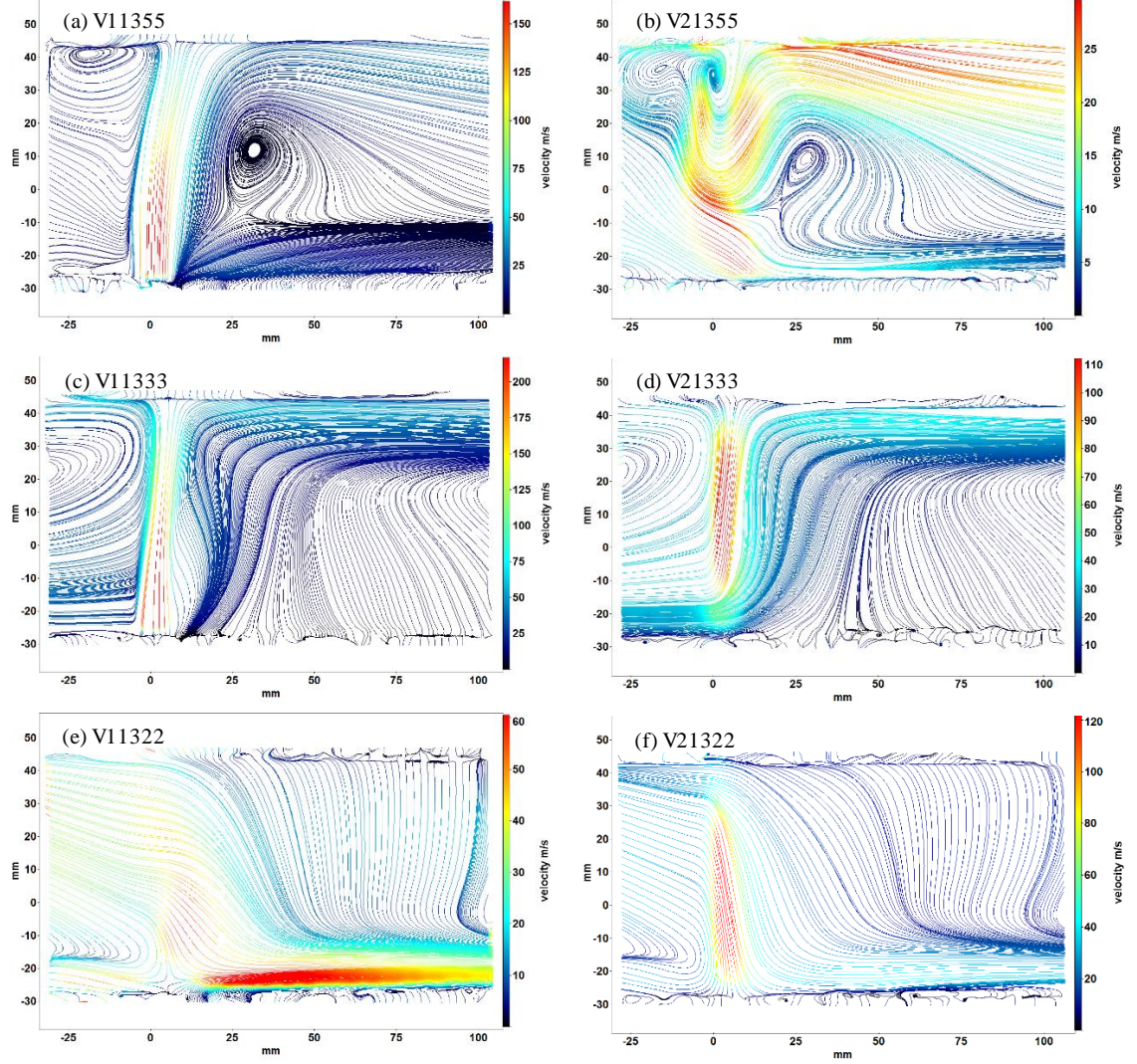
Figure 3.6: Streamlines with mean velocity field of CJICF obtained using 10kHz SPIV setup with *Split* = 1.3 for plane 1 (left) and plane 2 (right). (a, b) 5 staggered jets, *J* = 252. (c, d) 3 parallel jets, *J* = 701. (e, f) 2 parallel jets, *J* = 1578. Note the different color map scaling for each result.

This results in one of the most interesting flow features of CJICF, i.e., the "splash" region that is clearly shown in Figure 3.6 (a) in the upstream at the top wall by the streamlines forming a large recirculation region. The velocity in this recirculation region is very low indicating a high pressure stagnation zone. This stagnation zone creates a blockage for the oncoming crossflow which is then pushed downwards as shown by the

80

descending streamlines upstream of the windward side of the jet. The descent of the crossflow streamlines is noticeable up to $\sim2d_j$ upstream and $\sim1d_j$ above the jet exit. As the descending crossflow approaches the jet, it is entrained upwards in the windward shear layer of the jet as seen by the streamline turning upward sharply close to the jet. The stagnation region on the windward side is also clearly evident where the density of upwardly entrained streamlines increases drastically.

On the leeward side of the jet, shown in Figure 3.6 (a), firstly there seems to be a velocity node indicated by a source of streamlines near the bottom wall. This occurs as the fluid in the upward moving high velocity jet tries to entrain the slower fluid that traveled axially and around the jet. The streamlines that seem to originate near the bottom wall on the leeward side follow two distinctly diverging paths, i.e., some of the streamlines are entrained upward by the jets, while the remaining streamlines stay near the bottom wall and travel downstream having mostly axial velocity. An almost zero-velocity recirculation region on the leeward side of the jet is present between these diverging paths where some of the recirculating fluid goes upstream (opposite to the crossflow) before being entrained back downstream by the axially moving fluid near the bottom wall.

In plane 2, the velocity result for staggered jets (Figure 3.6 (b)) also reveal the two recirculation regions seen in plane 1 in the upstream and downstream of the jets. The downstream recirculation region in plane 2 has a similar shape but is smaller in size as compared to plane 1, indicating the three dimensionality of these recirculation regions. In plane 2, the region is not directly behind the jet but on the edge where the jet imposes lesser blockage on the crossflow. The upstream recirculation region in Figure 3.6 (b) has a distinct shape with what appears to be two recirculation cores. This occurs likely due to the

intermittently present upward and downward moving jet fluid in that region, which should be clarified by examining some instantaneous velocity fields. These recirculation zones provide high residence times for the fluid and effect mixing in these regions, a phenomena that will be later correlated with the flame characteristics in RQL and LQL studies in Chapter 4 and 5.

Upstream of the jets, as shown in plane 2 (Figure 3.6 (b)), the crossflow streamlines descend much closer to the bottom wall, and the crossflow appears to accelerate and squeeze through between the bottom jets where it would experience lesser obstruction from the top jet fluid. The obstruction by the bottom jet fluid on the top wall is higher than that by the top jet fluid near the bottom wall since more mass (1.5 times) is injected through the 3 bottom jets than the 2 top jets. This also means that the impingement of the top jets on the bottom wall is not as strong as the impingement of the bottom jets on the top wall, since the local J ratio near the bottom wall in the center plane of top jet would decrease because of the accelerated crossflow fluid, causing the top jets to deflect more in the downstream direction. If there were equal number of jets and mass flow from the bottom and the top, it the crossflow would be expected to divert towards the middle of the test section height. In that case, similar upstream recirculation zones would be expected both on the bottom and top walls. It is likely to have an annular combustor where the number of holes on the inner and outer casing are not the same, hence this top-bottom asymmetric jet placement is still of practical importance. Figure 3.6 (b) also shows that the descending crossflow streamlines that are above ~$2.5d_j$ height diverge upwards as they are passing the jets due to entrainment by the upward moving jets.

For the same air split (1.3), as either side of the staggered 5 jets are turned off, all the dilution air is pushed through the 3 bottom or 2 top jets thus causing an even strong jet impingement. For the 3 parallel jets (Figure 3.6 (c, d)), there are no opposing jets; thus the upstream recirculation region is much larger, extending beyond the field of view and is ~$3d_j$ tall. Downstream, as most of the fluid from the parallel jets ends up near the top wall (at least within the field of view), a huge recirculation region seems to be present which again is apparently centered beyond the observation window in the downstream direction. Both planes 1 and 2 (Figure 3.6 (c, d)) show similar flow features except that in plane 2 the crossflow passes through near the bottom wall (since no obstructing jet is present in this plane) and is entrained upward by the jet. Figure 3.6 (f) is similar (but inverted) to Figure 3.6 (d) since it also represents the edge plane (2) for a 2-jet parallel configuration.

In Figure 3.6 (e), which is the midway plane between two parallel jets, mostly crossflow should be present along with some higher velocity downward moving jet fluid. The upstream high pressure recirculation region extends in this plane as well, and the crossflow likely moves around it (towards the top wall) though this is taking place beyond the upstream edge of the observation window. What is seen in the imaged region is the descent of the crossflow fluid as it passes the recirculation zone and accelerates near the bottom wall.[1]

Since time-averaged results often do not reveal important features of the time-resolved flowfields, example instantaneous velocity fields for CJICF cases are shown for plane 1 (Figure 3.7) and plane 2 (Figure 3.8). The background color in these figures

---

[1]This observation will become more evident in results presented in the next section.

represents the local V_y (vertical) component; high upward (orange-red) or downward (blue-white) vertical velocity regions indicate the presence primarily of jet fluid.
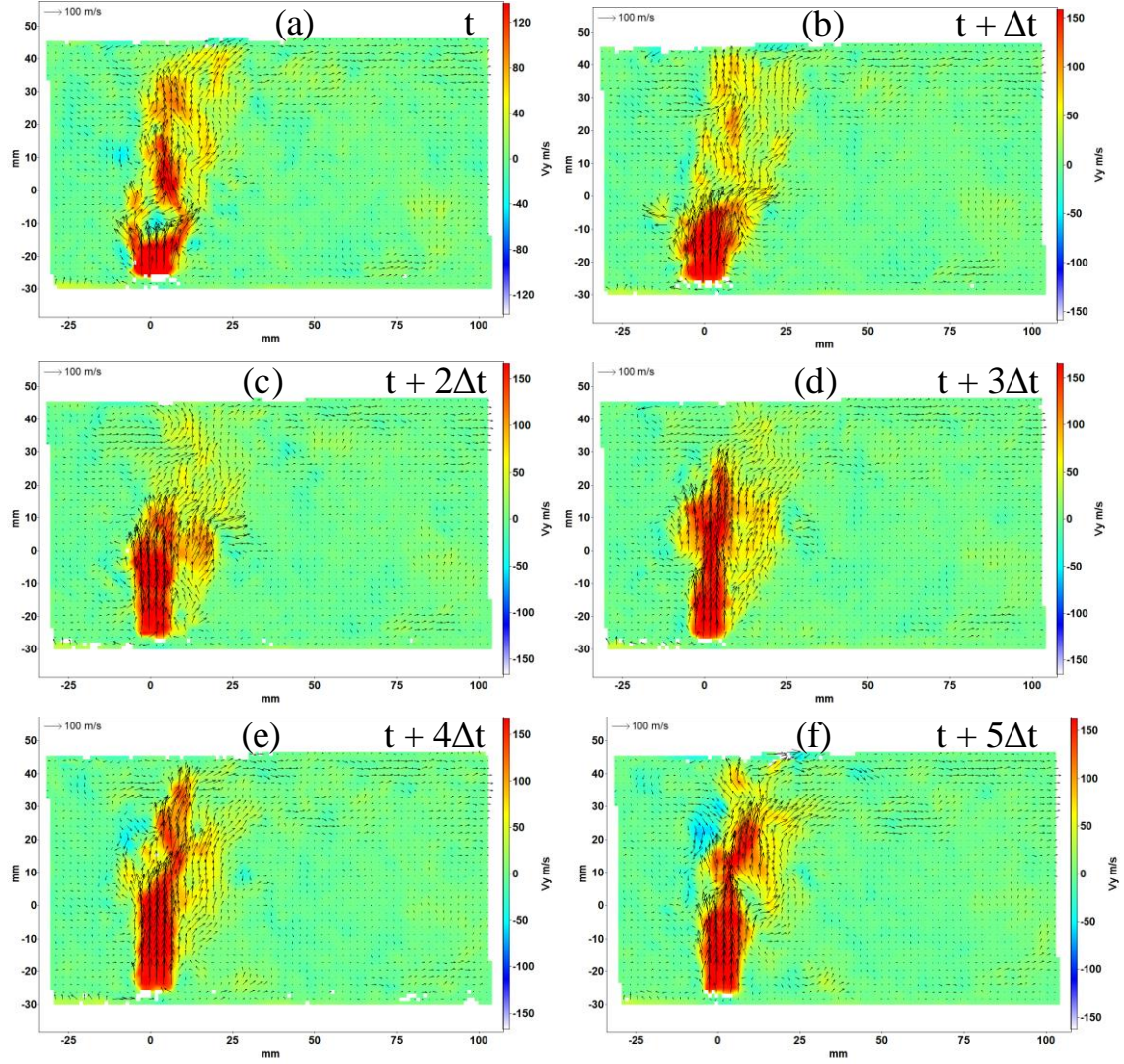
Figure 3.7: Time sequence of instantaneous images staggered jets configuration in plane 1 for air split = 1.3. Image shown in t = 0 is frame 90, Δt = 100 μs. Note the different color map scaling for the first image in the sequence (a).
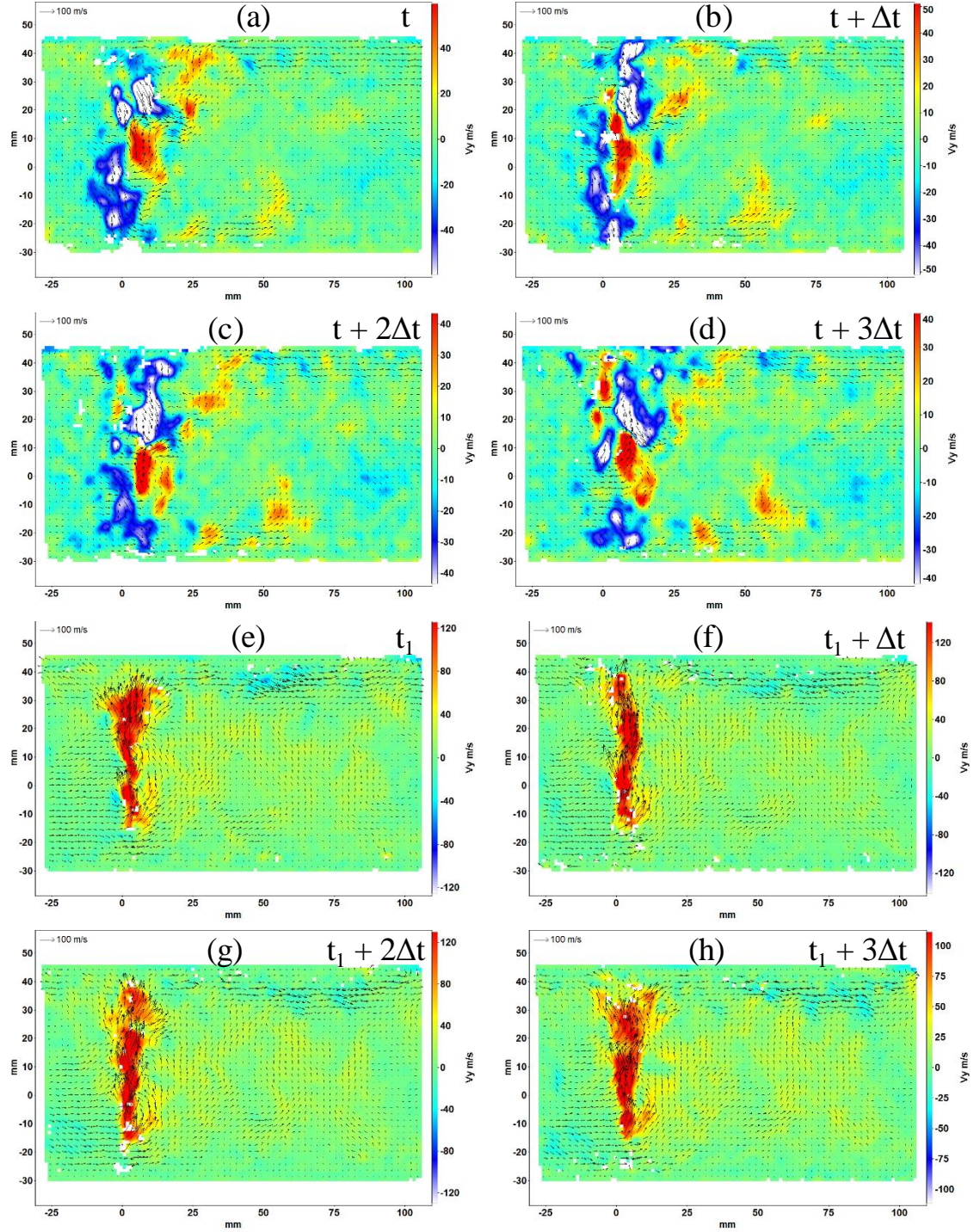
Figure 3.8: Time sequence of instantaneous images shown in plane 2. (a-d) staggered jets configuration. (e-f) 3 parallel jets. Air split = 1.3, image shown in t, $t_1 = 0$ is frame 20, $\Delta t = 100$ μs. Note the different color map scaling for each result.

For the staggered configuration, the results from plane 1 in Figure 3.7 (a, b) show sudden changes in the velocity at ~1.5 d_j height, likely due to lateral movement of the bottom jet. This could be caused by the top jet or crossflow interacting with the bottom jet. The bottom jet returns to the center plane in this lower region within 200-300 μs, but the process appears to repeat shortly thereafter, with the jet being pinched midway up (Figure 3.7 (e, f)). This suggests significant lateral deflection of the jet fluid is occurring often.

This lateral movement of the jets should also be present in the intermediate plane (plane 2), which is clearly evident in Figure 3.8. As expected with staggered-opposed jets (Figure 3.8 (a-d)), both upward and downward moving jet fluids, which originated from the bottom and top jets, can be simultaneously present in this plane that sits at the edge of both jets. Conversely, the parallel 3-jet configuration (shown in Figure 3.8 (e-h) does not have opposing jets from the top; hence the only high vertical velocity fluid observed is upward, associated with the bottom jets. Furthermore, the instantaneous jet structure for the parallel configuration changes less than for the staggered case. The bottom jet is nearly unbroken as it moves towards the top wall for the parallel case, whereas the staggered results reveal large pockets of fluid from one jet, separated by pockets of fluid from the other jet. Thus suggests significant jet-jet interaction in the staggered-opposed configuration, with large scale structures rapidly created in the shear layer between the jets.

For the staggered case, the instantaneous results also show descending fluid near the bottom wall, *but upstream of the windward side* of the bottom (upward) jets. As mentioned previously, the upstream recirculation regions (in Figure 3.6 (b)) are formed with the intermittent presence of upward and downward moving fluid; this is consistent with the instantaneous results shown in Figure 3.8 (a-d). *On the leeward side* of the bottom

jets, and in the region near the bottom wall, moderate size structures with high upward velocity occur. These structures could be due to fluid from the upward jet being sheared near the jet exit by the crossflow and carried downstream into the low pressure wake region. With increasing distance, these structures grow taller extending from near the bottom wall to ~midway of the test section height. The fluid in these structures could be entering this plane due to lateral motion from other planes. Some of this fluid could also be originating from the top jet after impinging onto the bottom wall where it mixes with the crossflow and the bottom jet. This is shown by the pockets of upward moving fluid that grow from the bottom wall towards the top wall.

Returning to the mean velocity results, the vorticities of the mean fields are presented in Figure 3.9, illustrating the jet trajectories, shear layers and the recirculation regions. Comparing the staggered and 3-jet parallel cases in plane 1 (Figure 3.9 (a, c)), the jet trajectory for the staggered case turns more than for the parallel configuration. This is most evident by following the low vorticity (white) region that marks the jet centerline. The windward and leeward shear layers for the staggered jets are also wider than for the parallel jets. This is likely due to the interaction between the interaction between the opposed (upward and downward moving) jets in the staggered case, which is absent in the parallel configuration.
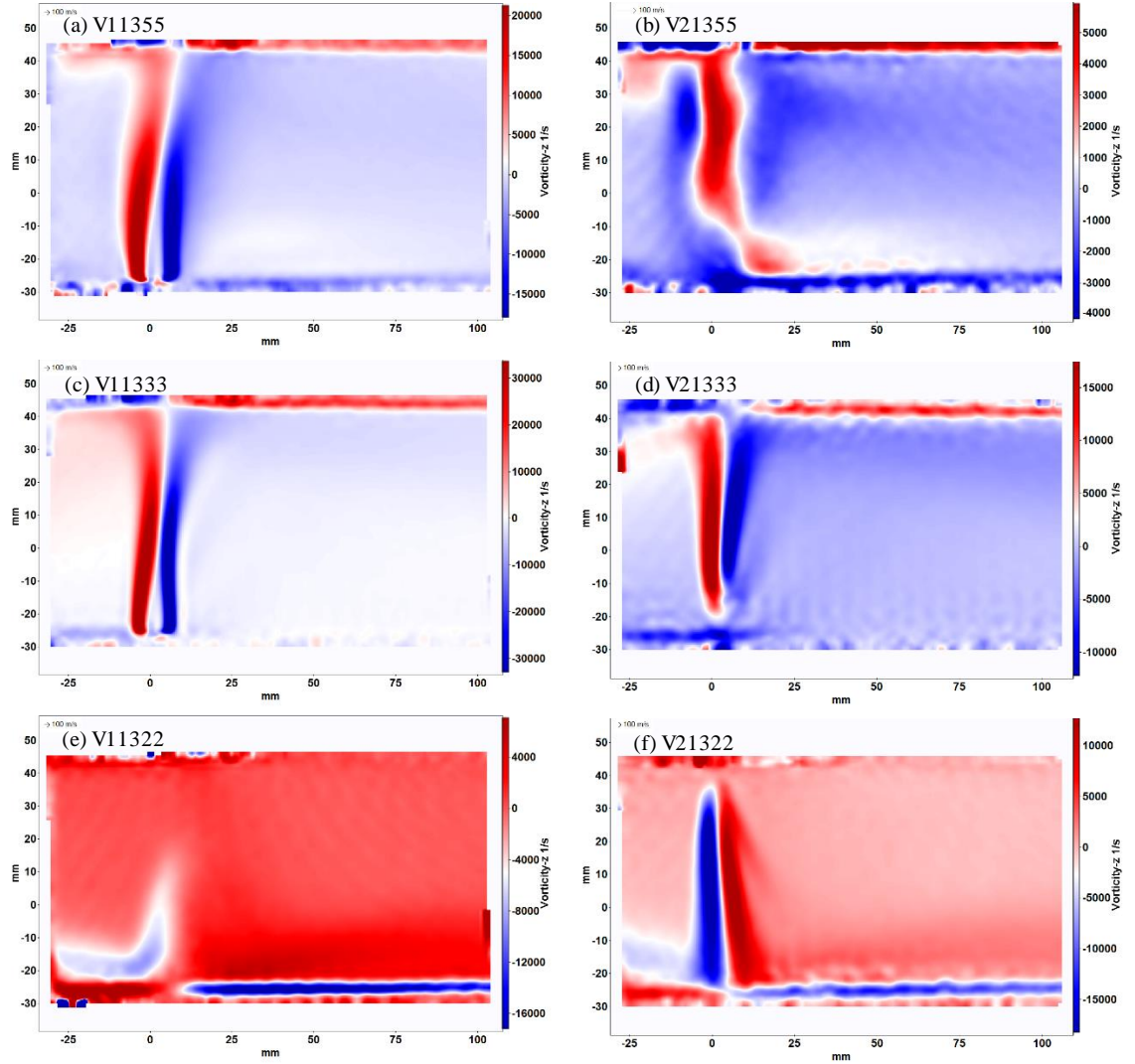
Figure 3.9: Mean vorticity field of CJICF (*Split* = 1.3) for plane 1 (left) and plane 2 (right). (a, b) 5 staggered jets, *J* = 252. (c, d) 3 parallel jets, *J* = 701. (e, f) 2 parallel jets, *J* = 1578. Note the different color map scaling for each result.

This interaction between the jets on the opposite side causes the distinct vorticity field of staggered jets in the edge plane (2) shown in Figure 3.9 (b), whereas the parallel vorticity field in the edge plane (Figure 3.9 (d)) shows the presence of entrained crossflow fluid and the presence of jet fluid due to lateral movement and jet spreading. As described previously and for the same reasons, the vorticity field of the 2-jet parallel case in the edge plane (Figure 3.9 (f)) is similar to that for 3 parallel jets (Figure 3.9(d)). The upstream

recirculation zone for 2 parallel jets in the midway plane (1) (Figure 3.9(e)) is also consistent with that shown by the streamlines (Figure 3.6 (e)).

3.3.2 *Constant J (75) CJICF Configurations*

The previous results compared the different jet configurations for a fixed air split ratio. As JICF flowfields are often parameterized by their momentum flux ratio, this section performs a similar comparison of jet configurations for a fixed J value of 75. Results based on the mean velocity fields at the same planes, and laid out in the same arrangement, are presented. The air split for the five staggered (and opposed jets), and the 3-jet and 2-jet parallel cases are 0.71, 0.43 and 0.28; as the number of operating jets is reduced, the air split decreases correspondingly. The results in this section are compared with those from Section 3.3.1 to examine the effects of air split and J ratios on the mean flow features of CJICF.

The jet penetration and width for the staggered and 3-jet parallel cases in plane 1 are shown in Figure 3.10 (a, c). The overall jet features are similar to those seen in Figure 3.5 for the higher air split (1.3). Even at these lower air splits, the jets clearly show penetration to the opposite wall, though the jet width increases slightly more ($\sim 2d_j$) when it approaches the opposite wall compared to the high air split (1.3) cases, which gave jet widths closer to $\sim 1.5d_j$. As might be expected, the jet trajectory turns more for the lower air split cases, which all have lower momentum flux ratios than the previous results. The biggest difference in jet features is seen in plane 1 for the 2-jet parallel configuration, i.e., by comparing Figure 3.10(e) for low J (75) and air split (0.28) with Figure 3.5(e) with a much higher J (1578) and higher air split (1.3). As expected, the jet turns much faster for

low *J,* as indicated by the presence of a wider region of downward moving fluid in the

middle of the test section in Figure 3.10(e).
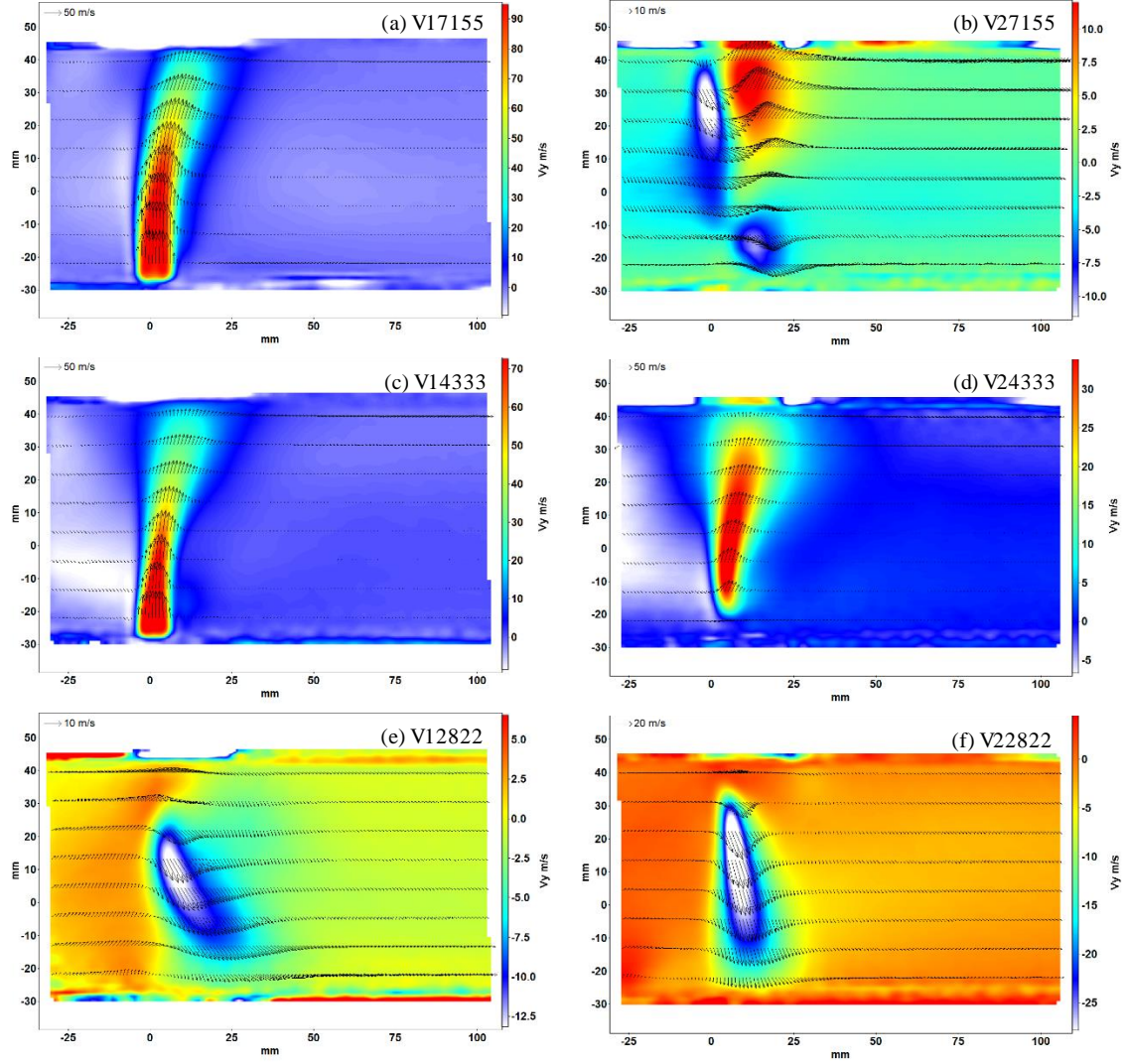
Figure 3.10: Mean *V_y* field of CJICF (*J* = 75) and velocity vectors at different heights for plane 1 (left) and plane 2 (right). (a, b) 5 staggered jets, *Split* = 0.71. (c, d) 3 parallel jets, *Split* = 0.43. (e, f) 2 parallel jets, *Split* = 0.28. Note the different color map scaling for each result.
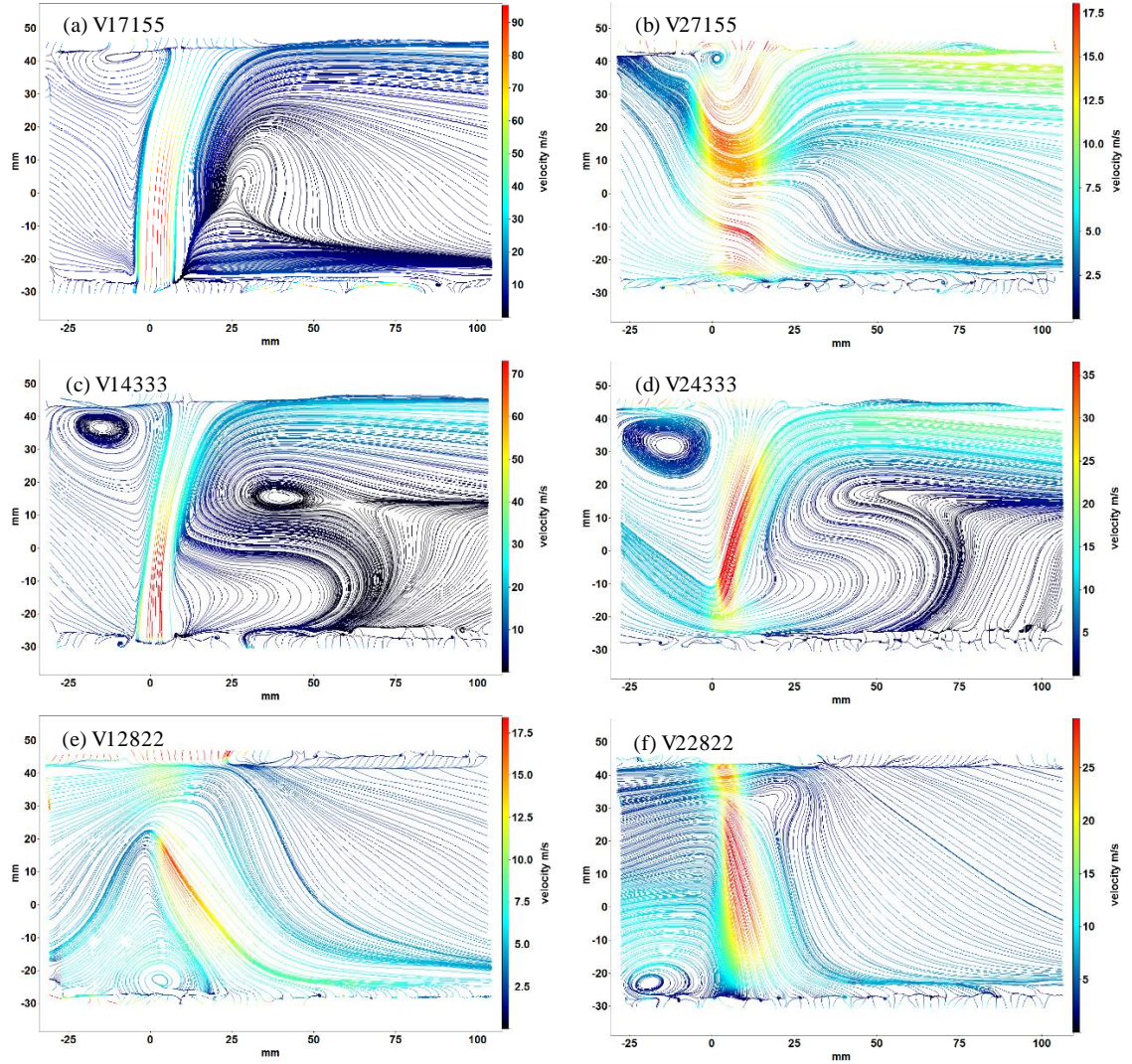
Figure 3.11: Streamlines with mean velocity field of CJICF obtained using 10kHz SPIV setup with *J* = 75 for plane 1 (left) and plane 2 (right). (a, b) 5 staggered jets, *Split* = 0.71. (c, d) 3 parallel jets, *Split* = 0.43. (e, f) 2 parallel jets, *Split* = 0.28. Note the different color map scaling for each result.

The two-dimensional streamlines and mean velocity are shown in Figure 3.11 for the *J*=75 cases. For staggered jets, both planes 1 and 2 (Figure 3.11 (a, b)) show similar flow features upstream of the jets when compared to the higher air split (1.3) case (Figure 3.6 (a, b)), except that the size of the upstream recirculation is smaller for lower *J*. For the

same cases, the downstream recirculation region in plane 1 (Figure 3.11 (a)) is also much smaller than before (Figure 3.6(a)) and is not evident in plane 2 (Figure 3.11(b)).

A similar observation can be made regarding the smaller size of the upstream recirculation regions for parallel jets (by comparing Figure 3.11(c, d, f) with Figure 3.6 (c, d, f)); again, the jet impingement on the opposite walls is weaker, hence producing a smaller upstream recirculation region. The reduced recirculation upstream of the jets is quite noticeable in Figure 3.11(e); the crossflow in this plane halfway between the two downward jets can now be seen to rise towards the top wall as it goes around the recirculation region produced by the stagnation of the jets splashing on the bottom wall. The crossflow fluid then moves back towards the bottom wall just upstream of x=0; this descent of the crossflow fluid occurred farther upstream in the previous case (Figure 3.6 (e)), and was in fact all that could be observed within the observation window. Smaller recirculation regions are also evident in the downstream region for the parallel jet cases, as seen in Figure 3.11 (c, d, f). The center of a recirculation region is now clearly present, which apparently was farther downstream in the test section for the higher air split results. The vorticity (see APPENDIX F) for these cases reveal the same general trends.

As noted above, the momentum flux and air split ratios for these three J=75 cases are all lower than the cases studied in Section 3.3.1 (split = 1.3). Furthermore, the current results produced smaller recirculation regions than the previous ones, and these recirculation zones have a significant impact on the flowfield in the mixing regions of the jets. So the question arises whether the decrease in J or in air split is the primary cause of the change. This can be answered by examining the two parallel jet configurations with the same J but different air splits (Figure 3.11 (d, f)). The 3-jet configuration with the

92

correspondingly higher air split produces the larger recirculation zone, even though each of its jets has the same momentum flux and therefore the same stagnation pressure as those in the 2-jet configuration. Therefore, it is fair to conclude that the size and impact of the recirculation zone in CJICF conditions is greater due to the higher mass of air being injected.

In summary, the CJICF flowfield is significantly different than the more extensively studied single, unconfined JICF flowfield. The large, confined jets highly influence the oncoming crossflow. The high pressure region produced due to impingement of the jets on the opposite walls produces large recirculation regions that significantly redirect the upstream crossflow. The jet-jet interaction in the staggered-opposed configuration, which is not present in for parallel jets, governs the flowfield in the intermediate plane. Overall, these jet-jet, jet-wall and jet-crossflow interactions greatly enhance mixing for CJICF.

CHAPTER 4.   RQL: AIR STAGED COMBUSTION

Combustion characteristics of air staged, Rich-Quench-Lean (RQL) combustors are examined in this chapter. Results are presented from experimental and analytical efforts carried to study the parallel and staggered flow configurations with multiple, large, preheated jets issuing transversely into a lower momentum, vitiated crossflow containing fuel rich products (including H_2 and CO) from the pilot burner. Flame stabilization modes, flame extent (burn out length), instantaneous flame boundaries and combustion features of reacting CJICF such as upstream burning (w.r.t. jets) are presented along with their dependence on the chemical time scales, mixing and velocity fields.

4.1   Flame Stabilization and Flame Extent for Staggered CJICF

Flame images acquired using low speed chemiluminescence diagnostics for the RQL experiments are shown in as the pilot equivalence ratio is varied from a lean (0.86) to rich (1.2) condition. In this case, all five dilution air jets are ON with a nominal air split ratio of 2.1 and average flow conditions shown in Table 4.1.

Table 4.1: Average flow conditions for low speed visible chemiluminescence experiments.

Air split	U_∞ (m/s)	$U_{j, top}$ (m/s)	$U_{j, bottom}$ (m/s)	$T_{\infty, preheat}$ (K)	$T_{j,top}$ (K)	$T_{j, bottom}$ (K)
2.12	35	264	271	592	475	521
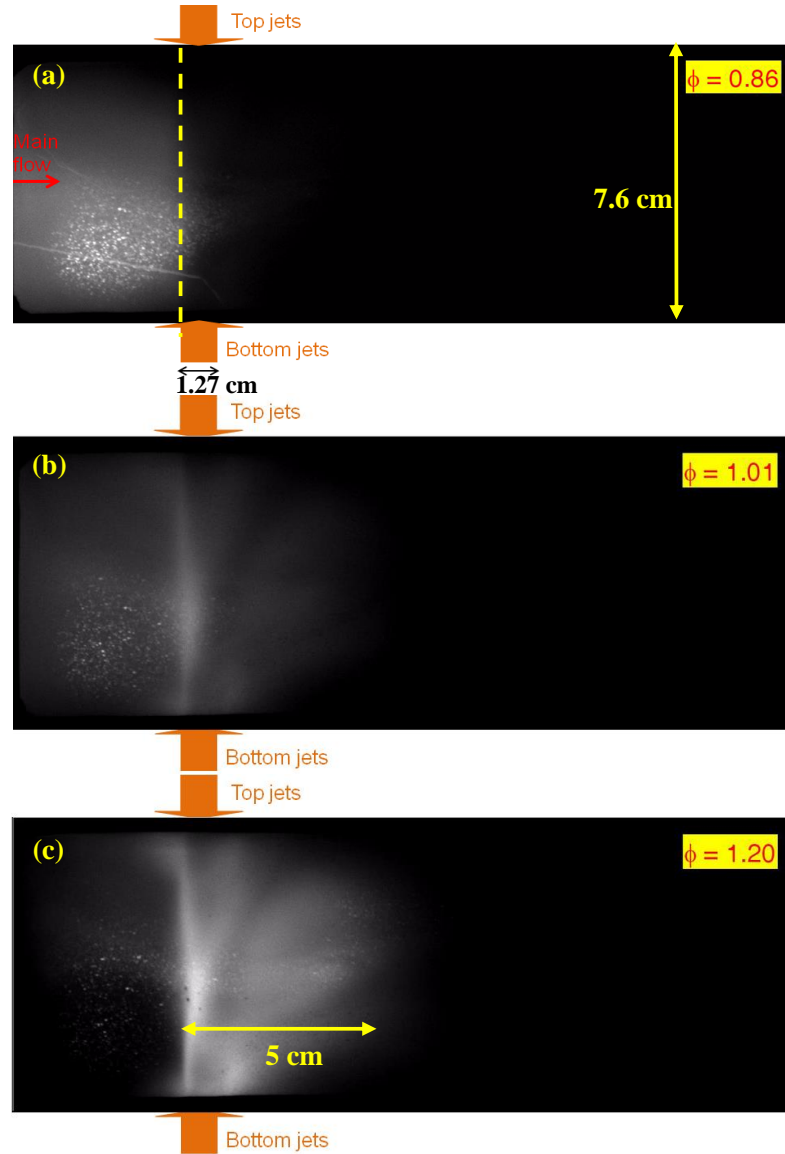
Figure 4.1: RQL chemiluminescence (average) images at three ϕ_pilot. Note the camera gain is adjusted to avoid saturation.

In Figure 4.1(a) for a crossflow composed of lean (ϕ=0.86) combustion products, it can be seen that the low level of emission from the pilot flow quenches right in front of the jets as the hot lean products are cooled by the dilution air. In Figure 4.1(b), with a slightly rich (ϕ=1.01) pilot combustor exhaust, the emission from combustion of the rich products (mostly H_2 and CO) with the dilution air appears immediately at the front (windward) edge

of the dilution jets. As the main combustor is operated at even richer equivalence ratio of 1.2 (Figure 4.1(c)), the chemiluminescence signal is much stronger than the radiation from the hot gases upstream of the jets, thus clearly marking the secondary fuel-lean staged combustion zone. Another interesting feature of these highly confined reacting jets is the apparent jet impingement on the opposite wall of the test section. This is clearly evident in Figure 4.1 (b,c), where the trajectories of the three bottom air jets are revealed by the darker region (reduced line-of-sight-averaged chemiluminescence in the core of the air jets). This "splash" on the opposite wall also coincides with heat release evident upstream of the air jets near both the top and bottom walls, indicating some of the jet air travels upstream due to its impingement on the wall; this is consistent with the flowfield results presented in the previous chapter. As the equivalence ratio is increased, the chemiluminescence (and presumably the heat release) continues to increase in intensity as more fuel is available to burn, with the emission extending roughly four jet diameters downstream from the leading edge of the jets for ϕ_{pilot} ~1.2, as shown in Figure 4.1. The sudden disappearance of chemiluminescence suggests that majority of the heat release has occurred and combustion is nearly complete. Although burned gas analyses would be required to concretely demonstrate this.

The chemiluminescence images shown in Figure 4.1 reveal three important features of the reacting RQL-type flow. First, significant heat release occurs on the windward side of the dilution air jets. Second, the heat release region formed by combustion of the dilution air and the rich vitiated crossflow is quite compact, extending only a few jet diameters downstream of the leading edge of the air jets. Third, evidence of significant interaction

between the air jet and the opposite wall of the combustor. Each of these features is examined in further detail below.

The burn out locations (or flame extents) extracted using edge detection of binary chemiluminescence images for RQL configuration with an air split of 1.3 are shown in Figure 4.2 for the pilot equivalence ratio increasing from 1.1 to 1.4. Note that the threshold intensity chosen to binarize the $\phi_{pilot} = 1.1$ case is relatively high such that only the very bright region is captured by the boundary, whereas the flame should still be closely attached near the jet exits as shown in Figure 4.1(c).
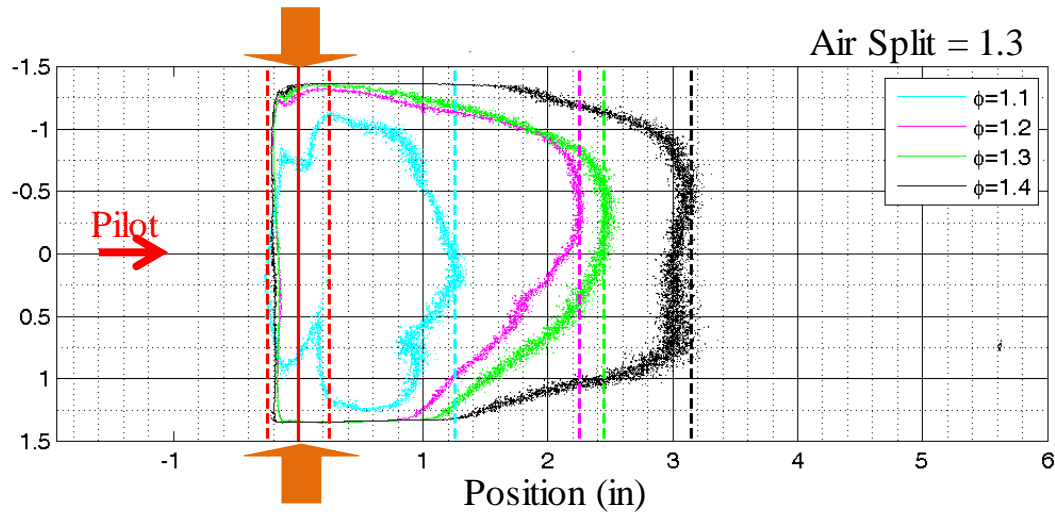
Figure 4.2: RQL Flame burn out locations marking downstream flame extent for air split of 1.3 using edge detection of binary flame images.

For the pilot equivalence ratios of 1.2 and 1.3, the flame burnout profile in the downstream is skewed towards the top half of the test section while for the $\phi_{pilot} = 1.4$ case, the burn out profile is relatively more symmetric between the top and bottom halves of the test section. This difference in the flame burn out profile shapes can be attributed to the fact that since there are three jets issuing from the bottom and two jets from the top, it takes

a few jet diameters to obtain the top-bottom uniformity as explained in Section 0. For the same mass flow rate of dilution air originating from each jet, initially about 1.5 times more dilution air ends up at the top half than at the bottom half, since in the downstream region closer to the jet exit, the jets fluid has not uniformly mixed with the crossflow fluid yet. This will be shown clearly by the top-bottom symmetry uniformity number (U_{sym}) in the mixing analysis section below.
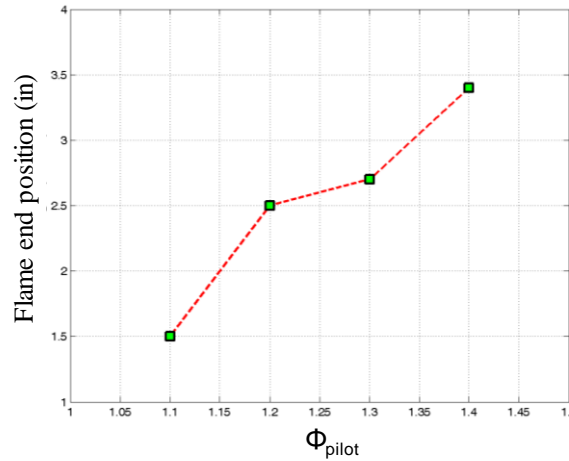
Figure 4.3: Increasing flame extent with increasing ϕ_pilot for RQL air split = 1.3.

The flame extent defined as the axial distance between the leading (windward) edge of the flame and the flame burnout location is plotted in Figure 4.3 for increasing ϕ_pilot. As the amount of unburned fuel (in the pilot exhaust) increases with ϕ, the axial distance needed for fuel to mix and react with the dilution air from the jets also increases roughly linearly with ϕ. This suggests that the combustion process is highly dependent on the mixing. If more fuel is added in the pilot burner (or ϕ_pilot is increased), it will take longer downstream distance for this extra fuel to mix with the available dilution air, of course,

assuming that there is sufficient dilution air from the jets available for the given amount of unburned fuel in the vitiated crossflow containing products from the rich pilot burner.

4.2 Autoignition Analysis at RQL Conditions

In the RQL setup, the flame attachment and appearance of heat release along the windward edge of the air jets can be interpreted using autoignition delay times calculated with a plug flow reactor model. As an example, autoignition times calculated for a pilot equivalence ratio of 1.2 (corresponding to an adiabatic temperature T_{ad}=2331 K) are presented in Figure 4.4. Calculations are performed for different mixing levels, denoted by jet-to-pilot mass ratio in the figure. For low mixing, the autoignition times are quite fast owing to the combustion of highly reactive H_2/CO vitiated products from the rich methane-air pilot burner at such high crossflow temperatures.
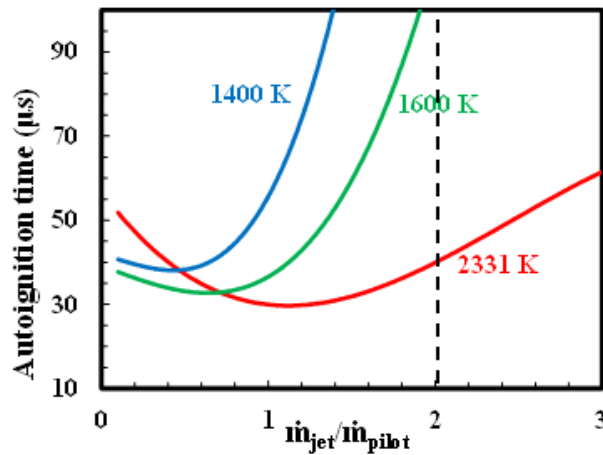
Figure 4.4: Autoignition times for RQL based on 20% rise in temperature.

Although the heat losses in the rig (between the pilot combustor and the test section) lead to lower crossflow temperatures (estimated to be between 1400-1600 K), the autoignition time scales are still very fast (~30-50 μs) for reasonable levels of mixing that

might be expected in the reaction zone. At high mixing levels (e.g., mixtures with more than 50% of their mass coming from the air jets), the lower resulting mixture temperature leads to a significant increase in autoignition times (though still representing relatively fast chemistry). Such fast autoignition times can explain the flame stabilization possible in the windward side near the jet exit where the vertical velocities are shown to be ~100m/s, which in turn leads to an autoignition length scale of ~3-5 mm. This is just a fraction of the jet diameter (d_{jet} = 12 mm) and is based on a conservative definition of the autoignition delay, based on 20% rise in temperature instead of one based on the rise in H mole fraction. This supports the explanation that in such a highly reactive environment, autoignition is able to achieve a nearly attached (stabilized) flame even on the highly strained windward side of a JICF.

The end of the combustion zone (or burn out location or flame extent) in the downstream can also be examined using the autoignition time scale. The axial velocity in the test section is estimated to be ~70 m/s after the pilot is mixed with almost twice the amount of air. Using the autoignition times with this velocity would result in an autoignition length scale < 10mm. Thus if the jet and cross-flow rapidly mixed, combustion would be finished within one jet diameter. But as seen in Figure 4.1(c), the staged combustion zone extends up to 5 cm (~4d_{jet}) suggesting that the combustion is mixing limited, i.e., reaction rates are fast enough that once high temperature unburned fuel (from pilot crossflow) and the dilution air (from jets) mix, combustion occurs rapidly. So the mixing process limits the extent of the combustion zone.

4.3 Mixing Field of Staggered CJICF

The relation between mixing and flame extent is explored further by revisiting the mixing field of staggered confined jets presented in the previous chapter. The uniformity numbers defined in that chapter are plotted in Figure 4.5 for a non-reacting (J =75, Split = 0.7) case with particle scattering images obtained in the bottom jet center plane with all 5 jets seeded but the pilot flow not seeded. Recall that U_{sym} represents the normalized difference in intensity between the top and bottom halves of test section at an axial location. As seen from the U_{sym} values (represented by solid circles), the staggered configuration has a relatively uniform distribution of jets fluid across the height of the test section at the jet entrance (at $x/d_j = 0$). Since there are three jets issuing from the bottom and penetrating towards the top wall, more jet fluid is present in the top region than in the bottom region. Hence, there is an initial rise in U_{sym} (at ~$1d_j$) downstream of the jets, which drops back as the flow mixes downstream (for ~ $4d_j$ - $6d_j$) and the jet fluid is more uniformly redistributed across the height of the test section.
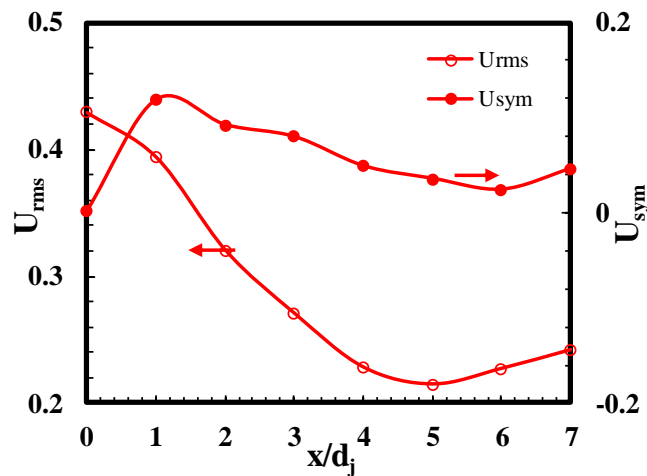
Figure 4.5: Uniformity numbers based on deviation from mean (U_{rms}) and top-bottom symmetry (U_{sym}) for non-reacting J =75, Split = 0.7 mixing case with all jets seeded and laser sheet in bottom jet center plane.

Recall that the axial uniformity number $(U_{rms})^2$ shows more uniformity indicating better mixing as U_{rms} approaches zero. Thus U_{rms} helps in identifying the minimum distance or length needed in a combustor for the flow to be uniformly mixed and consequently react for mixing-limited combustion. U_{rms} values shown in Figure 4.5 suggest that for a staggered CJICF configuration with J = 75, there is a non-uniform mixture at the jet entrance, which is expected since the jet fluid is contained primarily within the potential cores of the jets. Moving downstream, the jets fluid is stripped and redistributed by the oncoming crossflow and to a large extent due to interactions among the jets, and between a jet and the opposite wall of the test section. This leads to a more uniform mixture (lower U_{rms}) downstream of jet entrance.

With high J and air split ratio resulting in a confined flowfield, it is safe to assume that the mixing field and uniformity characteristics shown above for the staggered CJICF configuration closely represent the mixing field of the RQL flame results shown in Figure 4.1. The U_{sym} and U_{rms} results shown in Figure 4.5 both suggest that the jets and crossflow are uniformly mixed with the crossflow within a short distance (within ~ 4 - 6 d_j) downstream of the jets entrance. The flame extent results shown in Figure 4.1(c), Figure 4.2 and Figure 4.3 also demonstrate that the heat release region extends ~ 4 - 6 d_j downstream of the jets entrance. Based on these matching results from flame images and particle scattering images used for mixing analysis, it is concluded that the combustion is mixing limited for RQL configuration involving highly vitiated and reactive crossflow owing to the fast autoignition timescales.

---

[2]As defined in the previous chapter - it is calculated as a ratio of the standard deviation to the mean in a vertical strip in an image at a given axial position.

4.4   Flame Characteristics of Staggered and Parallel CJICF in RQL Systems

Flame characteristics of two jet configurations, namely staggered-opposed CJICF and parallel CJICF, are compared in this section for the jets consisting of preheated dilution air and for pilot flows of lean and rich equivalence ratios. All the cases presented here have a nominal air split ratio of 1.3, except for one parallel jets case with a split ratio of 0.78; this last case has the same nominal J ratio as the staggered jets case with a split of 1.3. In the following analysis, it is assumed that the OH*chemiluminescence intensity represents the combustion heat release. It should be noted, however, that the amount of signal received is not necessarily linearly proportional to the amount of heat release since previous studies have shown that the equivalence ratio and type of fuel (whether CH_4 or H_2-CO) also govern the chemiluminescence intensity. The gain and gate settings of the ICCD camera may also non-linearly scale the recorded intensity. However, for fixed camera settings and fuel composition, the relative intensity levels can be interpreted as proportional to the relative amount of heat release or burning.

4.4.1   Average Chemiluminescence Intensity Images

Average OH* chemiluminescence intensities for a lean pilot with air jets are shown in Figure 4.6 (a, b) for staggered jets (3 bottom and 2 top jets on) and Figure 4.6 (c) for a parallel CJICF configuration (only 3 bottom jets on). The air split ratio in these cases is fixed at 1.3, and the pilot burner equivalence ratio is increased from 0.8 in Figure 4.6 (a) to 0.85 in Figure 4.6 (b) and (c). Ideally, if the lean pilot burner had complete combustion such that absolutely no unburnt fuel was left in the vitiated crossflow before entering the test section, no chemiluminescence should be present. In fact, only a minimal amount of

light intensity is observed in these cases as compared to the rich cases presented in this section, even at a high camera gain (75%) with a 5 µs intensifier gate. In Figure 4.6 (a), the quenching of the pilot crossflow is evident at the leading edge of the jets with slight amount of luminosity in the leeward side of the bottom jets.
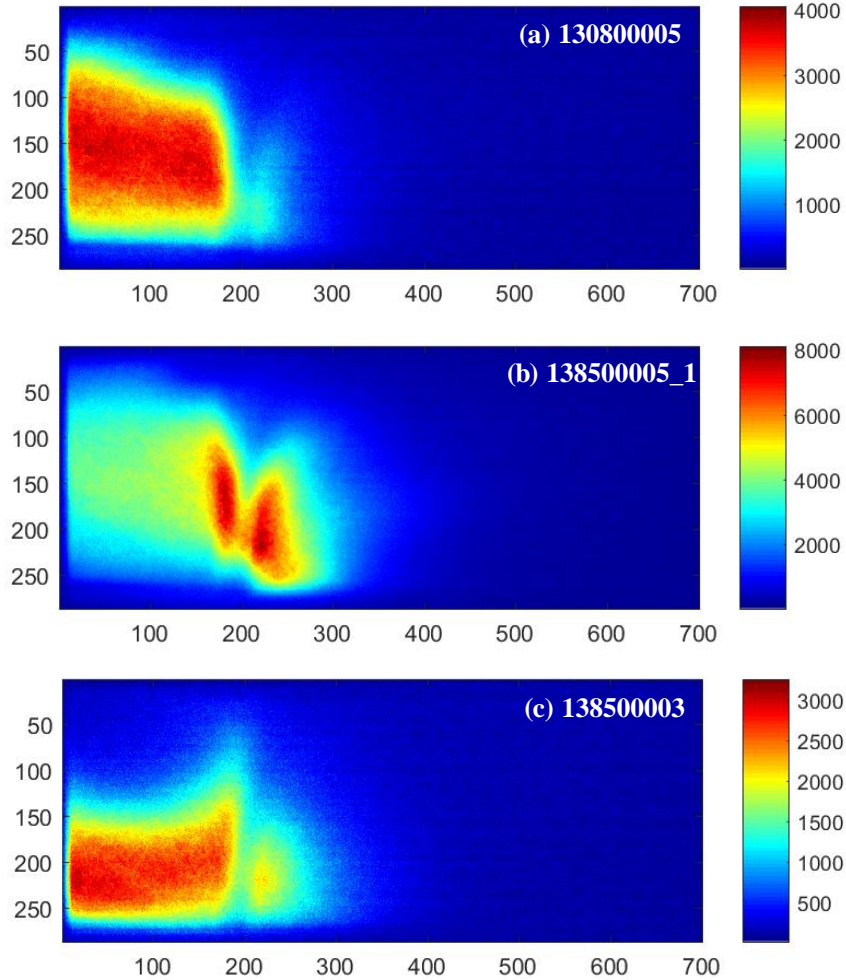
Figure 4.6: Average chemiluminescence intensity images for lean pilot and air jets. (a) Split = 1.3, ϕ_p = 0.8, 5 staggered jets, (b) Split = 1.3, ϕ_p = 0.85, J = 62, 5 staggered jets, (c) Split = 1.3, ϕ_p = 0.85, J = 173, 3 parallel jets. Note the different color map scaling for each result.

The mixing and velocity field results in the bottom jet center plane presented in the previous chapter revealed: 1) jet impingement or "splash" on the top wall, 2) recirculation

of jet fluid in the upstream of jets and 3) crossflow descending towards the bottom wall because more fluid originating from the three bottom jets ends up near the top wall. These features are also evident in all three cases shown in Figure 4.6. Low intensity luminescence is observed near the top wall where predominantly jet fluid is present; this inhibits chemical reactions and heat release due to lack of fuel in that region. As ϕ_p is increased from 0.8 in Figure 4.6(a) to 0.85 in Figure 4.6(b), more unburnt fuel exists in the crossflow, and it mixes with the jet air and burns in the windward and leeward shear layers, which are separated by the dark region representing the jet core of pure air. For the parallel jet configuration in Figure 4.6 (c), the bottom jets, which have a higher air flow rate than in the staggered configuration, create a strong splash on the top wall and push the crossflow downward, again agreeing with the velocity field results presented for non-reacting jets for same air split and jet configuration.

Overall, it should be noted that the maximum signal levels observed in Figure 4.6 are still very low (~120 times lower) than the signals presented for the rich pilot configuration shown in Figure 4.7 (a), when taking into account for the camera gain. Overall, for all practical purposes it is safe to assume the following: 1) the pilot burner has nearly complete combustion before entering the test section, 2) vitiated pilot crossflow upstream of the jets is deflected towards the bottom wall and 3) the jets are very effective in quenching the pilot flow on the windward side itself for both parallel and staggered-opposed CJICF configurations.
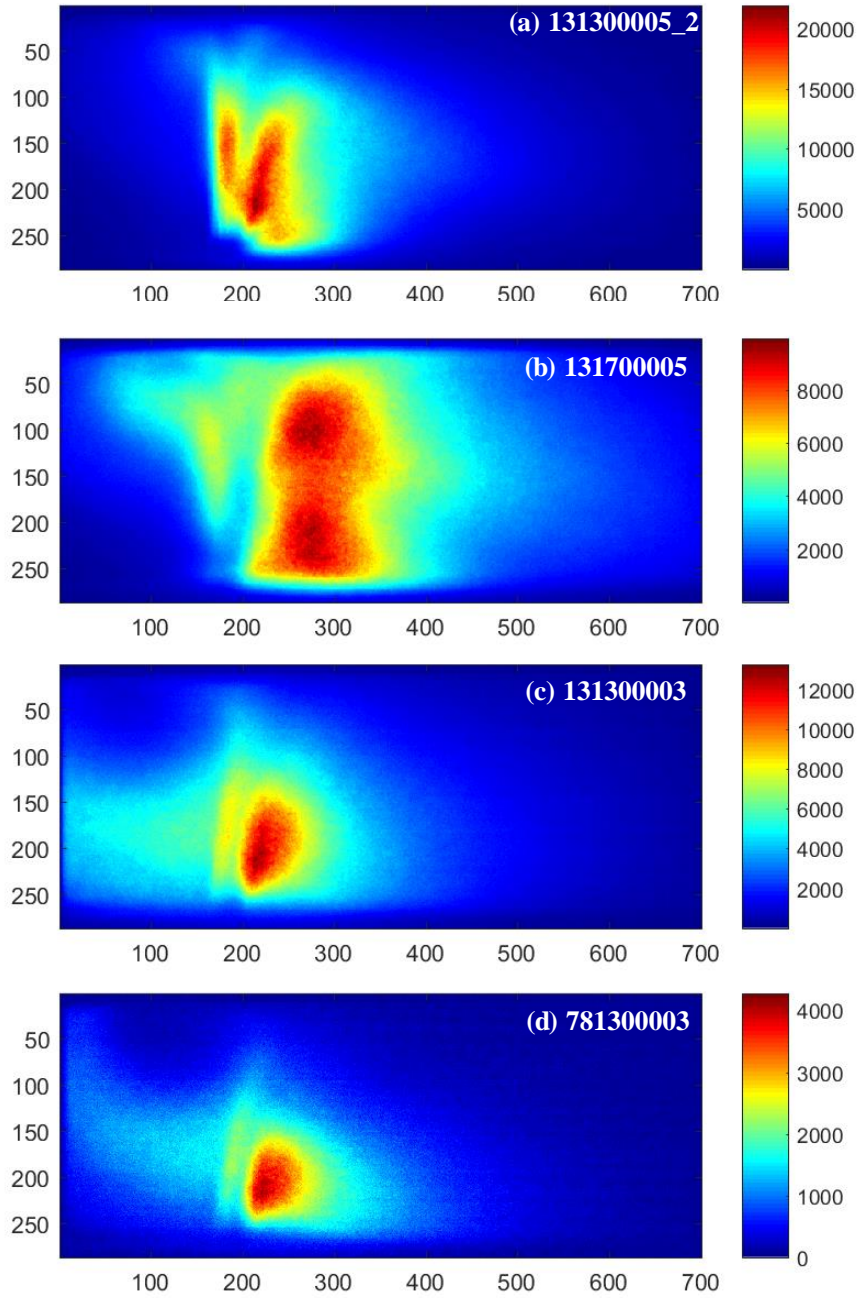
Figure 4.7: Average chemiluminescence intensity images for RQL CJICF conditions with rich pilot and air jets. (a) Split = 1.3, ϕ_p = 1.3, J = 62, 5 staggered jets, (b) Split = 1.3, ϕ_p = 1.7, J = 75, 5 staggered jets (intensity scaled x2), (c) Split = 1.3, ϕ_p = 1.3, J = 173, 3 parallel jets, (d) Split = 0.78, ϕ_p = 1.3, J = 62, 3 parallel jets. Note the different color map scaling for each result.

For a fuel-rich pilot with dilution air jets scenario that mimics RQL conditions, average OH* chemiluminescence intensities are shown in Figure 4.7 (a, b) for staggered-opposed and in Figure 4.7 (c, d) for parallel CJICF configurations.[3] The air split ratio in Figure 4.7 (a, b, c) is 1.3 and in Figure 4.7 (d) is 0.78 such that the parallel configuration has the same J ratio of 62 as the staggered configuration in Figure 4.7 (a). The J ratios for Figure 4.7 (b) and (c) are 75 and 173 respectively assuming adiabatic crossflow. The pilot equivalence ratios in Figure 4.7 (a, c, d) and Figure 4.7 (b) are 1.3 and 1.7 respectively. The contour plots for the intensity levels varying from 10% to 100% with increments of 10% are shown in Figure 4.8 for the same conditions. These contour plots are calculated from the mean images that are filtered using a second order Gaussian filter.

In agreement with the low speed result shown in Figure 4.1 (c) for the staggered CJICF RQL configuration., the high speed OH* image in Figure 4.7 (a) demonstrates similar average flame characteristics including an attached flame on the windward side of the jets, a compact combustion zone and a flame extent of few jet diameters. At first hand, the windward flame in Figure 4.7 (a) seems slightly lifted, but this is a manifestation of the imaging arrangement. In the high speed chemiluminescence setup, the camera is placed closer to the test section than in the low speed imaging setup. Due to this reason, the camera has a transformed view where the front and back edges of the test section on the bottom and top test section walls are both visible and the sense for depth is transformed from a three dimensional space into a two dimensional image. Effectively, the apparent positions of the jets have an offset in vertical direction from the front edge of the walls.

---

[3]Appendix F shows images with the same scaling for each case for comparing the low intensity regions.

Figure 4.8: Contour maps of average chemiluminescence intensity images for RQL CJICF conditions. (a) Split = 1.3, ϕ_P = 1.3, J = 62, 5 staggered jets, (b) Split = 1.3, ϕ_P = 1.7, J = 75, 5 staggered jets (intensity scaled x2), (c) Split = 1.3, ϕ_P = 1.3, J = 173, 3 parallel jets, (d) Split = 0.78, ϕ_P = 1.3, J = 62, 3 parallel jets. Note the different color map scaling for each result.

The heat release region with high intensity in Figure 4.7 (a) and in Figure 4.8 (a) is

more compact (or thinner) on the windward side than on the leeward side. The crossflow

stagnates on the windward side and forces the flame in the windward jet shear layer to be compact. Conversely on the leeward side, the jet shear layer is relatively free to expand and grow in the downstream direction, which leads to a more distributed flame.

The flame near the bottom wall that appears to be behind leeward side is likely to be between the glass window in front of the test section and the first bottom jet edge nearest to the window. The crossflow that is blocked by the jet fluid in the middle and top of the test section is diverted to descend and flow through the opening in this region near the side walls of the test section. The crossflow strips the jet fluid along the edge of the jet column where it ignites and stabilizes beside and slightly behind the leeward jet flame.

The upstream burning near the top wall is also evident in Figure 4.7 (a) and Figure 4.8 (a), but even more prominent in Figure 4.7 (b) and Figure 4.8 (b), where the jet fluid originating from the bottom jets splashes and recirculates at the top wall. Since about 30% more unburnt fuel is present in fuel-rich crossflow with $\phi_p = 1.7$ (Figure 4.7 (b) and Figure 4.8 (b)) than with $\phi_p = 1.3$ (Figure 4.7 (a) and Figure 4.8 (a)), the average flame shape for the two cases are quite different and are compared below.

Firstly, the windward jet shear layer shows a more distributed heat release zone that extends farther for higher ϕ_p since more fuel is available in the crossflow to mix and react with the jet fluid that was diverted upstream after impinging on the top wall. Secondly, the windward flame is more lifted for richer ϕ_p, since the crossflow adiabatic flame temperature is lower, resulting in longer autoignition times and thus longer residence times and lengths for flame stabilization. Thirdly, the heat release region on the leeward side is larger for the richer pilot case. A richer pilot has more fuel available in the crossflow that

needs to find air to burn. This air becomes available as the jet fluid is stripped by the entrained crossflow in the leeward shear layers of the jets. More fuel available in this region leads to a larger and much broader heat release zone. The heat release region shown in the leeward side near the bottom wall for the higher ϕ_p case is likely due to the flame near the side wall where the crossflow stripped and mixed with the fluid from the bottom jets. This heat release region integrated due to line of sight imaging should also cover the region between the jets where the crossflow mixes and reacts with the top jet air that turns slightly downstream and impinges on the bottom wall.

Although, the flame or heat release extends past the test section window for higher ϕ_p, most of the combustion (~80%) occurs within 6 jet diameters as shown in Figure 4.8(b). The intensity contours for lower ϕ_p (Figure 4.8 (a)) suggest that combustion is essentially complete within 6 jet diameters as well. As discussed in the previous chapter, mixing is also nearly complete within the same distance downstream which supports the conclusion drawn earlier that the combustion is mixing limited at these CJICF RQL conditions.

The flame shape for the parallel jet configuration shown in Figure 4.7 (c, d) and Figure 4.8 (c, d) is significantly different than that for the staggered jet configurations (Figure 4.7 (a, b) and Figure 4.8 (a, b)). This is expected as the mixing and velocity results showed drastically different flowfields for the two jet configurations as well. For a fixed air split (1.3) between the staggered and parallel configurations shown in Figure 4.7 (a, c), all the dilution air is injected only from the three bottom jets in the parallel configuration. Hence the momentum flux ratio for the parallel configuration almost triples (from $J = 62$ for staggered to $J = 173$ for parallel jets). This increased J ratio naturally results in a

stronger jet impingement on the top wall resulting in a larger upstream recirculation region as seen in the velocity fields from the previous chapter. This leads to the presence of mostly jet air and little crossflow fluid (fuel) and results in absence of heat release or flame in the upstream recirculation region as shown clearly in Figure 4.8 (c).

To study the effect of conserving momentum flux ratio (J = 62) between the staggered and parallel configurations (in Figure 4.7 (a, d)), the air split in the parallel configuration is reduced from 1.3 to 0.78. For this lower air split and J, the parallel jets are still highly confined and show similar flowfield features as the higher air split and J case. However, the size of the recirculation (or splash) region is smaller since the jet impingement is now weaker than in the high air split (1.3), high J (173) parallel case. This results in similar flame shapes between the two parallel jets cases, as shown in Figure 4.7 (c, d). One notable difference is the location of the darker region marking the absence of heat release in the core of the recirculation region; it sits closer to the jet injection location in Figure 4.8 (d) when compared with Figure 4.8 (c).

Another important distinction between the two jet configurations is that the leading edge flame in the parallel jets configuration turns downstream in the horizontal direction, while in the staggered configuration the leading edge is almost vertical and even extends upstream. This could occur as the parallel jets are pushed downstream by the high pressure stagnation zone in the splash region near the top wall. For the staggered jets, on the other hand, the dilution air originating from the bottom jets that splashes on the top wall is entrained and mixed along with the fuel in crossflow by the downward moving high velocity top jets. This leads to the availability of fuel-air mixture for the staggered case in the splash region near the top wall which in turn produces heat release upstream of the jets

near the top wall where otherwise there is no flame present in the parallel jets configuration. Furthermore, the presence of heat release upstream of the jets near the bottom wall in parallel configuration is due to the mixed fuel from crossflow with the air that originated from the bottom jets, splashed on the top wall, recirculated and reached upstream. The upstream heat release in the parallel jet configuration also helps stabilize the flame at the jet exit near the bottom wall, and the expansion from the upstream heat release may also cause the leading edge flame to turn downstream in the horizontal direction.

4.4.2   Instantaneous Chemiluminescence Intensity Images

This section examines the instantaneous flame behaviours, in contrast to average results, for the same four staggered and parallel CJICF RQL cases (with rich pilot) covered in Section 4.4.1. This includes: general flame shapes, upstream burning, the stability of the windward and leeward flames (i.e., attached versus lifted , and intermittent extinction), and large scale structure movements.

Firstly, representative instantaneous OH* chemiluminescence images (arbitrarily chosen as the last frames from each dataset) are compared in Figure 4.9 for each of the four RQL cases. Figure 4.9 (a) and Figure 4.9 (c) illustrate the windward and leeward shear layer burning regions separated by a darker region marking the potential core of the jet where mostly air is present. The weak chemiluminescence signal in this potential core region is due to the line-of-sight integration through the depth of the test section. The upstream burning characteristics of the instantaneous images shown in Figure 4.9 are also consistent with the average results from Figure 4.7.

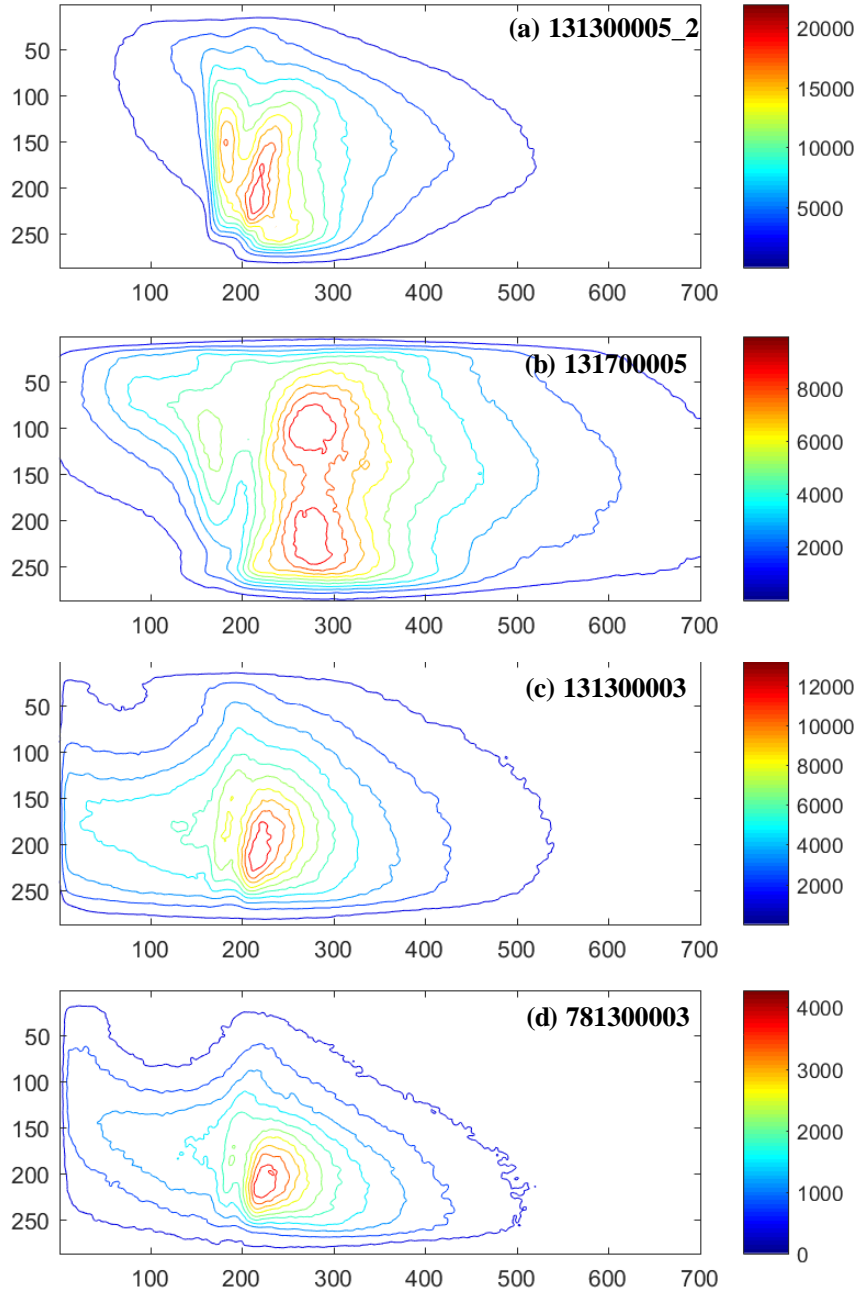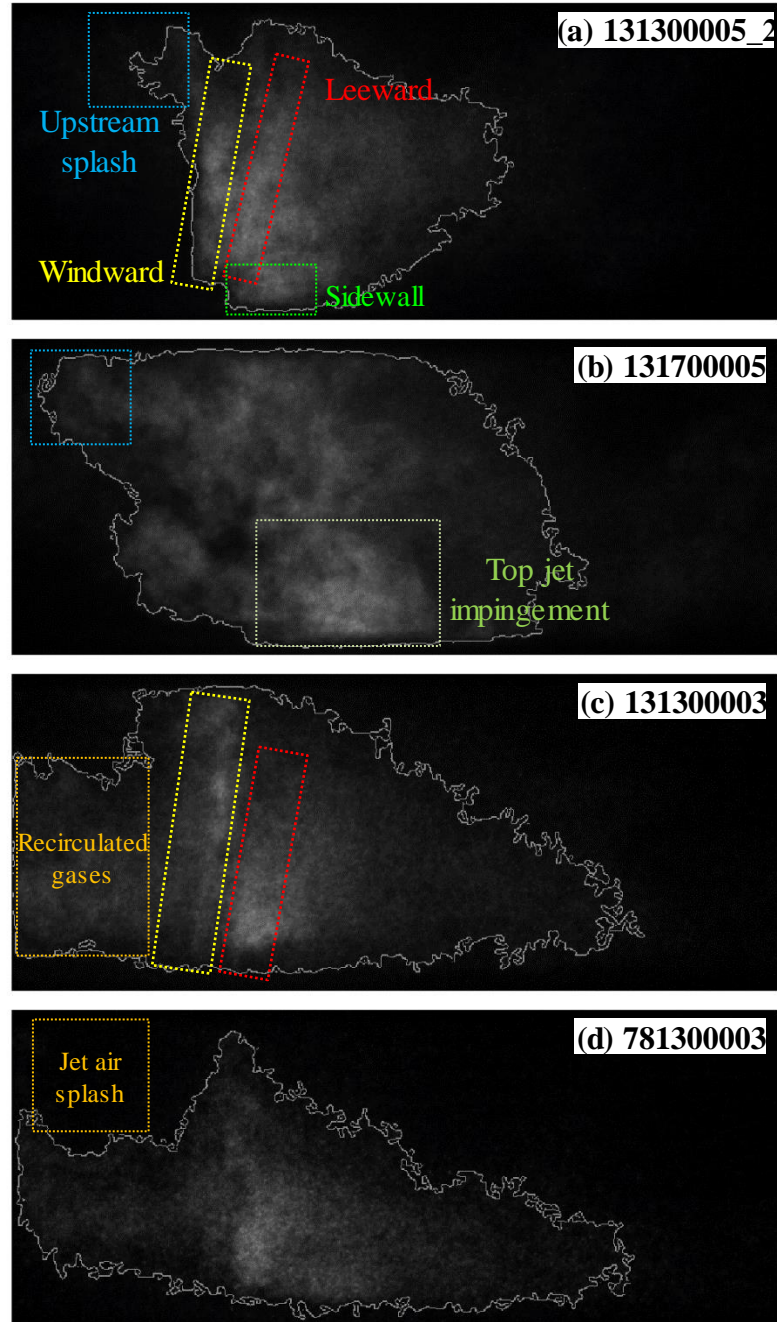**Figure 4.9: Instantaneous chemiluminescence intensity images for RQL CJICF conditions. (a) Split = 1.3, ϕ_p = 1.3, J = 62, 5 staggered jets, (b) Split = 1.3, ϕ_p = 1.7, J = 75, 5 staggered jets (intensity scaled x2), (c) Split = 1.3, ϕ_p = 1.3, J = 173, 3 parallel jets, (d) Split = 0.78, ϕ_p = 1.3, J = 62, 3 parallel jets. Note the different color map scaling for each result.**

The upstream burning region in the splash region for staggered jets with $\phi_p = 1.3$ (in Figure 4.9 (a)) is smaller than that for the richer $\phi_p = 1.7$ case (Figure 4.9 (b)) for the same reasons described earlier relating to the availability of more fuel in the upstream for the richer case. On the leeward side of the staggered jets, a uniformly distributed burning across the height of the test section is evident for the richer case shown in Figure 4.9 (b). This chemiluminescence signal on the leeward side near the bottom wall that extends far downstream is likely due to a combination of two heat release sources. The first is the reaction between the air that originated from the top jets, impinging on the bottom wall and then mixing with the fuel in the crossflow. The second is the reaction between the fluid that originated from the bottom wall that recirculates upstream and then mixes with crossflow fuel while descending downwards to the bottom. This latter fluid can stabilize in the region between the bottom jets and the side walls of the test section. Due to limitations of the line-of-sight imaging technique, it is hard to pinpoint these two sources of luminosity but further analysis of the instantaneous images will shed some light on this observation.

For the parallel jets configuration, the instantaneous images reveal that the case with the higher air split (1.3) and *J* (Figure 4.9 (c)) has heat release distributed in a larger region compared to the lower air split (0.78) case (Figure 4.9 (d)). This is likely due more air being available to burn for the higher air split, which also has improved mixing due to increased jet-wall interaction. In both Figure 4.9 (c) and Figure 4.9 (d), the dark region in the upstream is where the jets from the bottom impinge and splash on the top wall; hence, mostly jet air (and little or no fuel) is present in that region so reactions cannot occur. The chemiluminescence signal upstream of the jets in in Figure 4.9 (c) and Figure 4.9 (d) is

from the recirculated air that mixes and reacts with the oncoming crossflow after the splash or impingement on the top wall.

From examining the regions shown within the green outlines in Figure 4.10, it appears that the axial crossflow descending in the upstream of the jets entrains (or strips) and mixes with the air from the shear layer of the jets producing a flame region that moves back and forth in axial direction. This may be occurring in the region between the sidewalls of the test section and the bottom jets. This flame region is clearly observed in staggered CJICF RQL cases at both $\phi_p = 1.3$ and 1.6 conditions. For parallel jets, this flame region may be masked by the upstream burning flow and is hard to notice with the line-of-sight measurements.
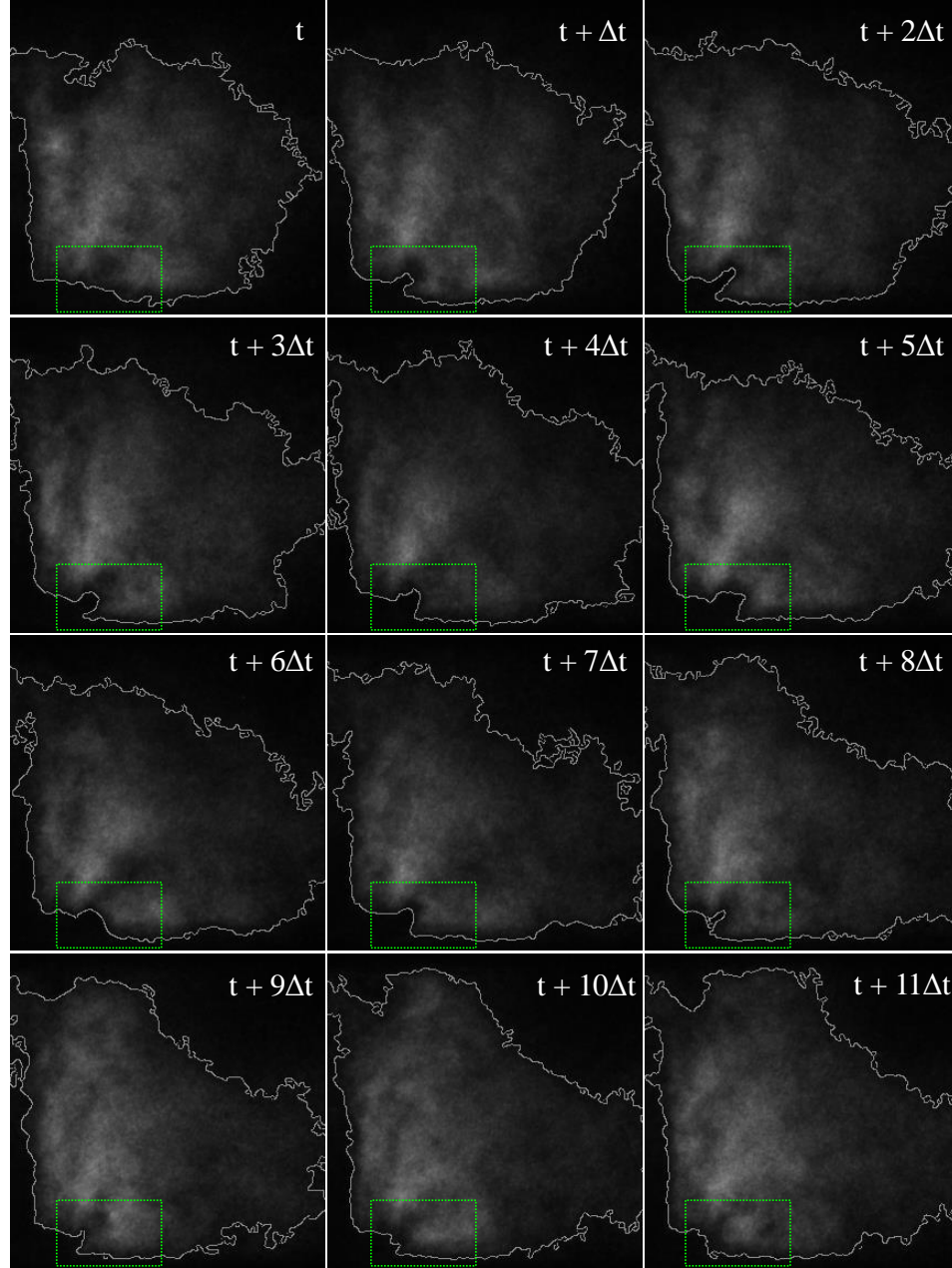
Figure 4.10: Time sequence of chemiluminescence images for staggered jets with ϕ_p = 1.3 with Δt = 100µs increments showing movement of the leeward flame in the sidewall region (t = 0 is 59th frame).
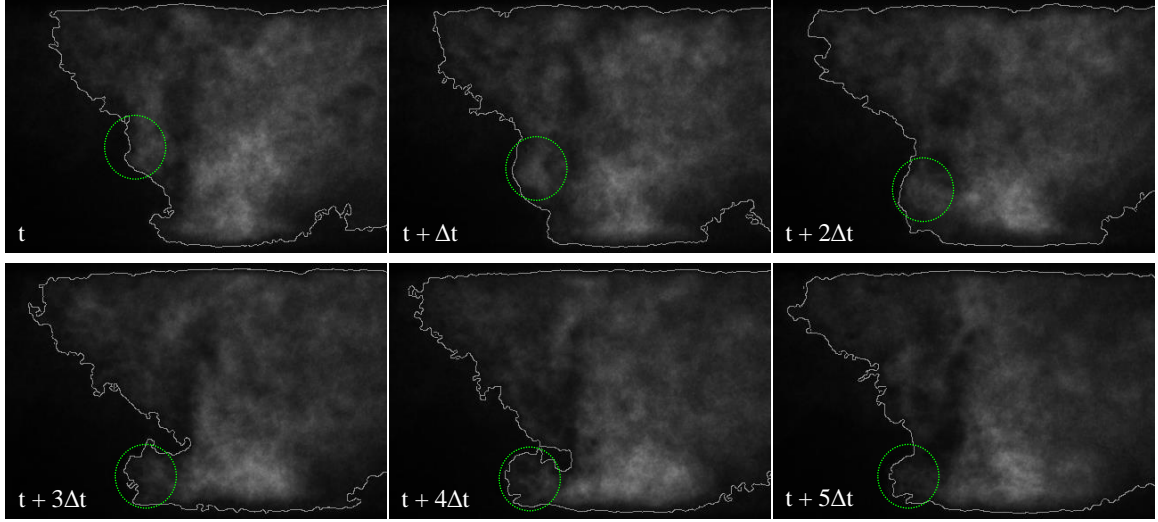
Figure 4.11:Time sequence of chemiluminescence images for staggered jets with ϕ_p = 1.7 with Δt = 100μs increments showing downward moving flame structure from the top jets (t = 0 is 11th frame).

In the richer case (ϕ_p = 1.6) of staggered-opposed jets (Figure 4.11 (a)), the windward flame near the jet exit is highly lifted, while the leeward flame is attached; this observation is consistent with the average image shown in Figure 4.7 (b). The flame is carried by the bulk motion of reacting fluid as shown in the time sequence of instantaneous chemiluminescence images in Figure 4.11, where a lifted flame on the top jets windward edge translates with the downward moving fluid that impinges on the bottom wall. The impingement of the top jets on the bottom wall is also evident in the contour plots shown in Figure 4.8 (b). As noted earlier, the impingement region of the bottom jets on the top wall is larger and extends farther upstream than that of top jets on the bottom wall, again due to more mass flow of air that ends up in the top wall from the three bottom jets as compared with that carried by to two top jets.
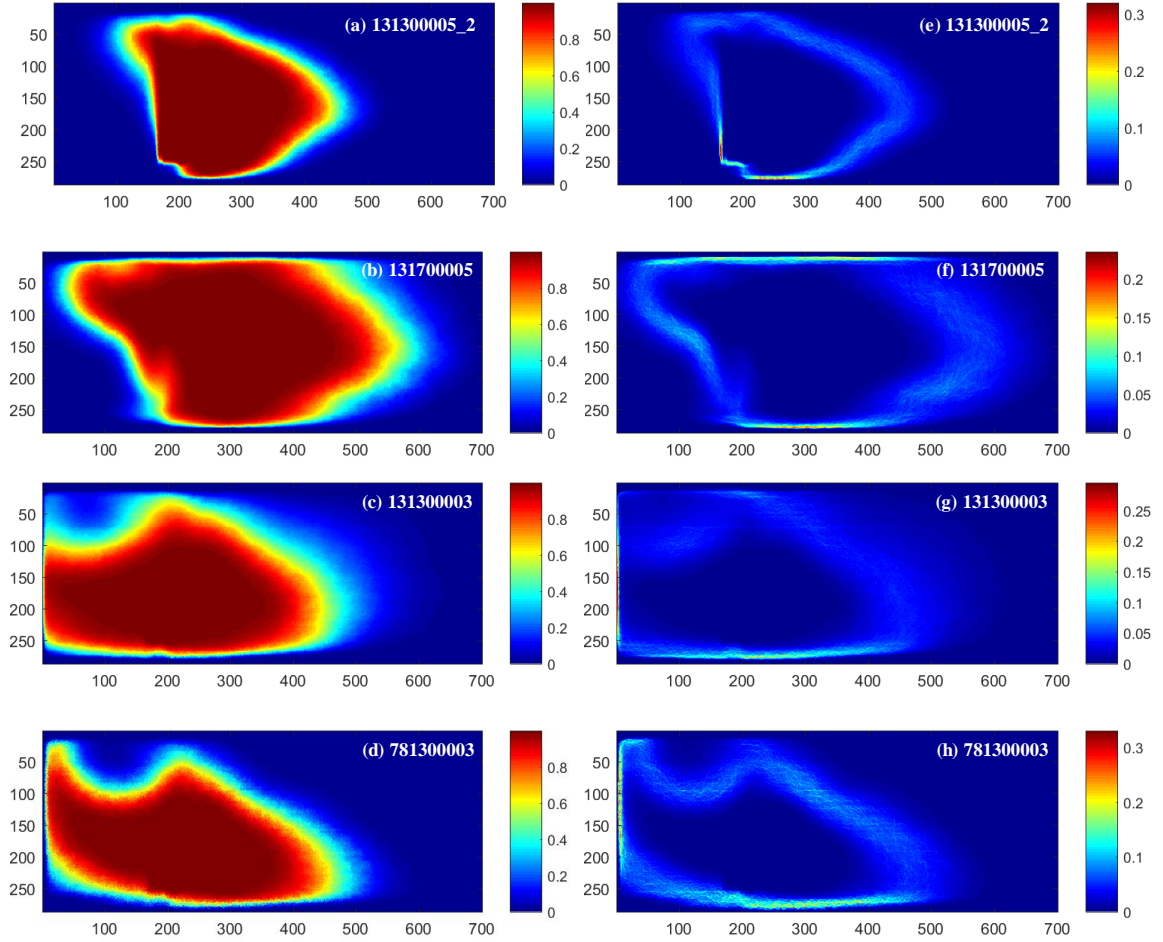
Figure 4.12: Mean PDF and edges of RQL CJICF conditions. (a, e) Split = 1.3, ϕ_P = 1.3, J = 62, 5 staggered jets, (b, f) Split = 1.3, ϕ_P = 1.7, J = 75, 5 staggered jets, (c, g) Split = 1.3, ϕ_P = 1.3, J = 173, 3 parallel jets, (d, h) Split = 0.78, ϕ_P = 1.3, J = 62, 3 parallel jets. Note the different color map scaling for each result.

Lastly, the mean PDF and flame edges are shown for the CJICF RQL cases in Figure 4.12. These images illustrate the intermittency of the flame in the various regions. There is a distinct central region for each case where the flame is always present. A compact windward flame stabilization zone is seen near the bottom jets for the staggered configuration with rich (ϕ_p = 1.3) pilot indicating an attached windward flame (see Figure 4.12 (a) and Figure 4.12 (e)). In contrast, the windward flame in the staggered jets with richer pilot (ϕ_p = 1.6) is lifted. Furthermore, the PDF results in Figure 4.12 (b) and flame

edges in Figure 4.12 (f) suggest an intermittent flame near the bottom jet exit, perhaps due to the unsteady motion of the top jets impinging on the bottom wall or intermittent autoignition occurring in the windward shear layer of the bottom jets. The windward flame stabilization in the bottom jets is not clear in the parallel jets shown in Figure 4.12 (c) due to line-of-sight integration of signal from the upstream recirculated fluid burning for high air split (1.3) case, but an attached windward flame is noticeable for the lower air split (0.78) case in Figure 4.12 (d).

There is an attached flame shown on the leeward side for each RQL case presented in Figure 4.12. This is consistent with the average (Figure 4.7) and instantaneous images (Figure 4.9) shown earlier. The edges far upstream in the parallel jets cases shown in Figure 4.12 (g) and Figure 4.12 (h) indicate that that the recirculation regions extend farther upstream ahead of the test section window. The downstream edges, which represent a flame brush, are contained within the field of view. The flame brush in the staggered (ϕ_p = 1.3) case is more compact than the wider flame brushes observed in the downstream for all other cases. This relates to the more consistent mixing capability of staggered jets in comparison with the parallel jets and also more consistent autoignition at higher temperatures as compared to the staggered (ϕ_p = 1.6) case. Overall, the downstream flame brushes for these CJICF RQL cases are only few jets diameters (2-3d_j) wide and the flame extent lengths are of the same order as mixing lengths ($\sim$ 4 - 6d_j), again suggesting mixing limited combustion for RQL systems involving CJICF conditions.

CHAPTER 5.   LQL: PREMIXED STAGED COMBUSTION

Combustion characteristics of premixed fuel-air CJICF in a Lean burn-Quick mix-Lean burn (LQL) combustor arrangement are examined in this chapter and compared with the air-staged RQL combustor results from Chapter 4. As in that chapter, high speed (10 kHz) OH* chemiluminescence measurements are presented for both parallel and staggered flow configurations. In addition, this chapter includes the response of the combustion to changes in crossflow (pilot) and jet equivalence ratios. The analysis approaches used to characterize the mean and instantaneous flame characteristics of the LQL CJICF are similar to those employed for the RQL CJICF. The observed combustion features are also related to the mixing and velocity field results presented in Chapter 3.

5.1   Overview of CJICF LQL Cases Studied

High-speed OH* movies for lean pilot conditions with preheated, premixed fuel-air jets were obtained for the staggered 5-jet configuration at two pilot equivalence ratios (0.6 and 0.85) and with the jets operated at a very lean (0.3) equivalence ratio and a moderately lean ϕ (0.8). The leaner pilot has an adiabatic flame temperature of ~1854 K, while the more stoichiometric pilot's is ~2222 K.[4] The air split ratio for all these cases was fixed at 1.3 (the same air split used in the staggered RQL results presented in the previous chapter). Example instantaneous images for each of these conditions are shown in the top two rows of Figure 5.1, the first row (a, b) contains results for the leaner pilot, while the

---

[4]These theoretical values do not include the pilot heat losses described in Chapter 2.

second row (c, d) shows the more stoichiometric pilot. The very lean jet cases are on the

left (a,c), while results for the less lean jets are on the right (b,d).

(a) 130603035

(b) 130608085

(c) 138503035

(d) 138508085

(e) 138508035

(f) 138508005

(f) 138508003

(h) 788508003
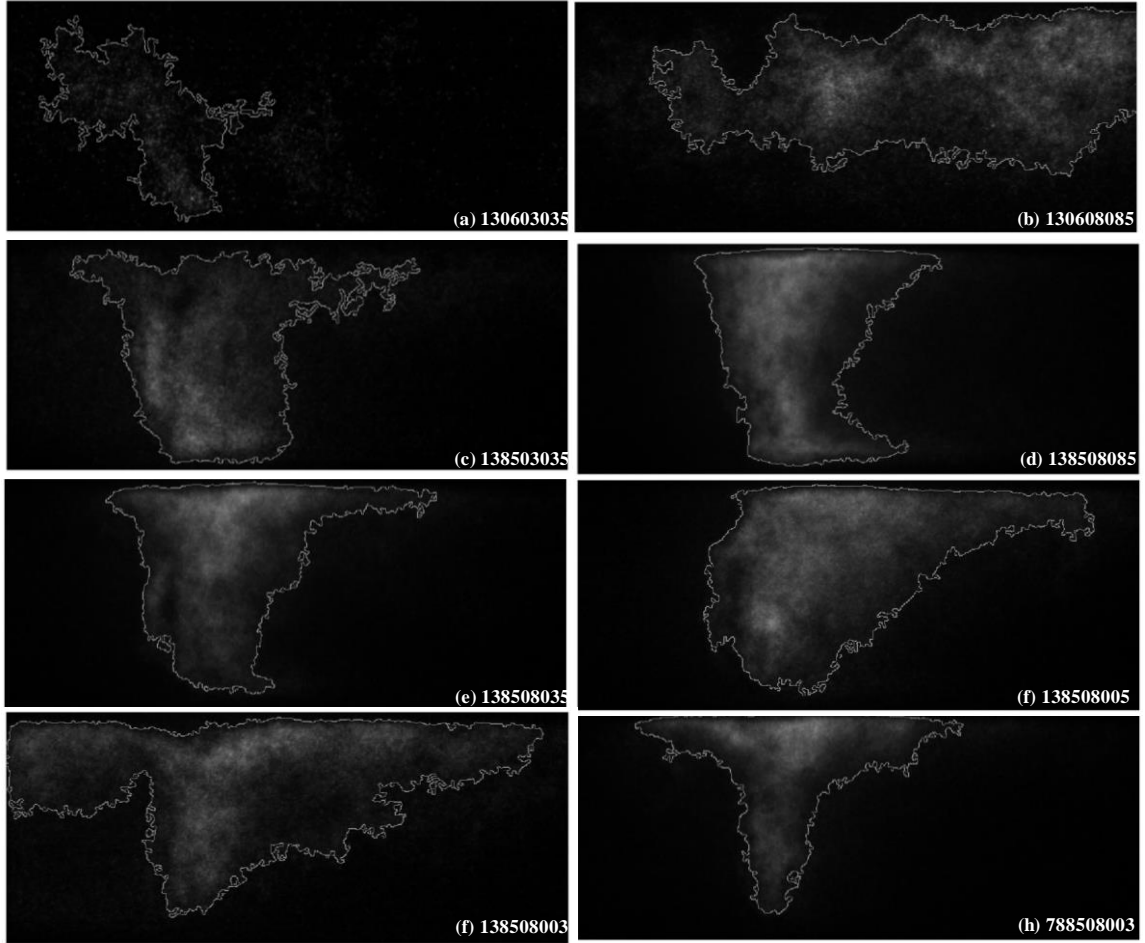
Figure 5.1: Example instantaneous chemiluminescence intensity images for LQL CJICF with staggered 5 jets (a-f) and parallel 3 jets (g, h), split = 1.3 (a-g) and 0.78 (h), ϕ_p = 0.6 (a, b) and 0.85 (c-h). (a) ϕ_{bj} = ϕ_{tj} = 0.3 (b) ϕ_{bj} = ϕ_{tj} = 0.8, (c) ϕ_{bj} = ϕ_{tj} = 0.3, (d) ϕ_{bj} = ϕ_{tj} = 0.8, (e) ϕ_{bj} = 0.8, ϕ_{tj} = 0.3, (f) ϕ_{bj} = 0.8, ϕ_{tj} =0, (g, h) ϕ_{bj} = 0.8.

Two additional staggered jet cases were examined; the conditions were similar to

that of Figure 5.1(d), with the more stoichiometric pilot (ϕ_p=0.85) and the less lean bottom

jets (ϕ_{bj}=0.8). In these two cases, however, the top jets were operated either at the lower

fuel condition (ϕ_{tj}=0.3) or with no fuel. Instantaneous results for these two cases are shown

in Figure 5.1 (e, f). Finally, two parallel jet configurations were studied. The first was similar to the conditions of Figure 5.1(f), except the top jets were not operated and air and fuel flow rates in the bottom jets were increased to maintain the same air split ratio (1.3) and the same bottom jet equivalence ratio (0.8). An example instantaneous result is shown in Figure 5.1(g). In the second parallel jet case, the bottom jet equivalence ratio and J (and thus velocity and mass flow rate) were kept the same as case f, thereby reducing the air split ratio to 0.78. The corresponding example instantaneous result is shown in Figure 5.1(h).

In all cases, the instantaneous OH* images were arbitrarily chosen as the last frames from each dataset. Also, all the remaining figures shown in this chapter follow the same arrangement of cases as that of Figure 5.1. The results in Figure 5.1 also include instantaneous flame edges calculated using the method described in Section 2.8.3; these instantaneous flame edges are used to produce the average flame edge results shown in Section 5.2.

Generally, the flame shape (combustion region) for the eight cases are notably different. For example of all the cases, the two with the colder pilot exhibit either the smallest combustion region (Figure 5.1(a)) or the farthest downstream burning (Figure 5.1 (b)). In comparing the signal levels between data sets, it is first important to point out that while all the camera outputs are scaled the same in these figures, the datasets in the first three cases (Figure 5.1 (a, b, c)) were acquired with a camera intensifier gain (70%), while the remaining datasets were acquired at a lower gain (60%). In all cases, the intensifier gate was the same (5 μs). So even with a higher gain, the colder pilot cases shown in Figure 5.1 (a, b) produce much lower intensity signals than the other cases. While the case with the

hotter pilot but very lean jet (Figure 5.1 (b)) is similar intensity levels to the remaining cases in the figure, its higher gain means it too has a lower OH* signal. These lower chemiluminescence levels suggesting lower heat release per unit area.

5.2 LQL CJICF Flame Characteristics

Mean OH* results for each of the eight cases are shown in Figure 5.3[5]; they are complemented with the intensity contours plots shown in Figure 5.4 outlining regions with 10-100% of the maximum intensity in increments of 10%. Note that in the pixel coordinates shown in these figures, the center of the jet exit is located at $x = 195$ and the jet exit (diameter) is 44 (i.e., $x = 173$ to 217).
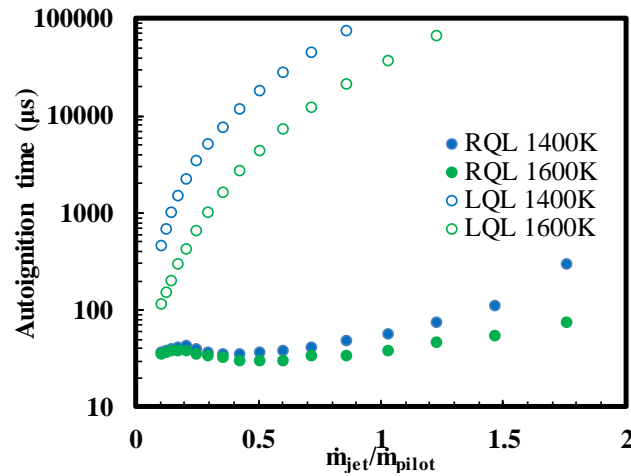
Figure 5.2: Comparison of τ_{auto} at T_{pilot} = 1400, 1600 K for RQL (ϕ_p = 1.2, ϕ_j = 0) and LQL (ϕ_p = 0.6, ϕ_j = 0.6).

A general comparison of the staggered LQL results shown in Figure 5.3 with the RQL cases shown in Figure 4.1 and Figure 4.7 indicate that the LQL flames are more lifted

---

[5]Appendix F shows the chemiluminescence images with the same scaling for each case so the reader can better compare the low intensity regions.

on the windward side. This is most evident by looking at the bottommost extent of the OH*

signal above the upward moving jets. The more lifted flames are likely due to longer

autoignition delays for the LQL versus RQL conditions. In comparing the LQL results for

the pilot cases with ϕ_p=0.85 (Figure 5.3 (c, d), the crossflow temperatures are similar to

those in the RQL studies. In the LQL experiments, however, the fuel that needs to

autoignite is natural gas from the jet, whereas in the RQL cases, the fuel is the H_2/CO from

the vitiated pilot products. H_2 is more reactive fuel than natural gas, and thus has faster

chemical rates and shorter autoignition delays as shown by the autoignition times compared

in Figure 5.2 for conditions close to those of the experiments. This conclusion about the

role of autoignition in stabilizing the jet flames is supported by the LQL results for the

colder pilot (first row), which are more lifted than their hotter pilot counterparts (second

row).

To further examine the LQL results, we begin with the staggered cases that most

closely resembles the previously studied RQL conditions, specifically those shown in

Figure 5.3(c) and Figure 5.4(c). As noted above, the pilot (crossflow) temperatures are

similar; $T_{ad,p}$ is ~2222 K for $\phi_p = 0.85$ and for the standard RQL pilot of ϕ_p=1.3.[6] The

difference in the LQL and RQL conditions is that the LQL jets are premixed with a small

amount of fuel ($\phi_j = 0.3$). The average LQL result shown in Figure 5.3(c) indicates a

compact combustion zone with a well-defined (sharp) windward leading edge, a thicker

leeward flame, and a low heat release jet core, more clearly seen in the contour version

(Figure 5.4(c)). The LQL mean combustion zone seen in Figure 5.3(c) closely resembles

---

[6] Mean OH* results for both pilot conditions with unfueled jets are shown in Figure 4.6(b) and Figure 4.7(a).

the RQL results for both the rich (Figure 4.7(a)) and lean (Figure 4.6(b)) pilots. Besides the already discussed higher lifting of the windward reaction zone for the LQL case, there is another important difference between the RQL and LQL flame shapes.
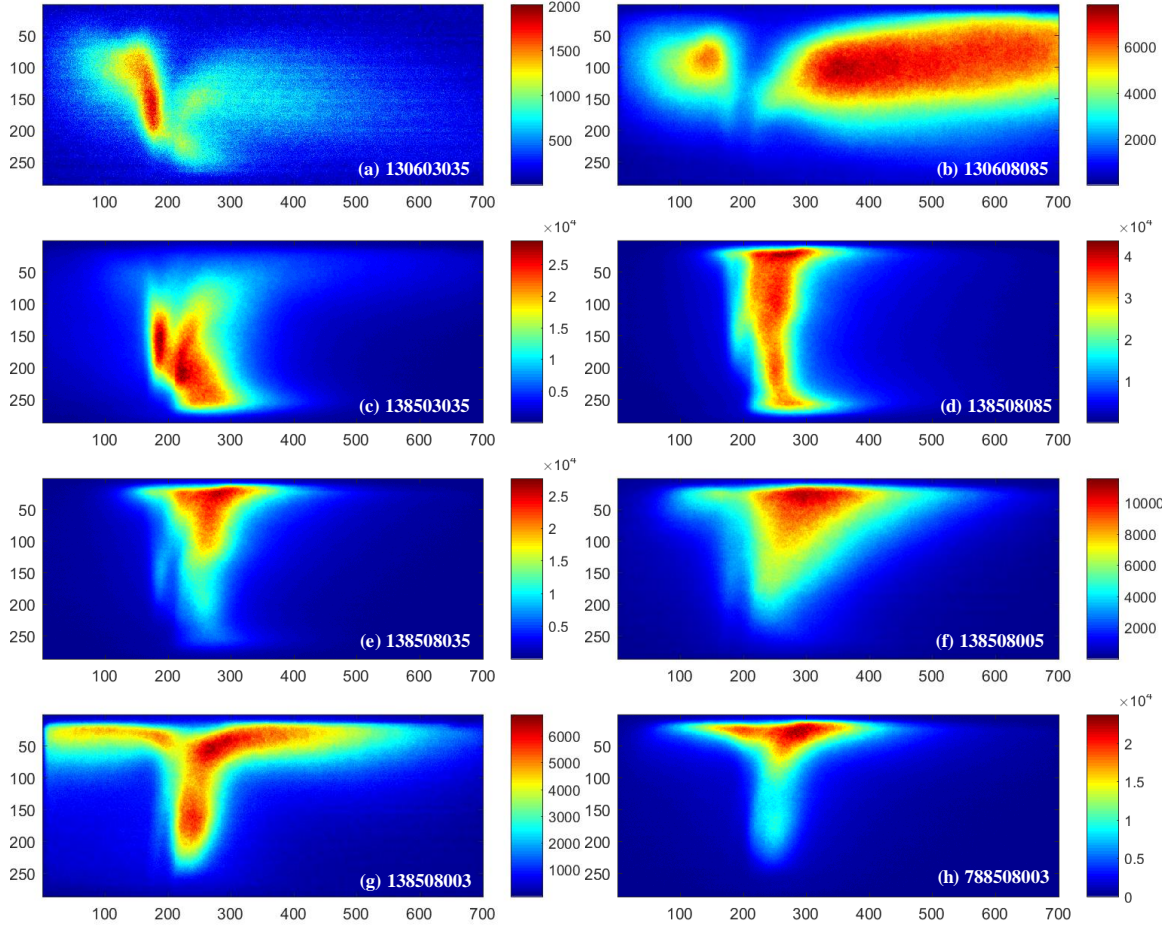
Figure 5.3: Average chemiluminescence intensity images for LQL CJICF with staggered 5 jets (a-f) and parallel 3 jets (g, h), split = 1.3 (a-g) and 0.78 (h), ϕ_p = 0.6 (a, b) and 0.85 (c-h). (a) $\phi_{bj} = \phi_{tj} = 0.3$ (b) $\phi_{bj} = \phi_{tj} = 0.8$, (c) $\phi_{bj} = \phi_{tj} = 0.3$, (d) $\phi_{bj} = \phi_{tj} = 0.8$, (e) $\phi_{bj} = 0.8$, $\phi_{tj} = 0.3$, (f) $\phi_{bj} = 0.8$, $\phi_{tj} = 0$, (g, h) $\phi_{bj} = 0.8$. Note the different color map scaling for each result.

Figure 5.4: Contour plots of unfiltered mean chemiluminescence intensity images for LQL CJICF with staggered 5 jets (a-f) and parallel 3 jets (g, h), split = 1.3 (a-g) and 0.78 (h), $\phi_p = 0.6$ (a, b) and 0.85 (c-h). (a) $\phi_{bj} = \phi_{tj} = 0.3$ (b) $\phi_{bj} = \phi_{tj} = 0.8$, (c) $\phi_{bj} = \phi_{tj} = 0.3$, (d) $\phi_{bj} = \phi_{tj} = 0.8$, (e) $\phi_{bj} = 0.8$, $\phi_{tj} = 0.3$, (f) $\phi_{bj} = 0.8$, $\phi_{tj} = 0$, (g, h) $\phi_{bj} = 0.8$. Note the different color map scaling for each result.

The LQL case shows more burning in the downstream portion of the splash region near the walls going downstream, whereas the RQL heat release extends more in the middle of the test section. These feature are more clearly evident in the contour plots (Figure 5.4(c) and Figure 4.8(a)). Since mostly air (and not much fuel) was present in the stagnation region near the wall for the RQL case (as indicated by the streamlines of Figure 3.6(a)), the air jets need to first mix with the crossflow in order to react. In the LQL configuration, the jets already have premixed fuel, so burning near the wall is possible as long as the flame

126

is stabilized somewhere, for example due to autoignition induced by some mixing with the high temperature crossflow.

The effect of increasing ϕ_j on flame shapes can be seen when comparing Figure 5.3(c) and (d) (or Figure 5.4(c) and (d).) Significantly more heat release (or more properly, chemiluminescence) is obtained at the higher ϕ_j conditions even at 10% lower intensifier gain settings. With higher ϕ_j, the flame shape is much more well-defined and compact as seen through the pdf and averaged flame edge results shown in Figure 5.5(d) and Figure 5.6(d).

As the pilot temperature is decreased, but with same ϕ_j (0.8), the flame shape is complete different (Figure 5.3(d) versus Figure 5.3(b)). For the colder pilot, the flame is more lifted as noted earlier. There is also a flame present in the upstream recirculation region created by the impinging jets on the top wall (recall Figure 3.6(a)). The jet fluid has a longer residence time in this recirculation region, which would allow combustion to occur even for reactants with slower chemistry. The absence of a flame near the bottom wall in Figure 5.3(b) is perhaps due to an overly lean mixture caused by mixing of the two downward moving jets with the descending crossflow observed in the velocity results (see Figure 3.6(a)). If sufficient mixing occurs, the reactants may become too lean to produce a stabilized flame. Note the upward moving jets are not exposed to as much crossflow fluid, so combustion is more likely in the upper region of the flow. Downstream in the splash region, an extended heat release region occurs; it is likely stabilized in the recirculation region (with long residence times) in the wake of the jets. Also, the contour plots (Figure

5.4(b)) clearly indicate the low heat release jet potential core that separates the two heat release regions in the windward and the leeward sides of the jet.

For the same lean pilot, comparing the staggered LQL cases that have "leaner" jets (ϕ_j=0.3, Figure 5.3(a)) with the richer jets (ϕ_j=0.8, Figure 5.3(b)), the significantly lower OH* intensities,[7] and presumably reduced volumetric heat release, combined with the reduced flame extent suggests less fuel is burning for the lean jets. Moreover, comparing Figure 5.4(a) with Figure 5.4(c) (also with ϕ_j=0.3), the leaner pilot case again has much less heat release. Since the amount of fuel in the jets is the same in these latter two cases, the logical conclusion is that only partial burning of the fuel occurs; much of the fuel in the jet remains unburned. This is possibly due to excessive mixing with the crossflow, reducing the mixture equivalence ratio, and/or flame speeds too low for the ϕ_j=0.3 fluid to produce a stabilized flame without the help of the hotter pilot gases.

We can now consider the staggered cases with variation in fuel supplied to the top jets, i.e., Figure 5.3 (d, e, f,) with $\phi_{tj} = 0.8, 0.3, 0$. The most notable trend is the significant increase in the extent of the burning in the top splash region as ϕ_{tj} is decreased. This growth in the size of the splash region is also clearly evident in the contour results of Figure 5.4. As the fuel is removed from the top jets, less burning can occur near the bottom wall. With less heat release near the bottom wall, and thus less dilatation, the high pressure in the bottom wall stagnation zone should decrease, relative to the stagnation zone in the top, where the bottom jet fluid with ϕ_{bj} =0.8) is burning. Thus the crossflow will see a more adverse pressure gradient near the top wall, and deflect even more towards the bottom wall,

---

[7]These low signal levels adversely affect the contour plot calculations shown in Figure 5.4(a).

and begin this further upstream of the jets. This allows the top splash region to extend farther upstream, and along with the burning of the bottom jet mixture.

In addition to the growth in the splash region for cases (d)-(f), the increase in the intermittency of the combustion region is clearly seen in the pdf results of Figure 5.5 and the average of the instantaneous flame edges shown in Figure 5.6. One important question that motivated these experiment with unequal jet equivalence ratio was to identify if the heat release in the far field of one jets from one side supports or hurts the flame stabilization in the nearfield of the jets on the opposite side. The liftoff height of the flame stabilized on the windward side of the bottom jets does not change across these three cases in Figure 5.5 and Figure 5.6. Thus, the reduced heat release from the top jets in the region near the bottom wall does not produce a noticeably adverse effect on the stability of the bottom jets. But this does not necessarily mean that the heat release from the top jets could not have a helpful effect under some conditions. In the current arrangement, the pilot and bottom jet equivalence ratios are similar (0.85 and 0.8), so a stabilization enhancement would not be noticeable regardless if the opposite jets are fueled or not-fueled. This effect could perhaps be more prominent for a leaner pilot crossflow.
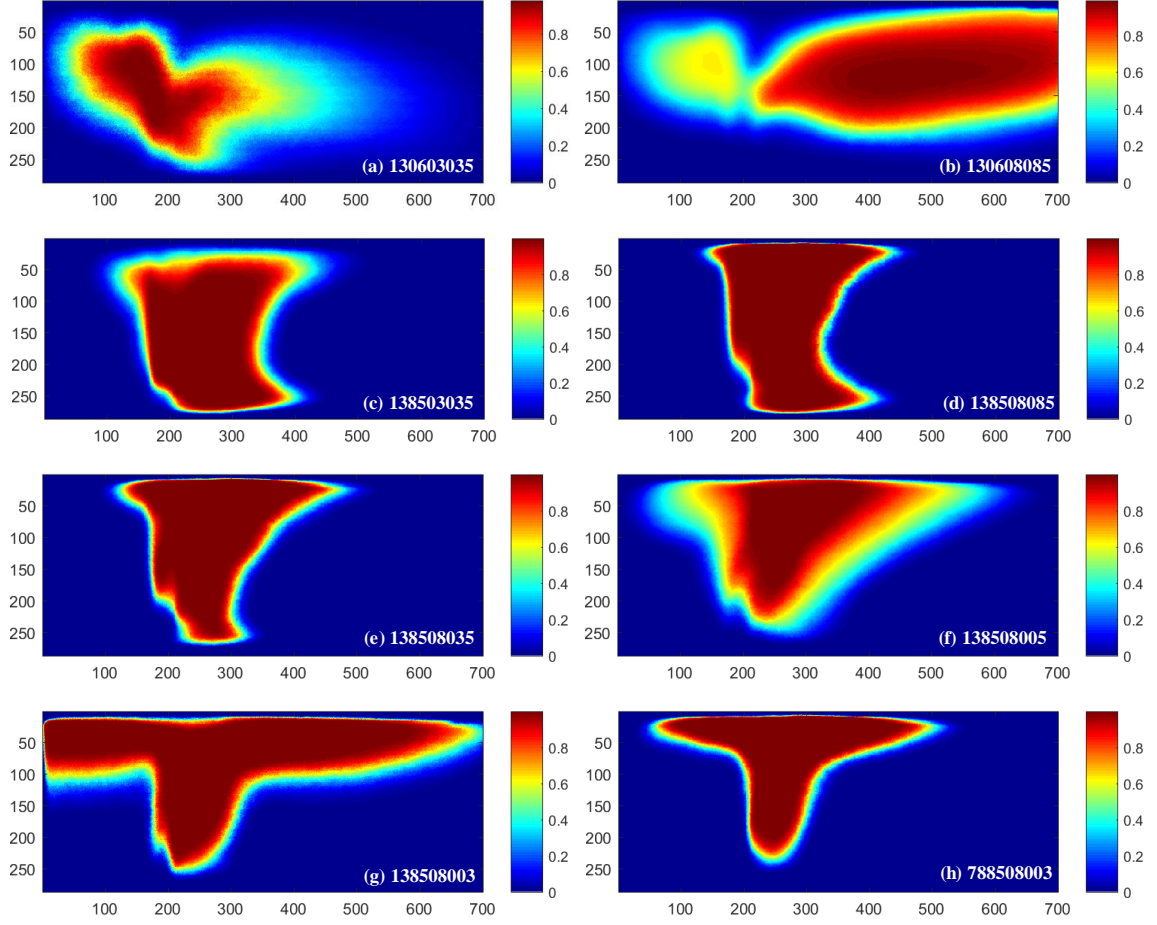
Figure 5.5: Mean PDF of chemiluminescence intensity images for LQL CJICF with staggered 5 jets (a-f) and parallel 3 jets (g, h), split = 1.3 (a-g) and 0.78 (h), ϕ_p = 0.6 (a, b) and 0.85 (c-h). (a) $\phi_{bj} = \phi_{tj} = 0.3$ (b) $\phi_{bj} = \phi_{tj} = 0.8$, (c) $\phi_{bj} = \phi_{tj} = 0.3$, (d) $\phi_{bj} = \phi_{tj} = 0.8$, (e) $\phi_{bj} = 0.8$, $\phi_{tj} = 0.3$, (f) $\phi_{bj} = 0.8$, $\phi_{tj} = 0$, (g, h) $\phi_{bj} = 0.8$.
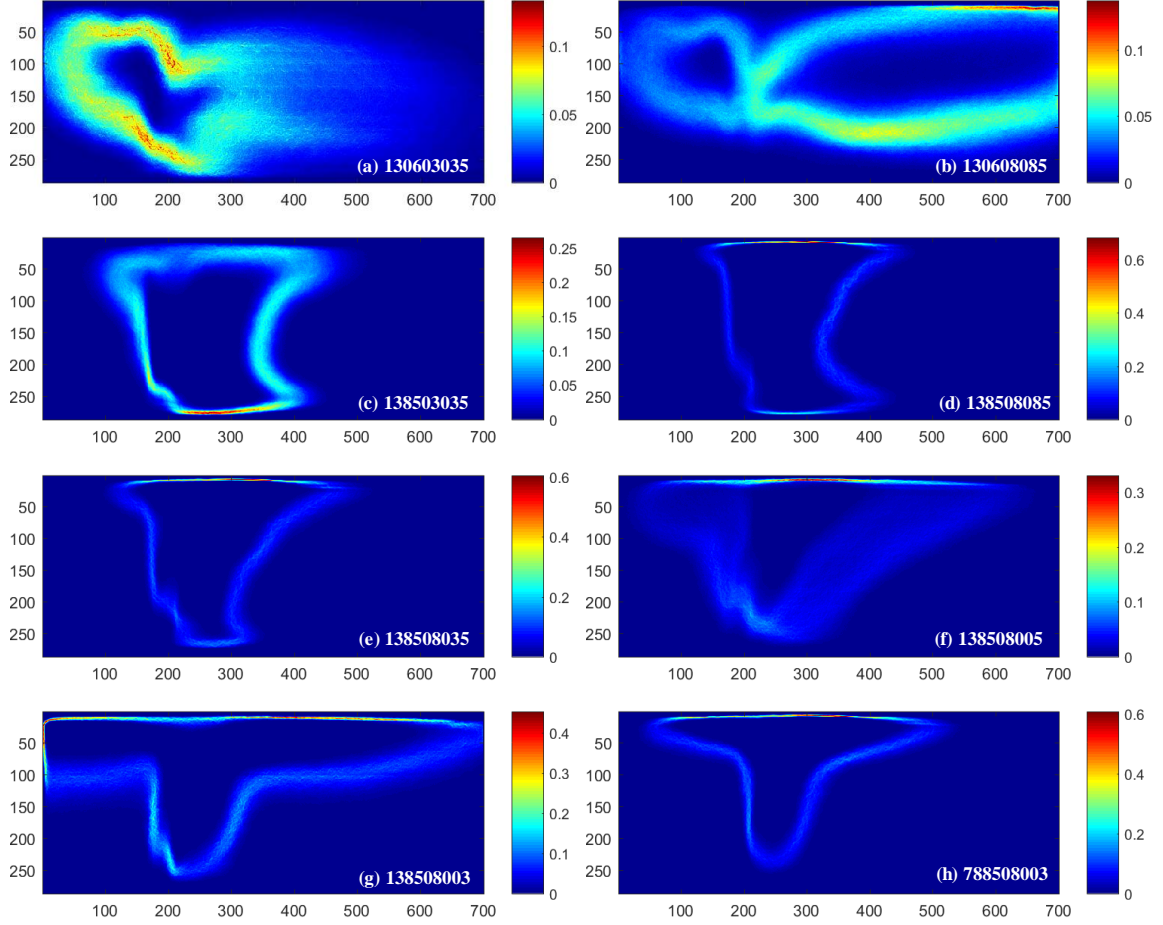
Figure 5.6: Averaged edges of instantaneous chemiluminescence intensity images for LQL CJICF with staggered 5 jets (a-f) and parallel 3 jets (g, h), split = 1.3 (a-g) and 0. 78 (h), ϕ_p = 0.6 (a, b) and 0.85 (c-h). (a) $\phi_{bj} = \phi_{tj}$ = 0.3 (b) $\phi_{bj} = \phi_{tj}$ = 0.8, (c) $\phi_{bj} = \phi_{tj}$ = 0.3, (d) $\phi_{bj} = \phi_{tj}$ = 0.8, (e) ϕ_{bj} = 0.8, ϕ_{tj} = 0.3, (f) ϕ_{bj} = 0.8, ϕ_{tj} =0, (g, h) ϕ_{bj} = 0.8. Note the different color map scaling for each result.

Lastly, we examine LQL with a parallel CJICF configuration, as seen in the results of Figure 5.1-Figure 5.6 (g, h). Firstly, the flame shape for parallel jets at LQL conditions is completely different than the RQL parallel jets results of Figure 4.7 (c, d). In the LQL cases the flame exists in the large recirculation zones created by the impinging parallel jets that were revealed in the velocity fields (Figure 3.6 (c-f)). Conversely, for RQL conditions there is no heat release in the recirculation and splash zones. Unlike the RQL air jets, the LQL jets already contain (premixed) fuel and do not rely on mixing with the crossflow

fluid to burn. Comparing the different air split cases shown in Figure 5.5 and Figure 5.6 (g, h), the upstream recirculation is smaller for the higher air split as seen through the larger flame extent for higher air split LQL case. This is consistent with the non-reacting velocity results in Figure 3.6 and Figure 3.11 (c-f).

CHAPTER 6.   CONCLUSIONS AND RECOMMENDATIONS

Staged combustors primarily rely upon rapid mixing and combustion to produce low emission levels. The jet in crossflow (JICF) is one configuration that can provide such rapid mixing and is used extensively in staged combustors for that reason. Most of the previous research in the open literature has examined the characteristics of single, unconfined JICF, but little work, especially experiments employing detailed diagnostics, has been carried out to understand the multiple and confined JICF (CJICF) configuration, which is a more practical scenario. This is the first major experimental study of multiple CJICF employing detailed optical diagnostics techniques, primarily high-speed SPIV and chemiluminescence. Both reacting and non-reacting CJICF are explored at atmospheric pressure and high temperature conditions. The primary contribution of this thesis is the elucidation of the mixing, velocity field and combustion characteristics of CJICF in air-staged (Rich-Quench-Lean, RQL) and fuel-air-staged (Lean-Quench-Lean, LQL) configurations.

Previous studies investigated the mixing characteristics and jet interactions of single- and multiple-row jets (in stream wise direction) using smoke photography. This thesis compliments and expands that work with mixing results obtained with high resolution, time-resolved planar particle scattering. Two jet configurations were addressed in this thesis, namely, parallel and staggered–opposed jets with relevant geometries and flow conditions. Moreover, time-resolved velocity fields were measured in various important planes across the multiple jet array. The combustion characteristics, such as the extent of burning and flame stabilization regions in both RQL and LQL configurations,

were determined using high-speed, line-of-sight chemiluminescence imaging, which provide important insights beyond those obtained in single JICF studies. Finally, the impact of the mixing and velocity fields in the confined, staged combustors on the combustion characteristics was detailed.

6.1   Conclusions

6.1.1   Major Findings

One can define a CJICF when the jet momentum ratio, *J*, is large enough for a given geometry to produce jet-wall interactions. The jet-wall interaction occurs as the jets impinge onto the opposite wall. While *J* is typically considered the controlling parameter for unconfined, single JICF, how the overall (air) mass is split between the jets and crossflow (i.e., pilot combustion zone) is found here to be more important for CJICF.

Rapid mixing in CJICF flowfields is found to result from a combination of jet-wall, jet-jet and, to a lesser extent, the traditional jet-crossflow interactions. Among these, the jet-wall interaction is found to be the most influential, and it produces multiple effects. One, the wall is able to redirect the jet fluid in the lateral direction; this enhances mixing with the crossflow in the region between jets and allows jet fluid to travel upstream. Two, the stagnation of the jet on the wall produces a recirculation region that provides a high residence time for chemical reactions. Three, the blockage caused by the high pressure stagnation region redirects the crossflow toward the wall opposite the stagnation region. This can change the local momentum ratio at the base of the jet, influence flame stabilization, and enhance mixing.

Jet configuration is another influential parameter to consider. In the two-sided, staggered-opposed configuration, as opposed to the one-sided parallel case, significant jet-jet interactions also occur. The high shear between the counter-flowing jets causes large and frequent lateral motion, and rapidly produces large scale structures that likely enhances mixing. Furthermore for better radial and circumferential uniformity in an annular combustor, e.g., for improving pattern factor, the results presented here indicate staggered jets would require less downstream distance to achieve the same uniformity than parallel jets for the same air(mass)-split.

The CJICF flow features greatly influence the combustion characteristics of both RQL and LQL staged combustors. For reasonably high pilot zone temperatures, the RQL staged combustion zone is primarily mixing limited, and thus highly dependent on the mixing field. The reactants in the LQL jets, on the other hand, do not need to mix with the crossflow in order for combustion to occur if the jet equivalence ratio is flammable. This is evident with the noticeable burning in the splash zone for LQL cases; for the same region in the RQL cases, little combustion occurred because the stagnation region contains mostly jet air and little fuel (from the crossflow). Furthermore, the compactness of the RQL combustion zone was shown to correlate with the length required to mix the jets with the crossflow and with the amount of unburned fuel in the pilot. For the LQL results, the compactness depended more on how long it takes to consume the available premixed fuel; thus jets with equivalence ratios closer to one were found to produce more compact combustion zones that leaner jets.

However, mixing with the crossflow can aid flame stabilization in the LQL case, for example through autoignition. While both RQL and LQL results showed attached

flames on the leeward side of the jets, the windward flame in the LQL cases is lifted more

than for RQL. In the current study, this is due to the slower chemistry for the CH_4 fuel in

the LQL jets compared to the H_2/CO reactants in the RQL rich pilot products. Stabilization

of the jet flames can also be influenced by the change in the crossflow approach the jets

due to the CJICF features mentioned above. For one, the crossflow fluid can contain a

mixture of the pilot products and recirculated jet fluid, which may be reacted or unreacted.

Thus the local crossflow can be hotter or colder than the pilot, leading to enhanced or

reduced flame stabilization. Also, the crossflow velocity can be increased or decreased due

to the redirection of the upstream crossflow, which would effect local strain rates.

6.1.2 *Additional Findings*

The general conclusions mentioned above are presented here in more detail, along

with additional observations from this study. The flow field and mixing characteristics of

multiple CJICF configuration are found to be significantly different than that of the single

unconfined JICF. The importance of jet-wall, jet-jet and jet-crossflow interactions are

examined, and their importance to attain rapid mixing in examined. At low air split and *J*

(12) ratio, the jet-crossflow interaction dominates the flowfield; the jet's vertical

momentum is turned by the crossflow's horizontal momentum before the jets hit the

opposite wall. At medium *J* (30), jet-jet interaction is present for the staggered jets

configuration; the jet momentum is sufficiently high such that it penetrates far enough to

effect the flowfield of the opposite jet. At high *J* (75), the jet-wall interaction is important;

the jets impinge onto the opposite wall, creating a high pressure "splash" or recirculation

zone. This splash zone imposes a blockage on the crossflow and causing it to divert away

from the wall far upstream of the jet injection location. This configuration is of importance

in a practical combustor where the upstream pilot flow could be diverted towards one of the liner walls away from the jet impingement region.

To quantify mixing, two uniformity metrics (U_{sym} and U_{rms}) are defined where U_{sym} measures top-bottom symmetry and U_{rms} measures the downstream mixing. For combustor applications, U_{sym} relates with the pattern factor while U_{rms} relates with the combustor length. The uniformity metrics for parallel and staggered jet configurations for a range of J ratios are presented in this thesis. The mixing results suggest that generally across all three planes, the flow becomes more uniform moving downstream. For the low J case ($J = 12$), the jet turns rapidly and mostly stays near the bottom half of the test section height. For the parallel jets with medium J (30), the jet fluid penetrates towards the bottom wall before turning, and then stays partly in the bottom half of the test section.

For the staggered-opposed configuration, the low J (12) and high J (75) cases provide better top-bottom uniformity in the downstream regions when compared to the medium J (30) case. Across the three planes, the staggered five jets with highest J provide the best overall mixing due to jet-jet and jet-wall interactions. Downstream of the jets, the crossflow can rapidly mix with jet fluid, which is even more noticeable in the regions between the jets due to lateral movement of jet fluid as it is redirected near the wall stagnation zone. The jet-wall impact appears to be more influenced by the total mass injection (or air split ratio in this study) rather than the momentum flux ratio, which is the parameter considered most influential for single, unconfined JICF configurations.

In RQL conditions, with the high temperature crossflow containing H_2 and CO, chemical times (autoignition delays) are sufficiently fast (~1-100μs), such that flames are

stabilized near the jet exits. The flame extents in RQL cases last only ~4-6 d_j which is also the distance required for mixing to occur for similar air split conditions as shown by the uniformity metrics. This indicates that the RQL flames are mixing limited rather than chemistry limited. Comparison of one sided (parallel) vs two sided (staggered) jets in RQL for same air split suggest that for parallel jets, the upstream recirculation region is much larger where no heat release occurs due the presence of mostly jet air. In staggered jets RQL, the upstream recirculation is much smaller and flame does exist since the opposite jets entrains the crossflow as well. At richer ϕ_p in RQL case, since $T_{ad,\,p}$ is lowered, τ_{auto} increases thereby causing lifted flames on the windward side of the jets. The flame on the leeward side consistently stays attached.

Contrary to the RQL, the LQL jet fluid can burn without significant mixing with the crossflow fluid, though a sufficiently high temperature crossflow can lead to enhanced flame stabilization. Thus when stabilized in a high temperature crossflow, the LQL jets can burn in the opposed wall splash region, while the RQL burning is delayed until mixing with the crossflow occurs. The heat release in the splash zone for LQL can further divert the crossflow due to dilatation. In a practical combustor, the flow from the pilot burner could be diverted due to high pressure splash region of the jet fluid, and even more diverted if there is heat release in the splash as in LQL case. As jets for fueled more in the LQL case, a more compact flame is achieved and in fact very weak flame exists if the jets have little amount of fuel as seen by cases with $\phi_j = 0.3$, and incomplete burning is noticed for this case when ϕ_p is lowered from 0.85 to 0.6. For the $\phi_p = 0.6$, even the jets with $\phi_j = 0.8$ burn inefficiently, or that the flame extends far in the downstream. In other words, the high adiabatic temperature from the crossflow is necessary to stabilize the premixed jets.

6.2   Recommendations for Future Work

An extensive data set of non-reacting CJICF velocity fields is provided in this thesis however conducting measurements of the reacting CJICF flowfield was not feasible due to the given geometry of the test section, exhaust section and due to limited optical access. It is recommended to design an improved facility with better optical access to take velocity data in reacting flows. Within the limitations of non-reacting PIV capabilities, flow field in additional planes such as x-y and y-z planes would be helpful which would be easy to incorporate if the test section had optical access from both the side windows instead of one window in the presented work.

Additional sets of conditions for LQL cases would be helpful where the pilot and jet equivalence ratios were chosen such that their adiabatic flame temperatures were not similar. By doing so, the effect of heat release in the far field combustion of one side jets could be seen on the flame stabilization in the near field of the opposite side jets. Planar flame diagnostics techniques such as OH PLIF are recommended in order to overcome the limitations imposed by the line-of-sight spatial averaging techniques such as chemiluminescence that was used in this study. If possible, simultaneous PIV and OH PLIF could provide insight into heat release effects on the flowfield. Additional studies on flame stabilization mechanisms are also recommended where data could be taken for different fuel types and other timescales such as consumption speed based timescales could be studied which would encapsulate chemical as well as fluid dynamical properties as opposed to autoignition timescales which is primarily a chemistry based time scale.

Further studies could also be performed at high pressure conditions to see the effect of pressure on flow and chemical time scales. At atmospheric pressure, more reactive fuel types such as H_2/CH_4 mixtures could be used instead of pure natural gas to resemble fast reaction times which might be present at high pressure, high temperature engine conditions with liquid fuels.

The experimental velocity data provided in this thesis could be a great tool for future computational modeling studies where the inlet conditions can be used from the data provided to validate different computational models. Further data analysis of current data is highly recommended where instantaneous statistics such as instantaneous PDFs based on velocity magnitudes and directionality can be performed. Temporal statistics identifying any underlying periodic behavior of the vortex shedding or movement should be examined in future. The velocities in z-direction and the dynamics of vortical structures in the velocity data were not extensively studied which could be pursued by other researchers to understand three-dimensional and dynamical behavior of CJICF. An extensive parametric study of quantities such as air split ratio and J ratio and possibly varying hole spacing and diameters is also recommended where confinement effects could be quantified and empirical scaling laws could be made.

APPENDIX A.INSTRUMENTATION

Table A.1: List of thermocouples used in CJICF experiments.

No.	Name	Name	Location	DAQ	DAQ port	Model	Manufacturer
1	T101	E1.9213.8-09	Pilot air SCO	NI9213	9	K	Omega (Type K)
2	T102	E1.9213.8-10	Combustor Inlet	NI9213	10	K	Omega (Type K)
3	T103	E1.9213.8-04	Combustor Nozzle	NI9213	4	K	Omega (Type K)
4	T104	Absent	Exhaust pipe	NI9213	NA	K	Omega (Type K)
5	T105	E1.9213.8-07	Pilot fuel CO	NI9213	7	K	Omega (Type K)
6	T201	E1.9213.8-05	Bottom air SCO	NI9213	5	K	Omega (Type K)
7	T202	E1.9213.8-13	Bottom plenum	NI9213	13	K	Omega (Type K)
8	T203	E1.9213.8-06	Bottom fuel CO	NI9213	6	K	Omega (Type K)
9	T301	E1.9213.8-00	Top Air SCO	NI9213	0	K	Omega (Type K)
10	T302	E1.9213.8-12	Top plenum	NI9213	12	K	Omega (Type K)
11	T303	E1.9213.8-08	Top fuel CO	NI9213	8	K	Omega (Type K)
12	T401	E1.9213.8-11	Test section	NI9213	11	R	Omega (Type K)

Table A.2: List of Solenoid valves used in CJICF experiments.

No.	Name	Location	Input Range	Output Range	DAQ	DAQ port	Model
1	SV1	Pilot fuel injector	120 VAC	Open/close	NI9476	A027	ASCO
2	SV2	Bottom fuel injector	120 VAC	Open/close	NI9476	A028	ASCO
3	SV3	Top fuel injector	120 VAC	Open/close	NI9476	A029	ASCO
4	SV4	Ignitor	120 VAC	Open/close	NI9476	A026	ASCO
4	SV5	H2 Solenoids (2)	120 VAC	Open/close	NI9476	A026	ASCO

Table A.3: List of differential pressure transducers used in CJICF experiments.

No.	Name	Name	Location	Input Range	Output Range	DAQ	DAQ port	Polarity	Model	Manufacturer
1	DP101	R2.9205.1-02/51	Pilot air SCO dP	1-5 VDC	0-10 psi	NI9205	Com2	Negative	PX771A-025DI	Omega
						NI9205	AI2/Port51	Signal		
2	DP201	E1.9208.4-01/02	Bottom air SCO dP	4-20 MA	0-100 inH2O	24 VDC	AI21	Positive	1151DP4S22B1DF	Rosemount
						NI9208	AI1 (port 2)	Negative		
3	DP301	E1.9208.4-00/01	Top air SCO dP	4-20 MA	0-100 inH2O	24 VDC	AI20	Positive	1151DP4S22B1DF	Rosemount
						NI9208	AI0 (port 1)	Negative		
4	DP401	R2.9205.1-04/55	Cooling air SCO dP	1-5 VDC	0-100 inH2O	NI9205	Com3	Negative	PX771A-100WCDI	Omega
						NI9205	AI4/Port55	Signal		

Table A.4: List of static pressure transducers used in CJICF experiments.

No.	Name	Name	Location	Input Range	Output Range	DAQ	DAQ port	Polarity	Model	Manufacturer
1	P101	R2.9205.1-01/49	Pilot air SCO P	1-5 VDC	0-1000 Psig	NI9205	COM1	Negative	PX725A-1KGI	Omega
						NI9205	ACH1	Signal		
2	P102	R2.9203.3-07/08	Pilot fuel C.O. upstream	4-20 MA	0-1000 Psig	NI9203	AO7/Terminal	Signal	PX409-1.0KGI	Omega
3	P103	R2.9205.1-22/75	Pilot fuel C.O. downstream	0-5VDC	0-200 Psig	24 VDC	rail	Positive	PX309-200G5V	Omega
						24 VDC	rail	Negative		
						NI9205	ACH22	Signal		
4	P104	R2.9205.1-23/77	Pre pilot regulator fuel P (Wall P)	0-5 VDC	0-1000 Psig	24 VDC	rail	Positive	PX309-1KG5V	Omega
						24 VDC	rail	Negative		
						NI9205	ACH23	Signal		
5	P105	R2.9205.1-00/47	Pilot combustor inlet P	1-5 VDC	0-500 Psig	NI9205	Com0	Negative	PX181B-500G5V	Omega
						NI9205	ACH0	Signal		
6	P201	E1.9205.2-18	Bottom air SCO P	0-5 V	0-500 Psig	24 VDC	E1.9208.4-27	Positive	PX309-500G5V	Omega
						COM	E1.9208.4-09	Negative		
						NI9205	AI1	Signal		
7	P202	R1.9203.3-00	Bottom fuel C.O. upstream P	4-20 MA	0-2500 Psig	NI9203	AI0	Negative	PX409-2.5KGI	Omega
						COM	rail	COM		
						Ground	rail	Ground		
8	P203	R2.9205.1-20/71	Bottom fuel C.O. downstream P	0-5 V	0-200 Psig	24 VDC	rail	Positive	PX309-200G5V	Omega
						24 VDC	rail	Negative		
						NI9205	ACH20	Signal		
9	P301	E1.9205.2-20	Top air SCO P	0-5 V	0-500 Psig	24 VDC	E1.9208.4-33	Positive	PX309-500G5V	Omega
						COM	E1.9208.4-28	Negative		
						NI9205	AI0	Signal		
10	P302	R1.9203.3-01	Top fuel C.O. upstream P	4-20 MA	0-2500 Psig	NI9203	AI1	Negative	PX409-2.5KGI	Omega
						COM	rail	COM		
						Ground	rail	Ground		
11	P303	R2.9205.1-21/73	Top fuel C.O. downstream P	0-5 V	0-200 Psig	24 VDC	rail	Positive	PX309-200G5V	Omega
						24 VDC	rail	Negative		
						NI9205	ACH21	Signal		
12	P401	R2.9205.1-5/56	Cooling air static P	1-5 VDC	0-500 Psig	NI9205	COM4	Negative	PX181B-500G5V	Omega
						NI9205	ACH4 to AI12/F	Signal		

Table A.5: List of pressure regulators used in CJICF experiments.

No.	Name	Name	Location	DAQ
1	Building air	--	Building air supply	NI9265
2	Pilot	R2.9265.4-02/87	Pilot CO Fuel Regulator set point	NI9265
3	Bottom (1)	R1.9265.2-00	Bottom CO Fuel Regulator set point	NI9265
4	Top (2)	R1.9265.2-01	Top CO Fuel Regulator set point	NI9265
5	Pilot Air	R1.9265.1-03	Pilot air setpoint	NI9265

Table A.6: List of subcritical and critical orifices used for flow metering.

No.	Name	Location	Model	Diameter (inches)	Manufacturer
1	SCO101	Pilot air SCO	2" 600# 304SS (360"WC,1.00 PPS)	1.0863	Imperial
2	SCO201	Bottom air SCO	2" 150# 316LSS	1.4341	Imperial
3	SCO301	Top air SCO	2" 150# 316LSS	1.2064	Imperial
4	CO101	Pilot fuel CO	V-43-SS	0.026	O'Keefe
5	CO201	Bottom fuel CO	V-26-SS	0.017	O'Keefe
6	CO301	Top fuel CO	V-21-SS	0.013	O'Keefe

Table A.7: List of calibration constants used in LabVIEW for fuel flow rate.

No.	Name	Location	Dia (inch)	CD	m	b	Calibration Date
1	CO101	Pilot fuel CO	0.043	0.91487	2.52591E-08	7.9E-06	Shephard 10/5/2015
2	CO201	Bottom fuel CO	0.026	0.92185	9.29278E-09	-2E-05	Jain 1/27/2016
3	CO301	Top fuel CO	0.021	0.94455	6.21158E-09	4.7E-06	Steinber 8/24/2015

Table A.8: Fuel flow rate calibration data obtained for critical (chocked) orifices.

P0 (Psi)	Fuel flow rate (g/s)		
	Pilot	Bottom	Top
100	1.02	0.35	0.25
150	1.52	0.54	0.38
200	2.03	0.73	0.50
250	2.53	0.91	0.62
300	3.03	1.10	0.75
250	2.53	0.91	0.62
400	4.04	1.47	1.00
500	5.05	1.84	1.25
600	6.06	2.21	1.49
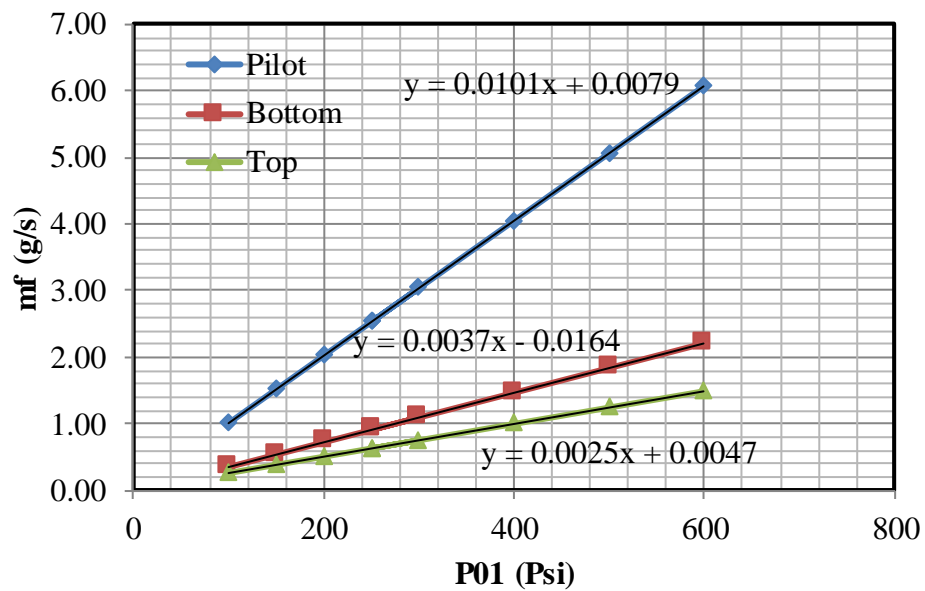
Figure A.1: Fuel flow rate calibration curves for critical orifices.

APPENDIX B. MIXING ANALYSIS CODE

```matlab
% Calculates Uniformity numbers for each image and an average image
from a video

% To run this script, put it the in the same folder that has the video
and choose matlab directory path to the same folder.
% Change the filename for the video you want to analyze
% Change the stringname accordingly
% Change the cropsize and ImDim depending upon a sample image for each
% calibration case. These dimensions are stored in Uniformity
Master.xls
% Change the excel file name and column names accordingly

% Last edited by Nishant Jain--- 2014-12-12----------------------------
-----------
%%
clear
clc
close all
A=VideoReader('V27550C1_512.avi');        %*****Input video file name
stringname = 'V27550C1_';
XlsColumn = 'AH1';                        %Input
B1,F1,J1,N1,R1,V1,Z1,AD1,etc..
cropsize = [12  39  1051-12 652-39];      %dimensions of cropped image
[xmin ymin width height] based on outer edge for M07555C1_1K
format = '.tif' ;
N=A.NumberOfFrames;                       %number of frames
h=A.Height;                               %height in pixels
w=A.Width;                                %width in pixels
mov(1:N)=struct('cdata',zeros(h,w,3,'uint8'),'colormap',[]);
Uniformity1_inst = zeros();
Imean = zeros();
%%
for k = 1:N                               %**********************choose
the range such that phi is constant and we have approximately 10 sec
worth of final video or we need 75 frames in total for each phi case
    mov(k).cdata=read(A,k)   ;        %reads RGB values in kth image
    mov(k).colormap=[]       ;        %reads colormap
    I = imcrop(mov(k).cdata,cropsize);
    w = size(I,2);
    h = size(I,1);
    ImDim = [184    299 1   1   1040    614 265 377 21  997 -30 662.0
120.0   85.0]; %[x0(jet center), y0(TS middle height) x1(frame x
origin) y1(frame y origin) x2(frame x end) y2(frame y end) x10mm(pixel)
y10mm(pixel)] These numbers come from uncropped calibrated image from
Davis
    xRes = (ImDim(10)-ImDim(9))/ImDim(13) ;%pixel/mm calculated from
biggest lengths available from Davis
    % xRes=5.83475;     % camera scale from davis
    yRes = (ImDim(12)-ImDim(11))/ImDim(14) ;%pixel/mm
    % xRes = 8.4;       %resolution found from the calibration sheet
image from Davis
```

```matlab
    % yRes = 8.4;        %resolution found from the calibration sheet
image from Davis
    dj = 0.5*25.4*xRes ;
    xjetwin = ImDim(1)-dj/2;
    xjetlee = ImDim(1)+dj/2;
    Nstrips = floor((w-xjetwin)/dj);
    dNorm = 0:1:Nstrips-1;
    Imean = Imean + 1/N.*im2double(I);
    %% Calculate location of vertical lines/strips and instantaneous
uniformity# using two methods

    for i = 1:Nstrips
        verline = xjetwin + (i-1)*dj;
        Itop =
sum(sum(I(1:round(h/2),round(verline):round(verline+dj))));
        Ibot =
sum(sum(I(round(h/2):h,round(verline):round(verline+dj))));
        Uniformity1_inst(i,k)= (Itop-Ibot)/(Itop+Ibot);
        Uniformity2_inst(i,k) =
std2(I(:,round(verline):round(verline+dj)))./mean2(I(:,round(verline):r
ound(verline+dj)));

    end

end
%% Calculate location of vertical lines/strips and mean uniformity#
using two methods using mean image
% Method 1/U1 : using relative intensity of top and bottom half of each
strip
% Method 2/U2 : coefficient of variation (stdev/mean) of each strip
for i = 1:Nstrips
%        verline = xjetwin + (i-1)*dj;
%        Itop_mean =
sum(sum(Imean(1:round(h/2),round(verline):round(verline+dj))));
%        Ibot_mean =
sum(sum(Imean(round(h/2):h,round(verline):round(verline+dj))));
%        Uniformity1_mean(i) = (Itop_mean-
Ibot_mean)/(Itop_mean+Ibot_mean);
%        Uniformity2_mean(i) =
std2(Imean(:,round(verline):round(verline+dj)))./mean2(Imean(:,round(ve
rline):round(verline+dj)));

%  Calculate mean uniformity# using the instantaneous images (U#1 mean
does
%  not change but U#2 does change, since average of stdev is not same
as
%  stdev of average. so DO NOT use mean image.
        Uniformity1_mean(i) = mean(Uniformity1_inst(i,:));
        Uniformity2_mean(i) = mean(Uniformity2_inst(i,:));
        Uniformity1_stdev(i)= std(Uniformity1_inst(i,:));
        Uniformity2_stdev(i)= std(Uniformity2_inst(i,:));

end
```

```matlab
%% Write Uniformity# to excel file
dNormCell = ['Normalized distance (x/dj)', num2cell(dNorm)]';
U_meanCell = [strcat(stringname,'Mean
uniformity1'),num2cell(Uniformity1_mean);...
    strcat(stringname,'Mean uniformity2'),num2cell(Uniformity2_mean)
    strcat(stringname,'Stdev uniformity1'),num2cell(Uniformity1_stdev)
      strcat(stringname,'Stdev
uniformity2'),num2cell(Uniformity2_stdev)]';
xlswrite('Mixing uniformity P2K1',dNormCell,'U_Mean','A1');
xlswrite('Mixing uniformity P2K1',U_meanCell,'U_Mean',XlsColumn);
xlswrite('Mixing uniformity
P2K1',Uniformity1_inst,strcat(stringname,'U1_Inst'));
xlswrite('Mixing uniformity
P2K1',Uniformity2_inst,strcat(stringname,'U2_Inst'));

%% Plot and save last cropped frame in the video with vertical
lines/strips
figure(1)
imshow(I);
% set(figure(1),'units','inches','pos',[1 5 w/xRes/25.4 h/yRes/25.4]);
% set(gca,'position',[0 0 1 1],'units','inches')
hold on;
line(ImDim(1),1:h,'LineWidth',20,'Color','r','LineStyle','-');
line(1:w,h/2,'LineWidth',20,'Color','r');
line(xjetwin,1:h,'LineWidth',10,'Color','g');
line(xjetlee,1:h,'LineWidth',10,'Color','g');

for i = 1:Nstrips
    verline = xjetlee + i*dj;
    line(verline,1:h,'LineWidth',10,'Color','g');
end
frame = getframe;
imwrite(frame.cdata,strcat(stringname,int2str(N),'_1',format));

%% Plot & save mean cropped image of the entire video
figure(2)
imshow(Imean);
% set(figure(2),'units','inches','pos',[6 5 w/xRes/25.4 h/yRes/25.4]);
% set(gca,'position',[0 0 1 1],'units','normalized')
frame = getframe;
imwrite(frame.cdata,strcat(stringname,'mean',format));

%% Plot and save Uniformity#1 for all instantaneous images
figure(3);
hold on
set(figure(3),'units','inches','pos',[2 2 4 3]);
plot(dNorm,Uniformity1_inst,'+','MarkerSize',3)
xlabel('x/d_j');
ylabel('Instantaneous Uniformity#1');
a=findobj(gcf); % get the handles associated with the current figure
allaxes=findall(a,'Type','axes');
alllines=findall(a,'Type','line');
alltext=findall(a,'Type','text');
set(allaxes,'FontName','Times','FontWeight','Bold','LineWidth',2,...
    'FontSize',16,'XMinorTick','on','YMinorTick','on','Box','on');
set(alllines,'Linewidth',1.5);
```

```matlab
set(alltext,'FontName','Times','FontWeight','Bold','FontSize',18);
saveas(gcf,strcat(stringname,'U1_inst',format));

%% Plot and save Uniformity#1 for mean image
figure(4);
hold on
set(figure(4),'units','inches','pos',[6 2 4 3]);
plot(dNorm,Uniformity1_mean,'k-
o','MarkerSize',5,'MarkerFaceColor','k','LineWIdth',1.5);
xlabel('x/d_j');
ylabel('Mean Uniformity#1');
a=findobj(gcf); % get the handles associated with the current figure
allaxes=findall(a,'Type','axes');
alllines=findall(a,'Type','line');
alltext=findall(a,'Type','text');
set(allaxes,'FontName','Times','FontWeight','Bold','LineWidth',2,...
    'FontSize',16,'XMinorTick','on','YMinorTick','on','Box','on');
set(alllines,'Linewidth',1.5);
set(alltext,'FontName','Times','FontWeight','Bold','FontSize',18);
saveas(gcf,strcat(stringname,'U1_mean',format));

%% Plot and save Uniformity#2 for all instantaneous images
figure(5);
hold on
set(figure(5),'units','inches','pos',[2 4 4 3]);
plot(dNorm,Uniformity2_inst,'+','MarkerSize',3)
xlabel('x/d_j');
ylabel('Instantaneous Uniformity#2');
a=findobj(gcf); % get the handles associated with the current figure
allaxes=findall(a,'Type','axes');
alllines=findall(a,'Type','line');
alltext=findall(a,'Type','text');
set(allaxes,'FontName','Times','FontWeight','Bold','LineWidth',2,...
    'FontSize',16,'XMinorTick','on','YMinorTick','on','Box','on');
set(alllines,'Linewidth',1.5);
set(alltext,'FontName','Times','FontWeight','Bold','FontSize',18);
saveas(gcf,strcat(stringname,'U2_inst',format));

%% Plot and save Uniformity#2 for mean image
figure(6);
hold on
set(figure(6),'units','inches','pos',[6 4 4 3]);
plot(dNorm,Uniformity2_mean,'k-
o','MarkerSize',5,'MarkerFaceColor','k','LineWIdth',1.5);
xlabel('x/d_j');
ylabel('Mean Uniformity#2');
a=findobj(gcf); % get the handles associated with the current figure
allaxes=findall(a,'Type','axes');
alllines=findall(a,'Type','line');
alltext=findall(a,'Type','text');
set(allaxes,'FontName','Times','FontWeight','Bold','LineWidth',2,...
    'FontSize',16,'XMinorTick','on','YMinorTick','on','Box','on');
set(alllines,'Linewidth',1.5);
set(alltext,'FontName','Times','FontWeight','Bold','FontSize',18);
saveas(gcf,strcat(stringname,'U2_mean',format));
```

147

```matlab
%%
figure(7);
hold on
set(figure(7),'units','inches','pos',[2 2 4 3]);
plot(dNorm,Uniformity1_inst,'+','MarkerSize',3)
plot(dNorm,Uniformity1_mean,'k-
o','MarkerSize',5,'MarkerFaceColor','k','LineWIdth',1.5);

xlabel('x/d_j');
ylabel('Uniformity#1');
a=findobj(gcf); % get the handles associated with the current figure
allaxes=findall(a,'Type','axes');
alllines=findall(a,'Type','line');
alltext=findall(a,'Type','text');
set(allaxes,'FontName','Times','FontWeight','Bold','LineWidth',2,...
    'FontSize',16,'XMinorTick','on','YMinorTick','on','Box','on');
set(alllines,'Linewidth',1.5);
set(alltext,'FontName','Times','FontWeight','Bold','FontSize',18);
saveas(gcf,strcat(stringname,'U1_inst_mean',format));


%%
%% Plot and save Uniformity#2 for all instantaneous images
figure(8);
hold on
set(figure(8),'units','inches','pos',[2 4 4 3]);
plot(dNorm,Uniformity2_inst,'+','MarkerSize',3)
plot(dNorm,Uniformity2_mean,'k-
o','MarkerSize',5,'MarkerFaceColor','k','LineWIdth',1.5);
xlabel('x/d_j');
ylabel('Uniformity#2');
a=findobj(gcf); % get the handles associated with the current figure
allaxes=findall(a,'Type','axes');
alllines=findall(a,'Type','line');
alltext=findall(a,'Type','text');
set(allaxes,'FontName','Times','FontWeight','Bold','LineWidth',2,...
    'FontSize',16,'XMinorTick','on','YMinorTick','on','Box','on');
set(alllines,'Linewidth',1.5);
set(alltext,'FontName','Times','FontWeight','Bold','FontSize',18);
saveas(gcf,strcat(stringname,'U2_inst_mean',format));
```

APPENDIX C. SPIV IMAGE PREPROCESSING CODE

```
:: Converts 4 single Tiff
SETLOCAL EnableDelayedExpansion
@echo off

:: ***********************************************Change these
parameters*******************************************
:: Define input and output paths of images
SET
file_path_in1=I:\njain34\2016PJICFRawData\201602SPIVRawData\C1_Njain\C1
V21322\
SET
file_path_in2=I:\njain34\2016PJICFRawData\201602SPIVRawData\C2_Njain\C2
V21322\
SET
file_path_out=I:\njain34\2016PJICFRawData\201602SPIVRawData\SPIV_NJain\
V21322\
SET filename_out=V21322_
SET firstImage=1
:: Note that here I programmed firstImage like a boolean logical, if 1
then yes use first image, else 0 then first image pair starts with
second image


:: *******************************************Don't mess with this
programming*************************************
:: Make the output path if it does not exist
if not exist "!file_path_out!" mkdir "!file_path_out!"

:: Initialize loop variables
SET count_im=0
SET count_out=0
SET count_display=0

:: Loop through the images in the first directory
FOR %%G IN ("%file_path_in1%*.tif") DO (
SET /a count_im=!count_im!+1
SET /a count_display=!count_display!+1
if "!count_display!" EQU "50" (echo Image !count_im! && SET
count_display=0)
:: echo !firstImage!
SET c1b=%%G
SET c2b=!c1b:c1=c2!
if "!firstImage!" EQU "0" (
if "!count_im!" NEQ "1" (
SET /a count_out=!count_out!+1
SET "x=00000!count_out!"
SET x=!x:~-5!
SET cout="!file_path_out!!filename_out!!x!.tif"
:: echo !cout!
convert.exe "!c1a!" %%G "!c2a!" "!c2b!" -adjoin "!cout!"
)
```

```
SET firstImage=1
) ELSE (
SET firstImage=0
SET c1a=%%G
SET c2a=!c2b!
)
)
echo Finished

pause
```

APPENDIX D. FLAME IMAGE PROCESSING CODE

```matlab
clc;
clear all;
close all;
%% Input variables
FilePathIn = 'G:\njain34\2016PJICFRawData\20160205OHChemiRawData';
CaseName = '\131700005';
FilePathOut = 'G:\njain34\2018ProcessedData\OHChemi\test_100';

ImageAmp = 1;
nStart = 3;                         %start image number
nEnd = 102;                         %end image number%
ThreshFactor = 0.5;                      %set threshold multiplication
factor for Otsu's threshold
CropRect = [54 130 753-54 416-130];    %set crop rectangle region


%% Initialization
FilePathIn = strcat(FilePathIn,CaseName);
FilePathOut = strcat(FilePathOut,CaseName);
FileName = strcat(FilePathOut,CaseName);
mkdir(FilePathOut);
V = VideoWriter(FileName,'Grayscale AVI');
V.FrameRate = 10;
open(V);
cd(FilePathIn)
I = dir('*.tif');                %matrix of all the images in the
directory
% nEnd = length(I);                    %choose number of images to make
the video
N = nEnd-nStart+1;               %Total number of images

MeanImage = zeros();             %Mean image, initialize parameter
PDFImage = zeros();
Edges = zeros();
% BinaryImageGrad = zeros();
% PDFImageGrad = zeros();
% PDFMultiImage = zeros();
% AddImage=zeros();               %Addition of all the images,Non-
dimensionalized based on , initialize parameter
TotInt=zeros();                  %Total intensity of an image summed
over all the rows and coloums
TotIntX = zeros();               %Total intensity of an image summed
over all the coloums (Y)
TotIntY = zeros();               %Total intensity of an image summed
over all the coloums (Y)
tic
for k = nStart:1:nEnd
    Image = imread(I(k).name);   %read images
    MaxInt = double(max(max(Image)));
    if MaxInt >= 65520
        fprintf('Warning: %s is saturated!\n',I(k).name)
```

```matlab
    end
%% calculate noise threshold based on outside the test section
intensity
%     Noise = Image;
%
Noise(CropRect(2):CropRect(2)+CropRect(4),CropRect(1):CropRect(1)+CropR
ect(3)) = 0;
%     Thresh = 2*double(max(max(Noise)))/MaxInt;
%%
    Image = im2double(imcrop(Image, CropRect));  % crop and non-
dimensionalize image wrt maximum
    MeanImage = MeanImage + 1/N.*Image;      %calculate Mean image
%   AddImage = AddImage+image;
%   TotInt(k)=sum(sum(image(k)));
    Threshold = graythresh(Image)*ThreshFactor;
%     Threshold = 0.05;
    BinaryImage =
bwareafilt(imfill(imbinarize(Image,Threshold),'holes'),1);
    BinaryImage = bwareafilt(BinaryImage,1);
    PDFImage = PDFImage + 1/N.*BinaryImage;

%     [gmag gdir] = imgradient(Image);
%     BinaryImageGrad = gmag/max(max(gmag))>0.25;
%     PDFImageGrad = PDFImageGrad + 1/N.*BinaryImageGrad;

    EdgeImage = edge(BinaryImage,'Canny');
    Edges = Edges + 1/N.*EdgeImage;
    if k < 100+nStart;
    frame = imfuse(Image,EdgeImage,'blend');
    writeVideo(V,frame);
    end
    %% calculate pdf based multiple threshold levels (doesnt make much
sense
    %%since equivalent to mean image if many threshholds are used)
%     Thresh = multithresh(Image,10);
%     QuantImage = imquantize(Image,Thresh);
%     PDFMultiImage = PDFMultiImage + 1/N.*QuantImage;

end
close(V);
TotIntX = sum(MeanImage);
TotIntY = sum(MeanImage');
MeanImage = im2uint16(MeanImage);
Image = im2uint16(Image);

save(FileName);
imwrite(Image, strcat(FileName,'InstGray.tif'));
imwrite(MeanImage, strcat(FileName, 'MeanGray.tif'));
imwrite(PDFImage, strcat(FileName,'PDFGray.tif'));
imwrite(Edges,strcat(FileName, 'EdgesGray.tif'));

figure(1);imagesc(MeanImage);colormap(jet);colorbar;axis image;
saveas(figure(1), strcat(FileName,'Mean'),'png');saveas(figure(1),
strcat(FileName,'Mean'),'fig');
figure(2);imagesc(PDFImage);colormap(jet);colorbar;axis image;
```

```matlab
saveas(figure(2), strcat(FileName,'PDF'),'png');saveas(figure(2),
strcat(FileName,'PDF'),'fig');
figure(3);imagesc(Edges);colormap(jet);colorbar;axis image;
saveas(figure(3), strcat(FileName,'Edges'),'png');saveas(figure(3),
strcat(FileName,'Edges'),'fig');
figure(4);imshowpair(Image,EdgeImage,'blend');colormap(gray);colorbar;
saveas(figure(4), strcat(FileName,'InstEdge'),'png');saveas(figure(4),
strcat(FileName,'InstEdge'),'fig');
figure(5);imcontour(MeanImage,10); colorbar
saveas(figure(5),
strcat(FileName,'MeanContour'),'png');saveas(figure(5),
strcat(FileName,'MeanContour'),'fig');
figure(6);imshowpair(MeanImage,Edges,'blend');colormap(gray);colorbar;
saveas(figure(6), strcat(FileName,'MeanEdge'),'png');saveas(figure(6),
strcat(FileName,'MeanEdge'),'fig');

% %% create filtered contour images
% D = imread('781300003MeanGray.tif');
% Df = imgaussfilt(D,2);
% figure;imagesc(D);colormap(jet);colorbar;axis image;
% figure;imcontour(Df,10);colormap(jet);colorbar;axis image;caxis([0
max(max(D))])
% cb=colorbar();set(cb, 'Ticks', [0:1000:4000], 'TickLabels', {'0',
'1000', '2000', '3000', '4000', '12000'}%
saveas(figure(2),'781300003MeanContourFilt.fig');saveas(figure(2),'7813
00003MeanContourFilt.png');
%
%%


%
% cb = colorbar();
% set(cb, 'Ticks', [10^7, 2.5*10^7, 5*10^7, 7.5*10^7, 10^8],
'TickLabels', {'10^7', '2.5 x 10^7', '5 x 10^7', '7.5 x 10^7', '10^8'},
'Interpreter', 'tex')




% figure(5);imshow(PDFImageGrad);colormap(jet);colorbar;
% figure(6);imshow(gmag,[]);colormap(gray);colorbar;
% AmplifiedMeanImage = ImageAmp*MeanImage;
%
figure(2);imshow(AmplifiedMeanImage,'Border','loose');colormap(jet);col
orbar;
% saveas(figure(2), strcat(FileName,'MeanAmp'),'png');saveas(figure(2),
strcat(FileName,'MeanAmp'),'fig');

toc



% figure(4);imagesc(PDFMultiImage);colormap(jet);colorbar;
%
% figure(2);imagesc(AddImage);colormap(gray);
% figure(4);plot(TotInt, '-k'); hold on; plot(TotIntX, '-r');
plot(TotIntY,'-b');
```

```matlab
% Imeanmean = mean(mean(MeanImage));
% Imeansum = sum(sum(MeanImage))/(512*768);
% Imeansum2 = mean(TotInt);


% max(max(MeanImage))



% code to avg tiff files in a folder

% close all
% clear all
%
% folder1 = 'D:\njain34\01_Gatech\01_RQL\Experiments and data\20170713
OH Chemi test\131300005_2';
% filepattern1 = fullfile(folder1,'*.tif');
% tiffiles1 = dir(filepattern1);
%
%  baseFileName1 = tiffiles1(1).name;
%   fullFileName1 = fullfile(folder1, baseFileName1);
%   totalimage = imread(fullFileName1);
%   totalimage_norm = imread(fullFileName1)./max(max(totalimage));
% for counter1 = 2:length(tiffiles1)
%    baseFileName1 = tiffiles1(counter1).name;
%   fullFileName1 = fullfile(folder1, baseFileName1);
%   fprintf(1, 'Now reading %s\n', fullFileName1);
%   imageArray = imread(fullFileName1);
%   imageArray_norm = imread(fullFileName1)./max(max(imageArray));
%   totalimage = imadd(totalimage,imageArray);
%    totalimage_norm = imadd(totalimage_norm,imageArray_norm);
% end
%
% Avgimage = totalimage/length(tiffiles1);
% Avgimage_norm = totalimage_norm/length(tiffiles1);
% figure(5)
% imagesc(Avgimage)
% figure(6)
% imagesc(Avgimage_norm)
%
```

APPENDIX E. AUTOIGNITION CALCULATION CODE

```matlab
clear
clc
close all

[GasData,GasHeaders,Case] = tblread('gas.txt','\t');
AirSplit = 1.3 ;

%% Set pilot equilibrium calculator conditions

FuelPilot = 'CH4'; %Choose : CH4, C3H8, C10H22
PhiPilot = 0.57; % Use two digit numbers...
PreheatPilot = 512 ; %[K]
PPilot = 1 ; %[atm]

MdotPilot = GasData(:,strmatch('Inlet flow rate of C1 Inlet1 Gas
MixerC1 end point_(kg/sec)',GasHeaders));
MdotPilot = MdotPilot*1000 ; %(g/s)
TPilot = GasData(:,strmatch('Inlet temperature of C1 Inlet1 Gas MixerC1
end point_(K)',GasHeaders)); %K (Input Temperature of Pilot Inlet)
PGas = GasData(:,strmatch('Pressure Gas MixerC1 end
point_(Pa)',GasHeaders));
PGas = PGas/101325 ;             %[atm]

%% Set jet inlet conditions
FuelJet1 = 'H2';              %Choose : H2, CH4, C3H8, C10H22, H2CH4-1090
etc..
FuelJet2 = 'CH4';
FuelJet1Perc = 25;           %Choose fuel mixture percentage
FuelJet2Perc = 100-FuelJet1Perc;
FuelJet = strcat(FuelJet1,FuelJet2,'-
',num2str(FuelJet1Perc),num2str(FuelJet2Perc));
PhiJet = GasData(:,strmatch('Inlet equivalence ratio of C1 Inlet2 Gas
MixerC1 end point',GasHeaders));              % Use two digit
numbers...
TJet = GasData(:,strmatch('Inlet temperature of C1 Inlet2 Gas MixerC1
end point_(K)',GasHeaders)); %[K]
TGasMix = GasData(:,strmatch('Temperature Gas MixerC1 end
point_(K)',GasHeaders)); %[K]
MdotJet100 = AirSplit*MdotPilot; %[g/s]
MdotJet = GasData(:,strmatch('Inlet flow rate of C1 Inlet2 Gas MixerC1
end point_(kg/sec)',GasHeaders));
MdotJet = MdotJet*1000 ; %g/s
MixFracJet = MdotJet./(MdotJet+MdotPilot);
PercJetMix = MdotJet./MdotJet100*100 ;

%% Define autoignition
%TauAuto_T : Based on percent rise in Temperature
TAutoPerc = 20 ; %Percentage rise in Temperature to define autoignition
time
ThresDelT = 50 ; %[K] If temperature rise is lesser than this threshold
then call it as no flame.
```

155

```matlab
%% Write to excel

FuelPilotVec = [];
FuelJet1Vec = [];
FuelJet2Vec = [];
FuelJet1PercVec = [];
FuelJet2PercVec = [];
PhiPilotVec = [];
% PhiJetVec = [];
PPilotVec = [];
% PGasVec = [];
% TPilotVec = [];
% TJetVec =[];
% MdotPilotVec = [];
% MdotJetVec = [];
% MixFracJetVec = [];
% PercJetMixVec = [];
TauAuto_TVec = [];
TauAuto_HVec = [];
TauAuto_HCOVec = [];
TVec = [];
Run = (1:size(GasData,1))';
OutVec2 = num2cell(NaN(1000,5*length(Run))); % For the overall plotting
vector


% Run = 1;
Name = strcat(FuelPilot,'-',FuelJet,'-P',
num2str(PPilot,'%02i'),num2str(PGas,'%02i'),...
    '-Phi',num2str(PhiPilot*100),num2str(PhiJet*100),'-
T',num2str(TPilot,'%04i'),...
    num2str(TJet,'%03i'),'-AS',num2str(AirSplit*10,'%02i'),'.xlsx');
for i = 1:length(Run)

    txtname = strcat(num2str(Run(i)),'.txt');
    [Data,Headers,Distance] = tblread(txtname,'\t');
    [x, y] = size(Data);
    Distance = str2num(Distance);
    TauRes = Data(:,strmatch('Plug flow residence time
PFRC2',Headers));
    T = Data(:,strmatch('Temperature PFRC2',Headers));
    XH = Data(:,strmatch('Mole fraction H PFRC2',Headers));
    XHCO = Data(:,strmatch('Mole fraction HCO PFRC2',Headers));

    if isempty(XH)
        XH = NaN(length(Distance),1) ;
        TauAuto_H = NaN ;
    else
        [MaxH AutoInd_H] = max(XH);
        TauAuto_H = TauRes(AutoInd_H);
    end

    if isempty(XHCO)
        XHCO = NaN(length(Distance),1) ;
```

```matlab
        TauAuto_HCO = NaN;
    else
        [MaxHCO AutoInd_HCO] = max(XHCO);
        TauAuto_HCO = TauRes(AutoInd_HCO);
    end

    delT = max(T)-min(T);
    if delT <= ThresDelT
        TauAuto_T = NaN;
        TauAuto_H = NaN;
        TauAuto_HCO = NaN;

    else
        TAuto = min(T)+delT*TAutoPerc/100;
        [Dif AutoInd_T] = min(abs(T-TAuto));
        if T(AutoInd_T)>TAuto;
            AutoIndLow_T = AutoInd_T-1;
        else
            AutoIndLow_T = AutoInd_T;
        end
        AutoIndHigh_T = AutoIndLow_T+1;
        TauAuto_T = TauRes(AutoIndLow_T)+(TauRes(AutoIndHigh_T)-
TauRes(AutoIndLow_T))/...
            (T(AutoIndHigh_T)-T(AutoIndLow_T))*(TAuto-T(AutoIndLow_T));

        if abs(TauAuto_H-TauAuto_T)/TauAuto_T >= 0.5
            TauAuto_H = NaN;
        end
        if abs(TauAuto_HCO-TauAuto_T)/TauAuto_T >= 0.5
            TauAuto_HCO = NaN;
        end

    end

%     delT = max(T)-min(T);
%     if delT <= ThresDelT
%         TauAuto_T = NaN;
%     else
%         TAuto = min(T)+delT*TAutoPerc/100;
%         [Dif AutoInd_T] = min(abs(T-TAuto));
%         if T(AutoInd_T)>TAuto;
%             AutoIndLow_T = AutoInd_T-1;
%         else
%             AutoIndLow_T = AutoInd_T;
%         end
%         AutoIndHigh_T = AutoIndLow_T+1;
%         TauAuto_T = TauRes(AutoIndLow_T)+(TauRes(AutoIndHigh_T)-
TauRes(AutoIndLow_T))/...
%             (T(AutoIndHigh_T)-T(AutoIndLow_T))*(TAuto-
T(AutoIndLow_T));
%     end
%     if delT <= ThresDelT
```

```matlab
%         TauAuto_H = NaN;
%     elseif isempty(XH)
%         TauAuto_H = NaN;
%     else
%         [MaxH AutoInd_H] = max(XH);
%         TauAuto_H = TauRes(AutoInd_H);
%     end
%      if delT <= ThresDelT
%         TauAuto_HCO = NaN;
%     elseif isempty(XHCO)
%         TauAuto_HCO = NaN;
%      else
%         [MaxHCO AutoInd_HCO] = max(XHCO);
%         TauAuto_HCO = TauRes(AutoInd_HCO);
%     end

%     NameVec = [NameVec cellstr(Name)];
    FuelPilotVec = [FuelPilotVec; cellstr(FuelPilot)];
    FuelJet1Vec = [FuelJet1Vec; cellstr(FuelJet1)];
    FuelJet2Vec = [FuelJet2Vec; cellstr(FuelJet2)];
    FuelJet1PercVec = [FuelJet1PercVec; num2cell(FuelJet1Perc)];
    FuelJet2PercVec = [FuelJet2PercVec; num2cell(FuelJet2Perc)];
    PhiPilotVec = [PhiPilotVec; num2cell(PhiPilot)];
%     PhiJetVec = [PhiJetVec num2cell(PhiJet)];
    PPilotVec = [PPilotVec; num2cell(PPilot)];
%     PGasVec = [PGasVec num2cell(PGas)];
%     TPilotVec = [TPilotVec num2cell(TPilot)];
%     TJetVec =[TJetVec num2cell(TJet)];
%     MdotPilotVec = [MdotPilotVec num2cell(MdotPilot)];
%     MdotJetVec = [MdotJetVec MdotJet];
%     MixFracJetVec = [MixFracJetVec MixFracJet];
% %     PercJetMixVec = [PercJetMixVec PercJetMix];
    TauAuto_TVec = [TauAuto_TVec; num2cell(TauAuto_T)];
    TauAuto_HVec = [TauAuto_HVec; num2cell(TauAuto_H)];
    TauAuto_HCOVec = [TauAuto_HCOVec; num2cell(TauAuto_HCO)];


    RunCell = ['Run number'; num2cell(Run)];
    NameCell = ['Filename'; cellstr(Name)];
    FuelPilotCell = ['Pilot fuel'; FuelPilotVec];
    FuelJet1Cell = ['Jet fuel 1'; FuelJet1Vec];
    FuelJet2Cell = ['Jet fuel 2'; FuelJet2Vec];
    FuelJet1PercCell = ['Jet fuel 1 %'; FuelJet1PercVec];
    FuelJet2PercCell = ['Jet fuel 2 %'; FuelJet2PercVec];
    PhiPilotCell = ['Pilot equivalence ratio'; PhiPilotVec];
    PhiJetCell = ['Jet equivalence ratio'; num2cell(PhiJet)];
    PPilotCell = ['Pilot pressure (atm)'; PPilotVec];
    PGasCell = ['PFR pressure (atm)'; num2cell(PGas)];
    TPilotCell = ['Pilot inlet temperature (K)'; num2cell(TPilot)];
    TJetCell =['Jet inlet temperature (K)'; num2cell(TJet)];
    TGasCell = ['Gas mixture temperature (K)'; num2cell(TGasMix)];
    MdotPilotCell = ['Pilot mass flow rate (g/s)';
num2cell(MdotPilot)];
    MdotJetCell = ['Jet mass flow rate (g/s)'; num2cell(MdotJet)];
    MixFracJetCell = ['Mixture fraction of jets';
num2cell(MixFracJet)];
```

```matlab
    PercJetMixCell = ['Percentage jet mixing'; num2cell(PercJetMix)];
    TauAutoTCell = ['Autoignition time based on T rise (ms)';
TauAuto_TVec];
    TauAutoHCell = ['Autoignition time based on H peak (ms)';
TauAuto_HVec];
    TauAutoHCOCell = ['Autoignition time based on HCO peak (ms)';
TauAuto_HCOVec];

    TauResCell = [strcat('PFR Residence time (ms)
Run#',num2str(Run(i))); num2cell(TauRes)];
    TCell = [strcat('Temperature (K) Run#', num2str(Run(i)));
num2cell(T)];
    HCell = [strcat('Mole fraction H Run#',num2str(Run(i)));
num2cell(XH)];
    HCOCell = [strcat('Mole fraction HCO Run#',num2str(Run(i)));
num2cell(XHCO)];
    %%
    DistanceCell = [strcat('Distance PFRC2
Run#',num2str(i),'_(mm)');num2cell(Distance)];
    DataCell = [cellstr(Headers)';num2cell(Data)];
    OutVec1 = [DistanceCell DataCell];
    %     FinName = sprintf(Name(1,:));
    xlswrite(Name(1,:), OutVec1, num2str(Run(i)));

    %% collecting Tau, T, XH, XHCO
    RunNumCell = num2cell(NaN(size(DistanceCell)));
    RunNumCell(1,1) = cellstr(strcat('Run#',num2str(Run(i))));
    OutVec2(1:length(DistanceCell), (Run(i)-1)*5+1:(Run(i)-1)*5+5) =
[RunNumCell TauResCell TCell HCell HCOCell];

end
xlswrite(Name(1,:), OutVec2, 'Profiles');
OutVec3 = [RunCell, NameCell,FuelPilotCell, FuelJet1Cell,
FuelJet2Cell,...
    FuelJet1PercCell, FuelJet2PercCell, PhiPilotCell, PhiJetCell,...
    PPilotCell, PGasCell, TPilotCell, TJetCell, TGasCell,
MdotPilotCell,...
    MdotJetCell, MixFracJetCell, PercJetMixCell, TauAutoTCell,...
    TauAutoHCell, TauAutoHCOCell];
xlswrite(Name(1,:), OutVec3, 'Tau');
```

APPENDIX F. ADDITIONAL VELOCITY AND FLAME

RESULTS
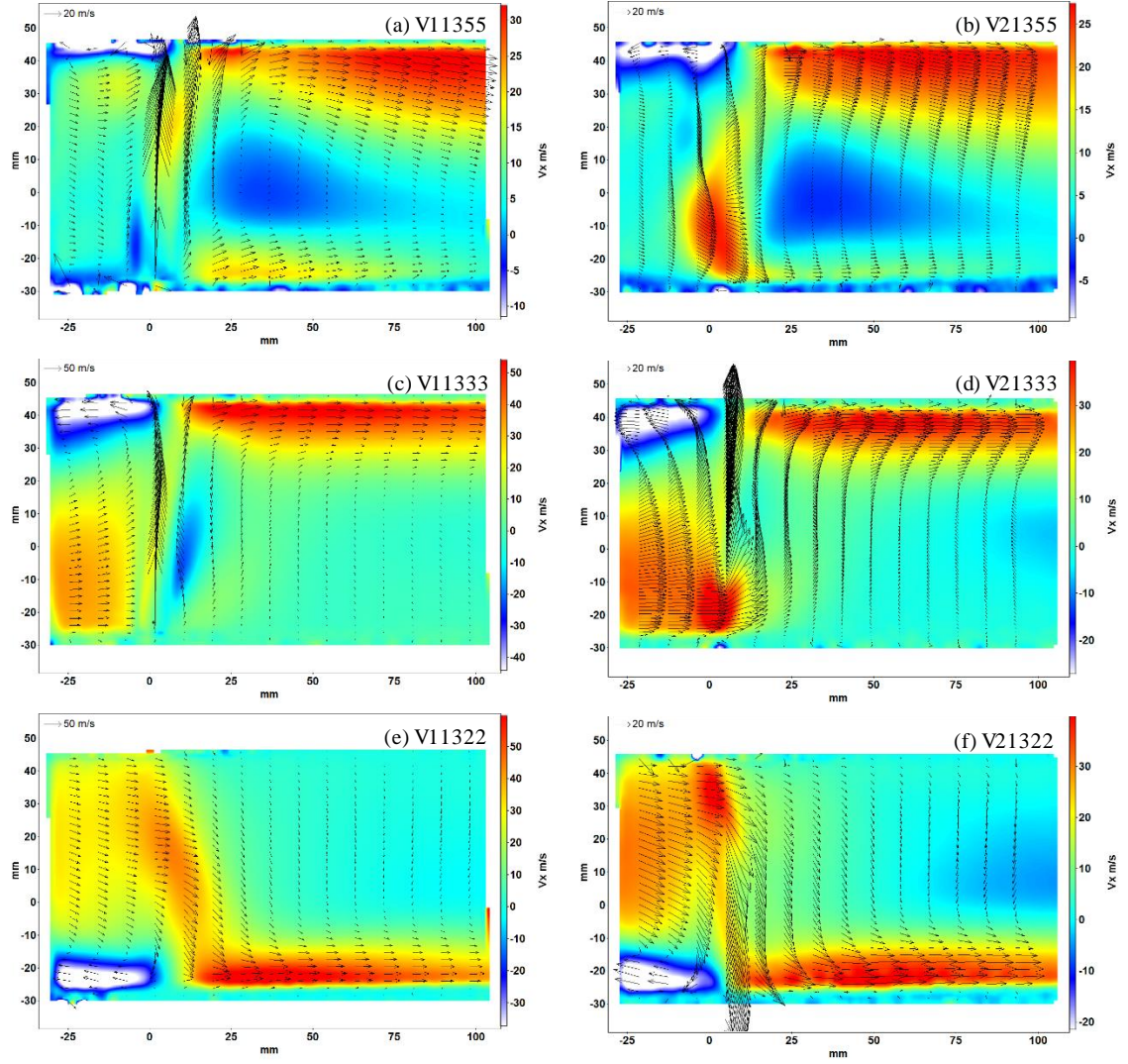
Figure F.1: Mean V_x field of CJICF (*Split* = 1.3) and velocity vectors at different axial locations for plane 1 (left) and plane 2 (right). (a, b) 5 staggered jets, $J = 252$). (c, d) 3 parallel jets, $J = 701$. (e, f) 2 parallel jets, $J = 1578$.
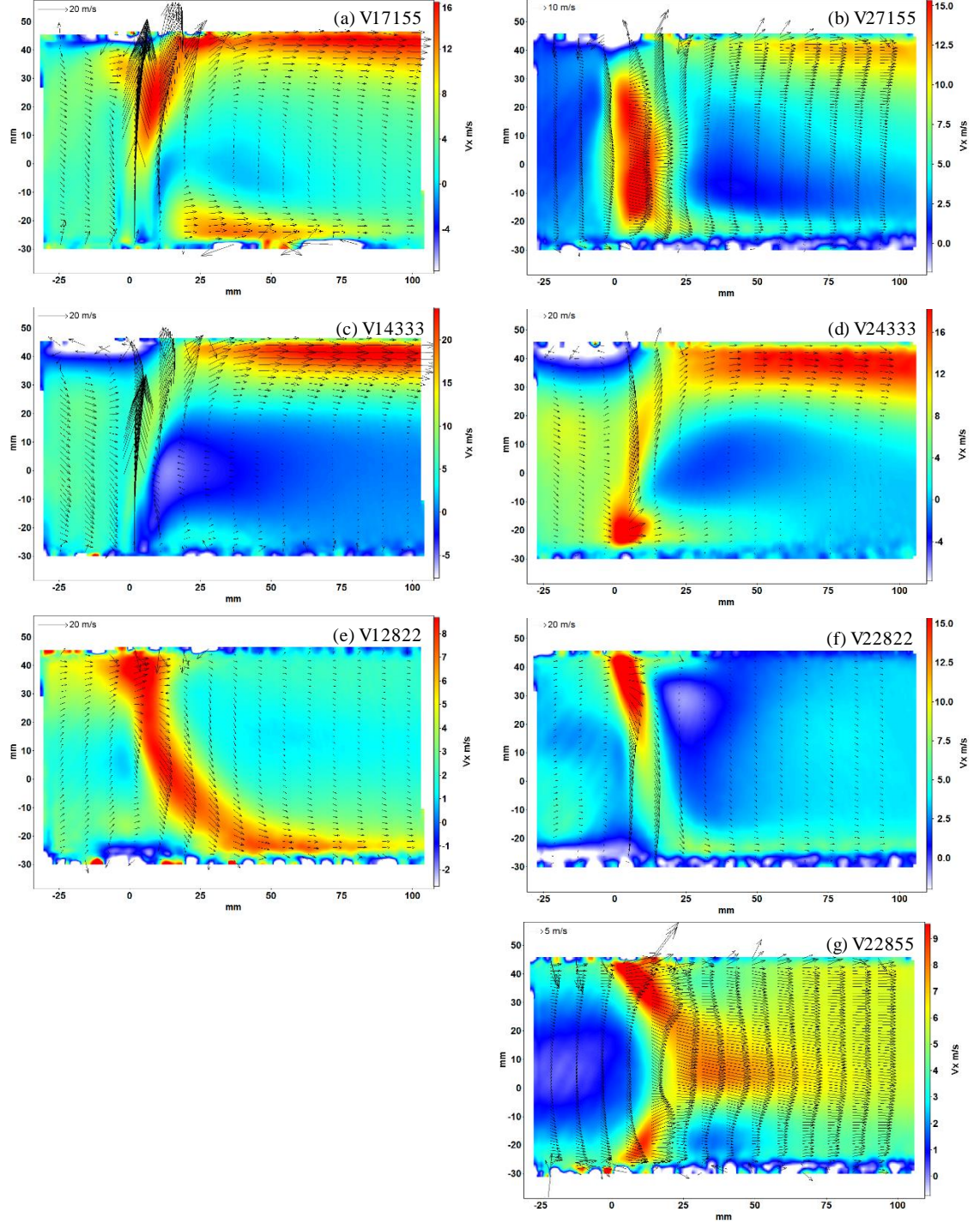
Figure F.2: Mean V_x field of CJICF (J = 75) and velocity vectors at different axial locations for plane 1 (left) and plane 2 (right). (a, b) 5 staggered jets, *Split* = 0.78. (c, d) 3 parallel jets, *Split* = 0.43. (e, f) 2 parallel jets, *Split* = 0.28.
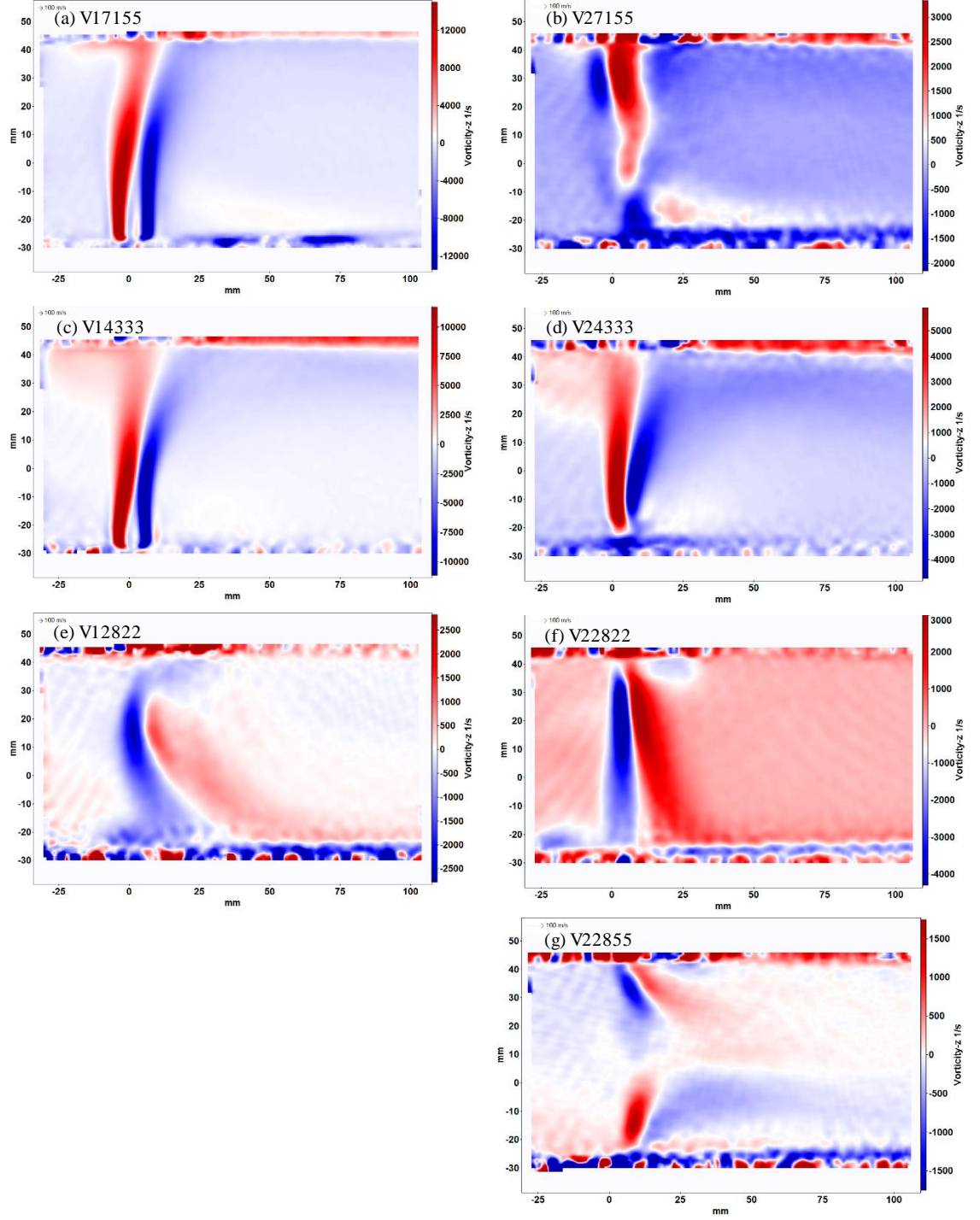
Figure F.3: Mean vorticity field of CJICF ($J = 75$) for plane 1 (left) and plane 2 (right). (a, b) 5 staggered jets, *Split* = 0.71. (c, d) 3 parallel jets, *Split* = 0.43. (e, f) 2 parallel jets, *Split* = 0.28.
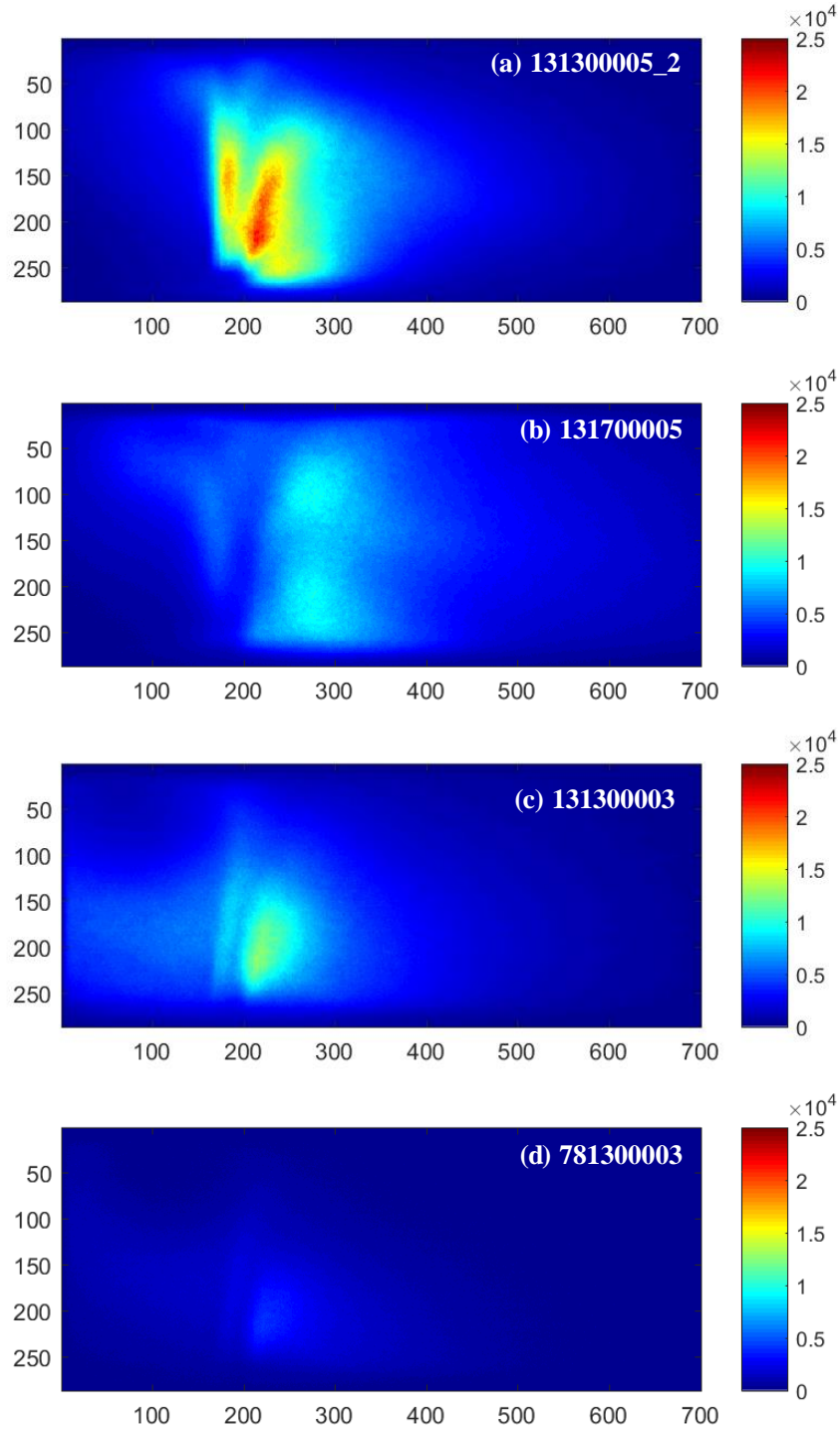
Figure F.4: Average chemiluminescence intensity images for RQL CJICF conditions with rich pilot and air jets. (a) Split = 1.3, ϕ_P = 1.3, J = 62, 5 staggered jets, (b) Split = 1.3, ϕ_P = 1.7, J = 75, 5 staggered jets (intensity scaled x2), (c) Split = 1.3, ϕ_P = 1.3, J = 173, 3 parallel jets, (d) Split = 0.78, ϕ_P = 1.3, J = 62, 3 parallel jets. Note same color map scaling for each result.
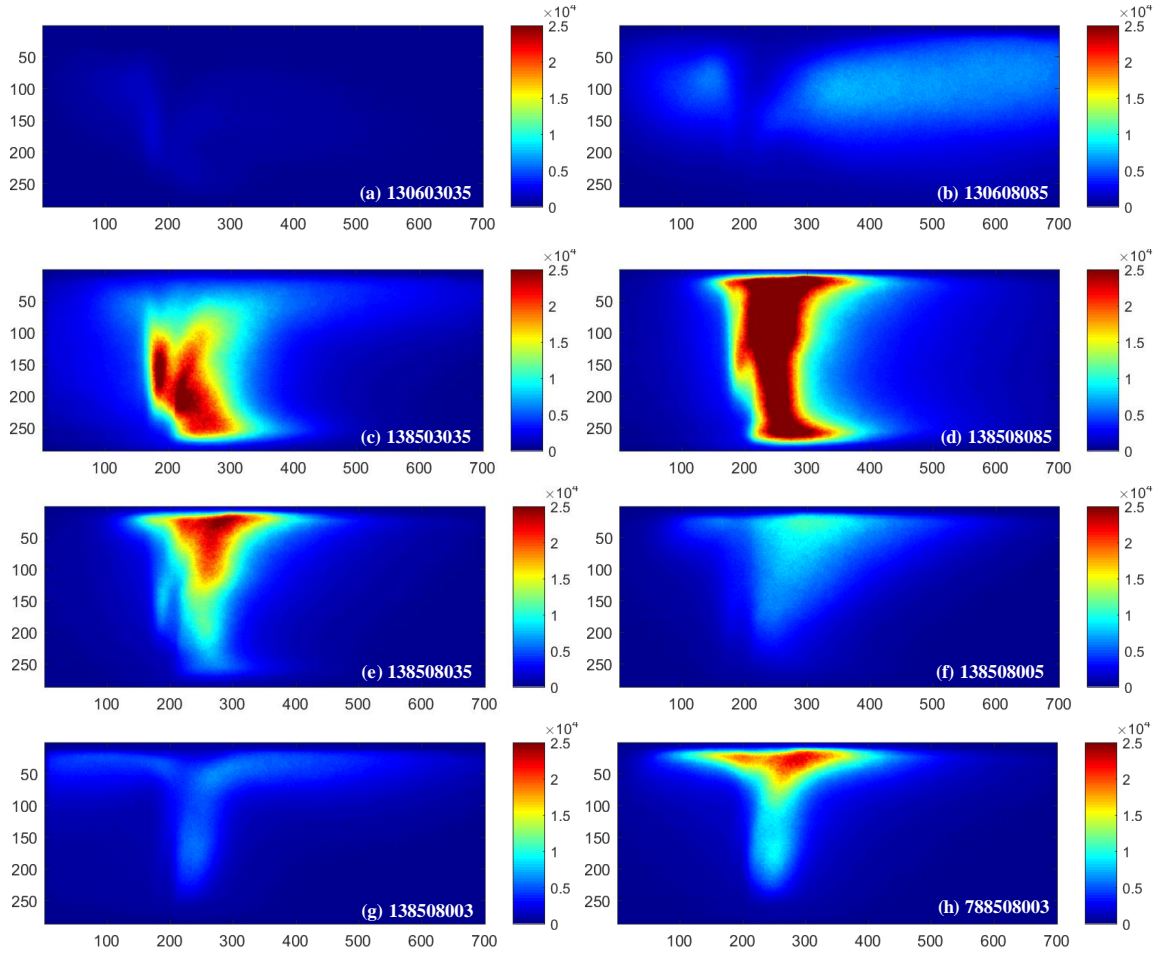
Figure F.5: **Average chemiluminescence intensity images for LQL CJICF with staggered 5 jets (a-f) and parallel 3 jets (g, h), split = 1.3 (a-g) and 0.78 (h), ϕ_p = 0.6 (a, b) and 0.85 (c-h). (a) ϕ_{bj} = ϕ_{tj} = 0.3 (b) ϕ_{bj} = ϕ_{tj} = 0.8, (c) ϕ_{bj} = ϕ_{tj} = 0.3, (d) ϕ_{bj} = ϕ_{tj} = 0.8, (e) ϕ_{bj} = 0.8, ϕ_{tj} = 0.3, (f) ϕ_{bj} = 0.8, ϕ_{tj} =0, (g, h) ϕ_{bj} = 0.8. Note the same color map scaling for each result. Note camera settings same for (a-c) and (d-h).**

REFERENCES

1. Chu, S. and A. Majumdar, *Opportunities and challenges for a sustainable energy future.* Nature, 2012. **488**: p. 294.

2. International Air Transport Association (IATA). *Fact Sheet Industry Statistics.* 2018; Available from: https://www.iata.org/pressroom/facts_figures/fact_sheets/Documents/fact-sheet-industry-facts.pdf.

3. Ommi, F. and M. Azimi, *Most effective combustion technologies for reducing Nox emissions in aero gas turbines.* The International Journal of Multiphysics, 2012. **6**(4): p. 417-424.

4. Schumann, U., *The impact of nitrogen oxides emissions from aircraft upon the atmosphere at flight altitudes—results from the aeronox project.* Atmospheric Environment, 1997. **31**(12): p. 1723-1733.

5. Köhler, I., R. Sausen, and R. Reinberger, *Contributions of aircraft emissions to the atmospheric NOx content.* Atmospheric Environment, 1997. **31**(12): p. 1801-1818.

6. EPA, U.S., *Control of Air Pollution from Aircraft and Aircraft Engines; Final Emission Standards and Test Procedures, EPA-420-R-12-011.* 2012.

7. Bowman, C.T., *Twenty-Fourth Symposium on CombustionControl of combustion-generated nitrogen oxide emissions: Technology driven by regulation.* Symposium (International) on Combustion, 1992. **24**(1): p. 859-878.

8. Lefebvre, A.H., *Gas turbine combustion.* 1998: CRC press.

9. Wilde, B., *Dynamics of variable density ratio reacting jets in unsteady, vitiated crossflows.* 2014.

10. Fowler, D., C. Flechard, U.T.E. Skiba, M. Coyle, and J.N. Cape, *The atmospheric budget of oxidized nitrogen and its role in ozone formation and deposition.* New Phytologist, 1998. **139**(1): p. 11-23.

11. Bandaru, R.V. and S.R. Turns, *Turbulent jet flames in a crossflow: effects of some jet, crossflow, and pilot-flame parameters on emissions.* Combustion and Flame, 2000. **121**(1–2): p. 137-151.

12. Hatch, M., W. Sowa, G. Samuelsen, and J. Holdeman, *Influence of Geometry and Flow Variations on NO Formation in the Quick Mixer of a Staged Combustor.* 1995.

13.   McGuirk, J., *The aerodynamic challenges of aeroengine gas-turbine combustion systems.* The Aeronautical Journal, 2014. **118**(1204): p. 557-599.

14.   McKinney, R.G., D. Sepulveda, W. Sowa, and A.K. Cheung. *The Pratt & Whitney TALON X low emissions combustor: revolutionary results with evolutionary technology.* in *45th AIAA Aerospace Sciences Meeting and Exhibit.* 2007.

15.   Margason, R.J. *Fifty years of jet in cross flow research.* in *In AGARD, Computational and Experimental Assessment of Jets in Cross Flow 41 p (SEE N94-28003 07-34).* 1993.

16.   Moin, P. and S.V. Apte, *Large-eddy simulation of realistic gas turbine combustors.* AIAA journal, 2006. **44**(4): p. 698-708.

17.   Boyce, M.P., *10 - Combustors*, in *Gas Turbine Engineering Handbook (Fourth Edition).* 2012, Butterworth-Heinemann: Oxford. p. 427-490.

18.   Liu, Y., X. Sun, V. Sethi, D. Nalianda, Y.-G. Li, and L. Wang, *Review of modern low emissions combustion technologies for aero gas turbine engines.* Progress in Aerospace Sciences, 2017. **94**: p. 12-45.

19.   Lefebvre, A.H. and D.R. Ballal, *Gas turbine combustion: alternative fuels and emissions*. 2010: CRC press.

20.   Koff, B.L., *Aircraft Gas Turbine Emissions Challenge.* 1993(78927): p. V03CT17A083.

21.   Lazik, W., T. Doerr, S. Bake, R. vd Bank, and L. Rackwitz. *Development of lean-burn low-NOx combustion technology at Rolls-Royce Deutschland.* in *ASME Turbo Expo 2008: Power for Land, Sea, and Air.* 2008. American Society of Mechanical Engineers.

22.   Mongia, H.C., *TAPS: A Fourth Generation Propulsion Combustor Technology for Low Emissions.* AIAA paper, 2003. **2657**: p. 2003.

23.   Washam, R. *Dry low NOX combustion system for utility gas turbine.* in *1983 Joint Power Generation Conference: GT Papers.* 1983. American Society of Mechanical Engineers.

24.   Samuelsen, G.S., J. Brouwer, M.A. Vardakas, and J.D. Holdeman, *Experimental and modeling investigation of the effect of air preheat on the formation of NOx in an RQL combustor.* Heat and Mass Transfer, 2013. **49**(2): p. 219-231.

25.   Peterson, C.O., W.A. Sowa, and G. Samuelsen, *Performance of a model rich burn-quick mix-lean burn combustor at elevated temperature and pressure.* 2002, NASA/CR-2002-211992.

26. Sturgess, G., R. McKinney, and S. Morford. *Modification of combustor stoichiometry distribution for reduced NOx emission from aircraft engines*. in *ASME 1992 International Gas Turbine and Aeroengine Congress and Exposition*. 1992. American Society of Mechanical Engineers.

27. Haselbach, F. and R. Parker. *Hot End technology for advanced, low emission large civil aircraft engines*. in *28th International Congress of the Aeronautical Sciences*. 2012.

28. Foust, M.J., D. Thomsen, R. Stickles, C. Cooper, and W. Dodds, *Development of the GE aviation low emissions TAPS combustor for next generation aircraft engines*. AIAA Paper, 2012. **936**: p. 2012.

29. Lazik, W., T. Doerr, S. Bake, R. vd Bank, and L. Rackwitz. *Development of lean-burn low-NOx combustion technology at Rolls-Royce Deutschland*. in *ASME Turbo Expo 2008: Power for Land, Sea, and Air*. 2008. American Society of Mechanical Engineers.

30. Davis, L.B. *Dry low NOx combustion systems for GE heavy-duty gas turbines*. in *ASME 1996 International Gas Turbine and Aeroengine Congress and Exhibition*. 1996. American Society of Mechanical Engineers.

31. Davis, L. and R. Washam. *Development of a dry low NOx combustor*. in *ASME 1989 International Gas Turbine and Aeroengine Congress and Exposition*. 1989. American Society of Mechanical Engineers.

32. Wagner, J.A., S.W. Grib, M.W. Renfro, and B.M. Cetegen, *Flowfield measurements and flame stabilization of a premixed reacting jet in vitiated crossflow*. Combustion and Flame, 2015. **162**(10): p. 3711-3727.

33. Marr, K.C., N.T. Clemens, and O.A. Ezekoye, *Mixing characteristics and emissions of strongly-forced non-premixed and partially-premixed jet flames in crossflow*. Combustion and Flame, 2012. **159**(2): p. 707-721.

34. Leong, M.Y., G.S. Samuelsen, and J.D. Holdeman, *Optimization of Jet Mixing into a Rich, Reacting Crossflow*. Journal of Propulsion and Power, 2000. **16**(5): p. 729-735.

35. Holdeman, J.D. and C.T. Chang, *Low Emissions RQL Flametube combustor component test results*. 2001.

36. Karagozian, A.R., *Transverse jets and their control*. Progress in Energy and Combustion Science, 2010. **36**(5): p. 531-553.

37. Ben-Yakar, A., M.G. Mungal, and R.K. Hanson, *Time evolution and mixing characteristics of hydrogen and ethylene transverse jets in supersonic crossflows*. Physics of Fluids, 2006. **18**(2): p. 026101.

38.   Gevorkyan, L., T. Shoji, D.R. Getsinger, O.I. Smith, and A.R. Karagozian, *Transverse jet mixing characteristics.* Journal of Fluid Mechanics, 2016. **790**: p. 237-274.

39.   Holdeman, J.D., D.S. Liscinsky, G.S. Samuelsen, V.L. Oechsle, and C.E. Smith. *Mixing of multiple jets with a confined subsonic crossflow in a cylindrical duct.* in *ASME 1996 International Gas Turbine and Aeroengine Congress and Exhibition.* 1996. American Society of Mechanical Engineers.

40.   Holdeman, J.D., D.S. Liscinsky, and D.B. Bain. *Mixing of multiple jets with a confined subsonic crossflow: Part II—Opposed rows of orifices in rectangular ducts.* in *ASME 1997 International Gas Turbine and Aeroengine Congress and Exhibition.* 1997. American Society of Mechanical Engineers.

41.   Holdemann, J.D. and C.T. Chang, *Mixing of Multiple Jets with a Confined Subsonic Crossflow: Part III--The Effects of Air Preheat and Number of Orifices on Flow and Emissions in an RQL Mixing Section.* 2008, NASA/TM—2008-215151.

42.   Fric, T. and A. Roshko, *Vortical structure in the wake of a transverse jet.* Journal of Fluid Mechanics, 1994. **279**: p. 1-47.

43.   Kamotani, Y. and I. Greber, *Experiments on a Turbulent Jet in a Cross Flow.* AIAA Journal, 1972. **10**(11): p. 1425-1429.

44.   Ruggeri, R.S., E.E. Callaghan, and D.T. Bowden, *Penetration of air jets issuing from circular, square, and elliptical orifices directed perpendicularly to an air stream.* 1950, NACA TN 2019.

45.   Coelho, S.L.V. and J.C.R. Hunt, *The dynamics of the near field of strong jets in crossflows.* Journal of Fluid Mechanics, 1989. **200**: p. 95-120.

46.   Smith, S.H. and M.G. Mungal, *Mixing, structure and scaling of the jet in crossflow.* Journal of Fluid Mechanics, 1998. **357**: p. 83-122.

47.   Su, L. and M. Mungal, *Simultaneous measurements of scalar and velocity field evolution in turbulent crossflowing jets.* Journal of Fluid mechanics, 2004. **513**(1): p. 1-45.

48.   Wagner, J.A., *Experimental Studies on Flow Field and Flame Stabilization of a Premixed Reacting Jet in Vitiated Crossflow.* 2016.

49.   Kelso, R.M., T. Lim, and A. Perry, *An experimental study of round jets in cross-flow.* Journal of fluid mechanics, 1996. **306**: p. 111-144.

50.   Hasselbrink, E.F. and M.G. Mungal, *Transverse jets and jet flames. Part 2. Velocity and OH field imaging.* Journal of Fluid Mechanics, 2001. **443**: p. 27-68.

51. Kolla, H., R.W. Grout, A. Gruber, and J.H. Chen, *Mechanisms of flame stabilization and blowout in a reacting turbulent hydrogen jet in cross-flow.* Combustion and Flame, 2012. **159**(8): p. 2755-2766.

52. Grout, R., A. Gruber, H. Kolla, P.-T. Bremer, J. Bennett, A. Gyulassy, and J. Chen, *A direct numerical simulation study of turbulence and flame structure in transverse jets analysed in jet-trajectory based coordinates.* Journal of Fluid Mechanics, 2012. **706**: p. 351-383.

53. Mortberg, M., W. Blasiak, and A.K. Gupta, *Experimental investigation of flow phenomena of a single fuel jet in cross-flow during highly preheated air combustion conditions.* Journal of engineering for gas turbines and power, 2007. **129**(2): p. 556-564.

54. Sullivan, R., B. Wilde, D.R. Noble, K. Periagaram, J.M. Seitzman, and T.C. Lieuwen, *Unsteady flame-wall interactions in a reacting jet injected into a vitiated cross-flow.* Proceedings of the Combustion Institute, 2013. **34**(2): p. 3203-3210.

55. Galeazzo, F.C.C., G. Donnert, P. Habisreuther, N. Zarzalis, R.J. Valdes, and W. Krebs, *Measurement and simulation of turbulent mixing in a jet in crossflow.* Journal of Engineering for Gas Turbines and Power, 2011. **133**(6): p. 061504.

56. Foley, C.W., J. Seitzman, and T. Lieuwen, *Analysis and Scalings of Blowoff Limits of 2D and Axisymmetric Bluff Body Stabilized Flames.* Turbo Expo, GT2012-70048, 2012.

57. Micka, D.J. and J.F. Driscoll, *Stratified jet flames in a heated (1390 K) air cross-flow with autoignition.* Combustion and Flame, 2012. **159**(3): p. 1205-1214.

58. Schmitt, D., M. Kolb, J. Weinzierl, C. Hirsch, and T. Sattelmayer. *Ignition and Flame Stabilization of a Premixed Jet in Hot Cross Flow*. in *ASME Turbo Expo 2013: Turbine Technical Conference and Exposition*. 2013. American Society of Mechanical Engineers.

59. Holdeman, J.D., *Mixing of multiple jets with a confined subsonic crossflow.* Progress in Energy and Combustion Science, 1993. **19**(1): p. 31-70.

60. Walker, R. and D. Kors, *Multiple jet study*. 1973, NASA CR 121217.

61. Reynolds, R. and C. White, *Transition mixing study*. 1986, NASA CR-175062.

62. Leong, M., G. Samuelsen, and J.D. Holdeman, *Mixing of jet air with a fuel-rich, reacting crossflow.* Journal of propulsion and power, 1999. **15**(5): p. 617-622.

63. Wang, S.J. and A.S. Mujumdar, *Flow and mixing characteristics of multiple and multi-set opposing jets.* Chemical Engineering and Processing: Process Intensification, 2007. **46**(8): p. 703-712.

64.   Holdeman, J., R. Srinivasan, E. Coleman, G. Meyers, and C. White, *Effects of multiple rows and noncircular orifices on dilution jet mixing.* Journal of Propulsion and Power, 1987. **3**(3): p. 219-226.

65.   Holdeman, J. and R. Srinivasan, *Modeling dilution of jet flowfields.* Journal of Propulsion and Power, 1986. **2**(1): p. 4-10.

66.   Holdeman, J., R. Srinivasant, and A. Berenfeld, *Experiments in dilution jet mixing.* AIAA journal, 1984. **22**(10): p. 1436-1443.

67.   Meisl, J., R. Koch, R. Kneer, and S. Wittig. *Study of NOx emission characteristics in pressurized staged combustor concepts*. in *Symposium (International) on Combustion*. 1994. Elsevier.

68.   Periagaram, K., D. Noble, J. Seitzman, T. Lieuwen, S. Martin, and E. Portillo. *Measurement of flame characteristics of a low swirl burner at high pressures and velocities*. in *49th AIAA Aerospace Sciences Meeting including the New Horizons Forum and Aerospace Exposition*. 2011.

69.   Wiberg, R. and N. Lior, *Heat transfer from a cylinder in axial turbulent flows.* International Journal of Heat and Mass Transfer, 2005. **48**(8): p. 1505-1517.

70.   Otsu, N., *A threshold selection method from gray-level histograms.* IEEE transactions on systems, man, and cybernetics, 1979. **9**(1): p. 62-66.

71.   *"Chemical-Kinetic Mechanisms for Combustion Applications", San Diego Mechanism web page, Mechanical and Aerospace Engineering (Combustion Research), University of California at San Diego (http://combustion.ucsd.edu). (Accessed: 2014 June 16)*

72.   Shen, H.-P.S., J. Steinberg, J. Vanderover, and M.A. Oehlschlaeger, *A shock tube study of the ignition of n-heptane, n-decane, n-dodecane, and n-tetradecane at elevated pressures.* Energy & Fuels, 2009. **23**(5): p. 2482-2489.

73.   Dooley, S., S.H. Won, M. Chaos, J. Heyne, Y. Ju, F.L. Dryer, K. Kumar, C.-J. Sung, H. Wang, and M.A. Oehlschlaeger, *A jet fuel surrogate formulated by real fuel properties.* Combustion and Flame, 2010. **157**(12): p. 2333-2339.

74.   Zhao, Z., J. Li, A. Kazakov, F.L. Dryer, and S.P. Zeppieri, *Burning velocities and a high-temperature skeletal kinetic model for n-decane.* Combust. Sci. and Tech., 2004. **177**(1): p. 89-106.

75.   Dryer, F.L.   [cited 2015 March 23]; Available from: http://www.princeton.edu/mae/people/faculty/dryer/homepage/kinetic_models/jet-fuel-surrogate/.

76.   *Chemical-Kinetic Mechanisms for Combustion Applications*. Available from: http://combustion.ucsd.edu.

77.   Gregory P. Smith, D.M.G., Michael Frenklach, Nigel W. Moriarty, Boris Eiteneer, Mikhail Goldenberg, C. Thomas Bowman, Ronald K. Hanson, Soonho Song, William C. Gardiner, Jr., Vitali V. Lissianski, and Zhiwei Qin. *GRI-Mech 3.0*. Available from: http://combustion.berkeley.edu/gri-mech/version30/text30.html.